NASA Reference Publication 1335

1994

Nimbus-7 Earth Radiation Budget Calibration History--Part II: The Earth Flux Channels

H. Lee Kyle
Goddard Space Flight Center
Greenbelt, Maryland

Richard R. Hucek, Philip E. Ardanuy, Lanning M. Penn, and Brenda J. Vallette
Research and Data Systems Corporation
Greenbelt, Maryland

John R. Hickey
The Eppley Laboratory, Inc.
Newport, Rhode Island

Robert H. Maschhoff
Gulton Industries
Albuquerque, New Mexico

Brian S. Groveman
Computer Sciences Corporation
Lanham, Maryland

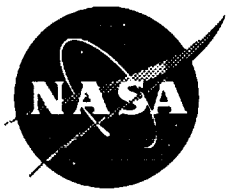

National Aeronautics and Space Administration

Scientific and Technical Information Branch

FOREWORD

Planning for what became the Nimbus Earth Radiation Budget (ERB) experiment started in 1968. The total program included both the Nimbus-6 and -7 ERB experiments. The Nimbus-6 was launched in June 1975 and the ERB sensors returned useful data through June 1978, while the Nimbus-7 was launched in October 1978 and the ERB returned useful data until turned off in 1993. Part II of the calibration history concerns the first 9 years of Nimbus-7 wide-field-of-view data (November 1978 through October 1987). Part I dealt with over 14 years of solar data (November 1978 through December 1993 but with gaps in 1992 and 1993). The experiment owes its existence and success to many dozens of dedicated engineers, computer analysts, scientists, and program managers who have worked on this experiment over its some 25 years of history. Here we will only mention a few who were important in the later years of the Nimbus-7 ERB measurement program. The present ERB Nimbus-7 Experiment Team (NET), the Nimbus-7 Operations crew (GE/Martin Marietta), the data processing crew and several NASA programs managers deserve special recognition for their support and contributions.

ERB NET (original members since 1976): John R. Hickey, Eppley Laboratory (with the program continuously since 1968); Fred B. House, Drexel University; Herbert Jacobowitz, NOAA/NESDIS; G. Louis Smith, NASA/Langley Research Center; Larry L. Stowe, NOAA/NESDIS; Thomas Vonder Haar, Colorado State University.

Elected members: Philip E. Ardanuy (1986), Research and Data Systems Corporation; Albert Arking (1983), NASA/GSFC; Garrett Campbell (1983); CIRA/Colorado State University; H. Lee Kyle (1983), NASA/GSFC; Robert Maschhoff (1983), Gulton Industries.

Nimbus Operations: Michael L. Forman, NASA/GSFC; (GE/Martin Marietta) John E. Sissala, Robert L. Berry and many others.

Data Processing: For quality control, Douglas V. Hoyt, Research and Data Systems Corporation; for production, Jesse Williams and Blanch Bowman (Hughes/STX); plus many others in both companies. Only Douglas Hoyt is still with the mentioned company.

NASA Program Managers: Albert J. Fleig, Edward J. Hurley, Daesoo Han, and Arnold G. Oakes (deceased) of the Goddard Space Flight Center; George Esenwein and Robert Schiffer of NASA Headquarters. Both Albert Fleig and Edward Hurley have now left the Government service.

Also greatly appreciated are the many Eppley Laboratory, Gulton Industries, General Electric and NOAA/NESDIS engineers and scientists who assisted in making the sensors, constructing the ERB instruments, integrating the ERB into the Nimbus spacecraft, and assisted in both the prelaunch and postlaunch ERB characterization and analysis program.

ACRONYMS AND ABBREVIATIONS

AN	ascending node
CAT	Calibration Adjustment Table
CZCS	Coastal Zone Color Scanner
DN	descending node
EMST	ERB MATRIX Summary Tape
ENSO	El Niño/Southern Oscillation
ERB	Earth Radiation Budget
ERBE	Earth radiation budget experiment
ERBS	Earth radiation budget satellite
FOV	field of view
LIMS	Limb Infrared Monitor of the Stratosphere
LW	longwave
MAT	Master Archive Tape
MFOV	medium-field-of-view
NASA	National Aeronautics and Space Administration
NESDIS	National Environmental Satellite, Data, and Information Service
NET	Nimbus-7 Experiment Team
NFOV	narrow-field-of-view
NIR	near infrared
NOAA	National Oceanic and Atmospheric Administration
OLR	outgoing longwave radiation
RMS	root mean square
SEFDT	Solar and Earth Flux Data Tape
SMMR	Scanning Multichannel Microwave Radiometer
SW	shortwave
SZA	solar zenith angle
TA	target area
TM	temperature monitor
TOA	top of the atmosphere
TSA	time and space averages
WFOV	wide-field-of-view

CONTENTS

Section			Page
FOREWORD			iii
ACRONYMS AND ABBREVIATIONS			v
1.	INTRODUCTION		1
	1.1	Background	1
	1.2	Chronology of ERB Experiment	2
2.	THE WFOV SENSORS AND PREFLIGHT CALIBRATION		4
3.	CHARACTERIZATION OF INFLIGHT WFOV SENSORS		7
	3.1	Principal Operational Problems	7
		3.1.1 Irradiance of Solar Target	9
		3.1.2 Long-Term Sensitivity Changes in All the Channels	9
		3.1.3 Reflectivity of the WFOV Baffle in Channel 12	15
		3.1.4 Temperature Variations and Thermal Gradients in Channels 13 and 14	15
		3.1.5 Longwave Dome Heating in Channels 13 and 14	17
	3.2	The Stability of Channel 12	18
	3.3	Calibration History	20
		3.3.1 Sensitivity Studies	22
	3.4	The Global CAT	24
4.	INFLIGHT WFOV CALIBRATION ADJUSTMENT		27
5.	LONG-TERM DEGRADATION MAINTENANCE		31
	5.1	Shortwave Sensitivities of the Total-Radiation Channels	32
	5.2	Longwave Sensitivities of the Total-Radiation Channels	34
	5.3	Sensitivity of the Shortwave Filtered Channel	36
	5.4	Sensitivity of the Near-Infrared Filtered Channel	39
	5.5	Asymmetric Degradation of the Filtered Channels	40
6.	REMOVAL OF SOLAR TARGET IRRADIANCE		42
	6.1	Elimination of Stray Light	44
	6.2	Interpolation Across Sunblip	45
7.	THERMAL ADJUSTMENTS OF CHANNELS 13 AND 14		45
	7.1	Satellite Night	47
	7.2	Satellite Sunrise and Sunset	47
		7.2.1 Solar Heating	48
		7.2.2 Thermal Cooling	48
		7.2.3 Convolution	49
	7.3	Satellite Day	50
	7.4	Validation Using Thermal Models	52
8.	LONGWAVE DOME HEATING CORRECTION IN CHANNELS 13 AND 14		58

9. CONCLUSIONS AND DISCUSSION 59
9.1 Calibration Conclusions 59
9.2 Discussion 61

10. REFERENCES 66

APPENDIX A—WFOV Sensitivity From Observations of the Sun A-1

APPENDIX B—Thermal Models B-1

APPENDIX C—WFOV Adjustment Equations C-1

1. INTRODUCTION

1.1 Background

The Nimbus-7 Earth Radiation Budget (ERB) experiment made measurements from November 16, 1978 until sometime in 1993. A 10 channel solar telescope recorded the total solar irradiance and wide band spectral irradiances at a satellite altitude of 950 km above the Earth's surface. Four fixed, wide-field-of-view (WFOV) nadir-pointing sensors recorded the emitted and reflected irradiance from the Earth, while a biaxial scanner recorded Earth-reflected and emitted radiances as a function of the nadir and azimuth angles. The scanner failed on June 22, 1980, but the solar and WFOV sensors continued to operate to the end of the experiment in 1993. An overview of the scientific results is given by Kyle et al. (1993a). A description of the instrument and an initial discussion of the calibration appears in Jacobowitz et al. (1984a), while an update on the scanner calibration and products is given by Kyle et al. (1990b). Part I of this calibration history reviewed the long-term calibration of the solar channels (Kyle et al., 1993b), while Part II (this paper) discusses the Earth-viewing WFOV channels (see Table 1). Over 14 years of WFOV measurements were recorded and archived. However, due to budget constraints, only 9 years (November 1978 to October 1987) of data have been properly calibrated and processed. Only the total solar irradiance measurements were calibrated for the entire period of over 14 years.

Table 1. Characteristics of ERB fixed wide-angle FOV channels

All channels have type N3 thermopile sensors. All channels have an unencumbered FOV of 121° and a maximum FOV of 133.3°. Channel 12 has an additional FOV selection of 89.4° unencumbered, 112.4° maximum. Output of these channels is a 3.8-s integral of the instantaneous readings.

Channel	Wavelength Limits (μm)	Filter
11*	<0.2 to >50	None
12*	<0.2 to >50	None
13	0.2 to 3.8	Two Suprasil W hemispheres
14	0.695 to 2.8	RG695 between two Suprasil W hemispheres

*Channels 11 and 12 are redundant channels. Channel 11 has black-painted baffles and is used for in flight calibration of channel 12; it is often covered. Channel 12 has polished aluminum baffles as did both channels 11 and 12 on Nimbus-6. The longwave radiation (4 to >50 μm) is given by channel 12 at night and by the difference (ch12-ch13) during daylight.

The calibration procedures for a long-term experiment evolve over time for two reasons. First, both the sensor and its environment change over the years, and secondly, the longer a sensor and its measurements are studied the better the operation of the sensor is understood. In the case of the ERB WFOV sensors, there were four sequential stages in their calibration history—one prelaunch and three postlaunch. Although calibrated with care before launch (Hickey and Karoli, 1974), the dynamic environment on the

satellite differed so markedly from the laboratory calibration conditions that major postlaunch calibration adjustments had to be made. As described by Kyle, et al. (1985), the postlaunch calibration studies went through three phases and culminated in the spring of 1985 with the adoption of the present global Calibration Adjustment Table (CAT) algorithm. Of the Earth-viewing channels, only the longwave narrow-field-of-view (NFOV) scanner channels had true on-board calibration capabilities. A blackbody mounted inside the scanner housing furnished a hot reference point while space looks were used to obtain a cold reference point. The postlaunch calibration of these channels appeared well behaved (Jacobowitz et al., 1984a). However, a filtered to nonfiltered radiance algorithm was required to account for the nonflat spectral response function of the longwave diamond filter. Thus when questions arose about the inflight calibration of the WFOV channels, it was decided to compare their results with those of the longwave NFOV sensors and to adjust the WFOV results to be consistent with those of the NFOV. From this comparison came the initial postlaunch WFOV calibration adjustments (Jacobowitz et al., 1984a and Kyle, et al., 1984). However, the scanner failed on June 22, 1980.

The long-term maintenance of the WFOV calibration, therefore, required the development of another calibration adjustment procedure. The development work included laboratory studies on sensors similar to the flight WFOV sensors in addition to detailed examination of the flight data. These studies resulted in an inflight characterization of the WFOV sensors (Maschhoff et al., 1984) and new calibration adjustment procedures (Kyle, et al., 1984) termed the Pacific CAT.

The Pacific CAT algorithm was used to process the WFOV data from June 1980-October 1983. Continued study of the inflight data plus an additional laboratory study led to a quantitatively improved algorithm termed the global CAT. The global CAT better describes how the calibration bias of the shortwave channels 13 and 14 varies from one part of the orbit to another. It also more accurately quantifies and corrects for the long-term degradation of all the WFOV channels. Both the Pacific and global CAT's are based on the long-term stability of the total (0.2 to 50 μm) channel 12. The shortwave channel 13 and 14 calibrations are adjusted by comparing their measurements to those of channel 12 while observing the central Pacific Ocean (Pacific CAT) or the entire globe (global CAT). At present, all 9 years of the available WFOV products have been processed or reprocessed using the preferred global CAT calibration (Kyle et al., 1993a). This paper describes the characterization of the WFOV sensors in their satellite environment and the global CAT calibration adjustments used for the long-term dataset. The calibration problems can generally be divided into two time categories, short-term and long-term, plus a general sensor characterization category. Thermal perturbations can be caused both by the instrument absorbing radiant energy from the Sun and the Earth and by the on-off cycle of the various instruments on the satellite. In addition, direct solar radiation strikes the WFOV detector twice per orbit, at satellite sunrise and sunset, and overwhelms the signals from the Earth. Such problems are termed "short-term" because even though they persist throughout the experiment, they vary continually and rapidly within a satellite orbit. Changes in the sensors and sensor optics that occur over weeks, months, or years are called "long-term" as are any changes that are permanent. The general category deals with noncyclic satellite operating conditions that were not properly anticipated in the preflight calibration procedures. The chief one of these was the cold ring of space about the warm Earth which occurs in the field of view of channel 12. Section 2 describes the sensors and the preflight calibration while Section 3 discusses the various in orbit problems. The following Sections 4-7 describe the adopted solutions to these problems.

1.2 Chronology of ERB Experiment

The ERB experiment was but one of eight experiments on the Nimbus-7 satellite, and the ERB itself consisted of three subpackages: the solar channels, the WFOV channels, and the scanner. The ERB WFOV thermal environment and operating schedule were strongly influenced by the operating schedules

of the other experiments and of the ERB scanner. The ERB WFOV and solar sensors used the same on/off power command and so had to have identical operating schedules. For reference, the major events in the ERB operating schedule are listed in Table 2. Because of the limited spacecraft power available, the ERB and several other instruments operated in a power-sharing mode for the first several years. As various instruments became nonfunctional and were turned off, the ERB was able to operate continuously for long periods.

Table 2. Major ERB Events

Date	Event
October 24, 1978	Launch of Nimbus-7 satellite
November 16, 1978	Initial turn on. ERB in 3-day-on/1-day-off power sharing schedule with other Nimbus-7 experiments. From time to time, the schedule varied somewhat.
December 10, 1978 through April 13, 1979	ERB scanning activity is curtailed because it interfered with the short-lived LIMS experiment which studied trace gases in the stratosphere. 12/10 to 12/30/78 — Scanning on 2-day-on/2-day-off schedule; WFOV and solar on 3-day-on/1-day-off schedule 12/30 to 3/9/79 — Further curtailment; no scanning near the north pole, nor in the northern hemisphere at night 3/10 to 3/31/79 — Global scanning, 2-day-on/2-day-off schedule 4/1/ to 4/13 — ERB on 1-day-on/1-day-off mode but no scanning
April 14, 1979	ERB and scanner returns to 3-day-on/1-day-off schedule, but with occasional variations
June 22, 1980	Scanner chopper wheel stops. This terminates useful scanner measurements. Efforts to restart the chopper continued through July 18. The noise in channel 10c decreased noticeably after July 18.
September 11, 1983	ERB put on full-time on schedule
April 18, 1984	ERB returns to 3-day-on/1-day-off schedule
October 28, 1984	ERB back on full-time on schedule
April 9 to June 23, 1986	No Earth flux measurements, but ERB was on for 20 minutes on most orbits for solar measurements. This allowed the CZCS experiment additional power for its end-of-life program
April 22 to August 20, 1987	Earth flux measurements taken only on alternate days to conserve power. On the off days, ERB was on for 30 minutes per orbit to make solar measurements; however, these measurements were noisy
August 24, 1987	ERB back on full-time on schedule
November 1, 1987	Final calibration of WFOV data not done after this date due to budget constraints.

Table 2. Major ERB Events	
Date	Event
September 24-28, 1989	ERB sensor data blanked out by a temporary electronics problem possibly caused by a cosmic ray. Normal data transmission recommenced on the afternoon of September 28.
January 4-11, 1992	The ERB solar telescope refused to move from γ=-14° to -15° in order to track the Sun, but it would move in the other direction. Several tests were made and finally on January 11, the telescope moved to γ=-15°. The telescope has moved normally since that time.
January 15-23, 1992	Some of the ERB sensor data became meaningless, then it all became saturated. Data alternated between meaningless signals and saturation. This was probably caused by energetic particles damaging the electronic circuits. Normal operation resumed on January 23.
June 17-September 2, 1992	The Sun was not clearly visible during this period. The solar telescope can move only over the range, $\gamma = \pm 20°$. The precession of the orbit over the years combined with the seasonal progression of the Sun relative to the satellite moved the Sun out of the unrestricted field of view of channel 10c during this period.
January 25, 1993	The continued precession of the orbit again moved the Sun out of the unrestricted field of view of channel 10c.
February 9, 1993	ERB electronics turned off.

The calibration and final processing of the WFOV measurements stopped because of budget constraints after October 31, 1987, but the measurements were still taken and archived. The total solar irradiance measurements taken by the ERB solar sensor (channel 10c) were considered more important and were calibrated and released. The WFOV and solar channels shared both the same power switch and the same initial data processing software. This accounts for the continued archiving of the WFOV measurements. The post-1987 WFOV measurements received a brief, routine quality review and appeared to be of good quality.

2. THE WFOV SENSORS AND PREFLIGHT CALIBRATION

The four WFOV sensors employ identical flatplate thermopile detectors that are baffled to limit their unencumbered FOV to 121°. This size is slightly greater than the solid angle of the Earth, subtended at spacecraft altitude (955 km), and allows for satellite attitude fluctuations and misalignment of the channel detectors with respect to nadir. It also permits a narrow ring of space radiation to be included in the sensor observations. This radiation is insignificant over much of an orbit cycle, but near satellite sunrise and sunset, the solar disc moves across the space ring and adds a strong, direct component of extraterrestrial radiation to the measurements (cf. Section 3.1.1). Less intense, indirect solar radiation also strikes the receiver surface via reflection from the baffle walls. This occurs for the approximate subsatellite solar zenith angle range from 90° (detector perpendicular to direction of solar irradiance) to 120° (satellite enters the Earth's shadow). Figure 1 is a drawing of channel 13 and will be used in discussing all four channels (11 through 14). Channels 11 and 12 are called total channels since they have no limiting spectral filters. They were identical on Nimbus-6, with channel 11 used as a reference and kept shuttered for protection most of the time. On Nimbus-7, channel 11 is also a reference but its baffle walls are painted black to reduce internal reflections. Channels 13 and 14 each have two quartz

dome filters to block longwave radiation, the inner filter intended to shield the thermopile from outer dome heating. Channel 14 has an additional 695-red glass dome, between the two quartz domes, which blocks most visible light. The spectral band limits of the channels and their filter types are given in Table 1.

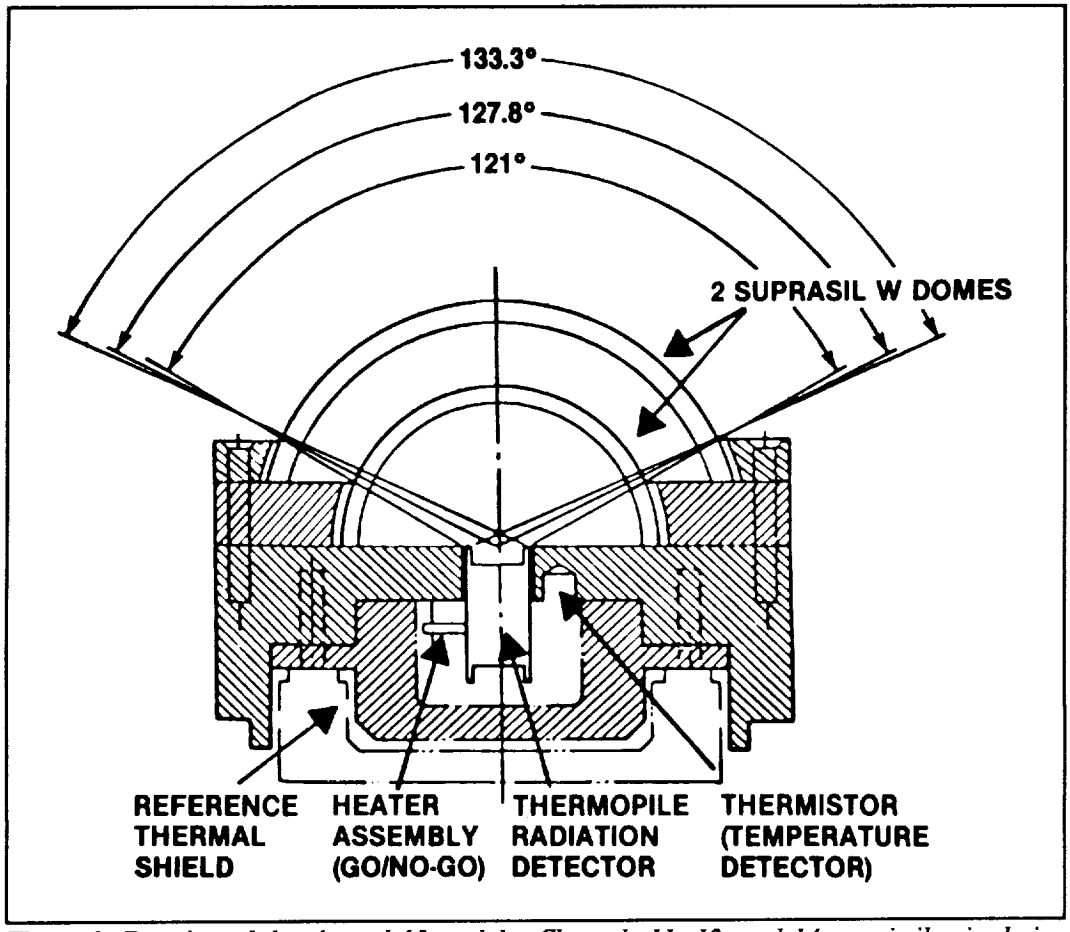

Figure 1. Drawing of the channel 13 module. Channels 11, 12, and 14 are similar in design except that channels 11 and 12 have no covering domes, while 14 has a red glass insert between the two domes.

The prelaunch calibration equations are approximations of the two-way flux of radiant energy across the receiver surface and, for the total channels, energy balance is expressed in the form (Jacobowitz et al., 1984; Kyle et al., 1984)

$$\Delta W = H_T \cdot F_T - \epsilon_D \cdot F_D \cdot \sigma \cdot (T_D + kV)^4 \qquad (1)$$

where ΔW is the net irradiance (W/m^2) at the detector, $H_T \cdot F_T$ is incoming target irradiance at satellite altitude, and $\epsilon_D F_D \sigma (T_D + kV)^4$ is outgoing thermal radiation from the detector. The target configuration factor, F_T, is normally set to unity so that H_T alone gives the satellite altitude irradiance. However, it may also be convenient to consider the satellite altitude radiation as a spherical wave propagating away from the source. If F_T contains the geometrical dependence of the irradiance amplitude on distance (inverse square law), then H_T is the magnitude of the irradiance at its source (i.e., the top of the

atmosphere). Additional parameters are ϵ_D and T_D, the emissivity and temperature (°K) of the detector, respectively; σ, the Stefan-Boltzmann constant; V, the thermopile output digitized in counts (c); k, the thermopile temperature correction factor (°K/c); and F_D, the detector configuration factor. The configuration factor represents the receiver's effective FOV of space which, because of reflection from the baffle walls, is somewhat greater than its geometrical FOV. Thus, F_D accounts not only for the direct loss of receiver thermal radiation to space, but also indirect losses via radiative exchange between the baffle and the receiver.

The net irradiance is also given as a function of instrument parameters by

$$\Delta W = \frac{V - [V_0 + b(T_m - 25°C)]}{S_0 + a(T_m - 25°C)} \tag{2}$$

where V_0 is zero offset voltage in counts at 25°C, b is the offset voltage temperature coefficient (c/°C), T_m is module temperature (°C), S_0 is thermopile sensitivity at 25°C (c/Wm^{-2}), and a is the sensitivity temperature coefficient (c/Wm^{-2}/°C). The sensitivity $S = S_0 + a(T_m - 25)$ of (2) is the apparent thermopile sensitivity since it includes the effects of the receiver absorptivity, a_r, which reduces the flow of radiation through the receiver.

For the filtered channels, the calibration equations are similar to (1), but they suppose that near thermal equilibrium exists within the domed environment of the sensors. Infrared radiation incident upon the receiver is thus balanced by thermal emission from the receiver, and only the term for target SW radiation is present on the right-hand side. The expression for ΔW for the filter channels is given by

$$\Delta W = \frac{V - V_0}{S_0 \cdot (1.0 + 0.01 \cdot A \cdot (T_B - 25))} \tag{3}$$

where T_B is the thermopile base temperature (°C), and A is the sensitivity temperature correction factor (°C^{-1}). Notice that although (3) has a form similar to (2), its offset voltage, V_0, is not parameterized as a function of temperature as is done for the total channels. Although not anticipated, thermal gradients in the detector environment actually caused greater measurement perturbations in channels 13 and 14 than in channels 11 and 12, where V_0 is prescribed as a function of T_m.

Table 3 contains the calibration coefficients used in Eqs.(1), (2), and (3) for the production of both the Nimbus-6 and -7 MAT WFOV products. The data from the Nimbus-6 ERB experiment (Smith et al., 1977) has never been recalibrated although some empirical adjustments have been made (Bess et al., 1981, 1987). The calibration adjustments for the WFOV Nimbus-7 ERB measurements are described in the following sections.

Table 3. Nimbus-6 and -7 WFOV Calibration Coefficients (Postlaunch Values).								
	Channel 11		Channel 12W		Channel 13		Channel 14	
Constant	ERB 6	ERB 7	ERB 6	ERB 7	ERB 6	ERB 7	ERB 6	ERB 7
E_s								
E_D	0.977	0.977	0.977	0.977				
k	0.0031	0.0031	0.0031	0.0031				
F_s								
F_D	0.8628	0.80461	0.8628	0.8628				
S	1.598	1.49166	1.585	1.607	2.004	1.939	3.989	4.179
V_O	-24.76	-12.13	-27.56	-23.10	-41.0	-43.0	-44.0	-44.0
a	0.00242	0.00115	0.00177	0.00109				
b	-0.3377	-0.462	-0.4129	-0.638				
A					0.04	0.04	0.03	0.03
F_T	1.00	1.00	1.00	1.00	1.00	1.00	1.00	1.00

3. CHARACTERIZATION OF INFLIGHT WFOV SENSORS

Postlaunch studies have revealed numerous differences between the prelaunch-calibration environment and the satellite's orbital environment (Kyle et al., 1984; Maschhoff et al., 1984), and have identified two main uncertainties in the evaluation of the definitive calibration of the ERB WFOV channels. First, degradation of the optical elements in space has resulted in large transmissivity changes in the filtered shortwave channels. Smaller drifts in sensitivity have also occurred in the unfiltered channels. Second, the filtered shortwave radiation sensors, although designed in the laboratory to be insensitive to thermal gradients, have responded to the various thermal forcings present in the experiment's operating environment. The variable thermal state has arisen chiefly due to the presence of both the 104-minute orbital diurnal cycle and changes in the operating schedules of the various electronic systems, motors, and heaters.

3.1 Principal Operational Problems

The interior of the ERB instrument assembly is always warmer than its extremities (cf. Figure 22a) where the WFOV sensors are mounted to the satellite within an aluminum block. Figure 2 is a photograph of channel 13 showing its cylindrical thermopile casing and square aluminum body. The thermal conductivity of the aluminum body, although high, is finite and one expects a fraction of the instrument temperature gradient to exist from the front (scene side) to the back (heat sink side) of the sensor thermopiles. This, of course, would generate a response in the detectors which in channel 13, for example, would be 20 W/m^2 for a 10-millidegree (°C) thermopile temperature gradient. Verification of the existence of such temperature gradients in the flight data was difficult due to the lack of suitable temperature monitors on the instrument. Those available in and around the Earth flux module have a basic resolution of 0.1 °C and the analysis of averaged data obtained over hundreds of orbits was required to demonstrated that, indeed, such thermopile temperature gradients were possible (Maschhoff et al., 1984).

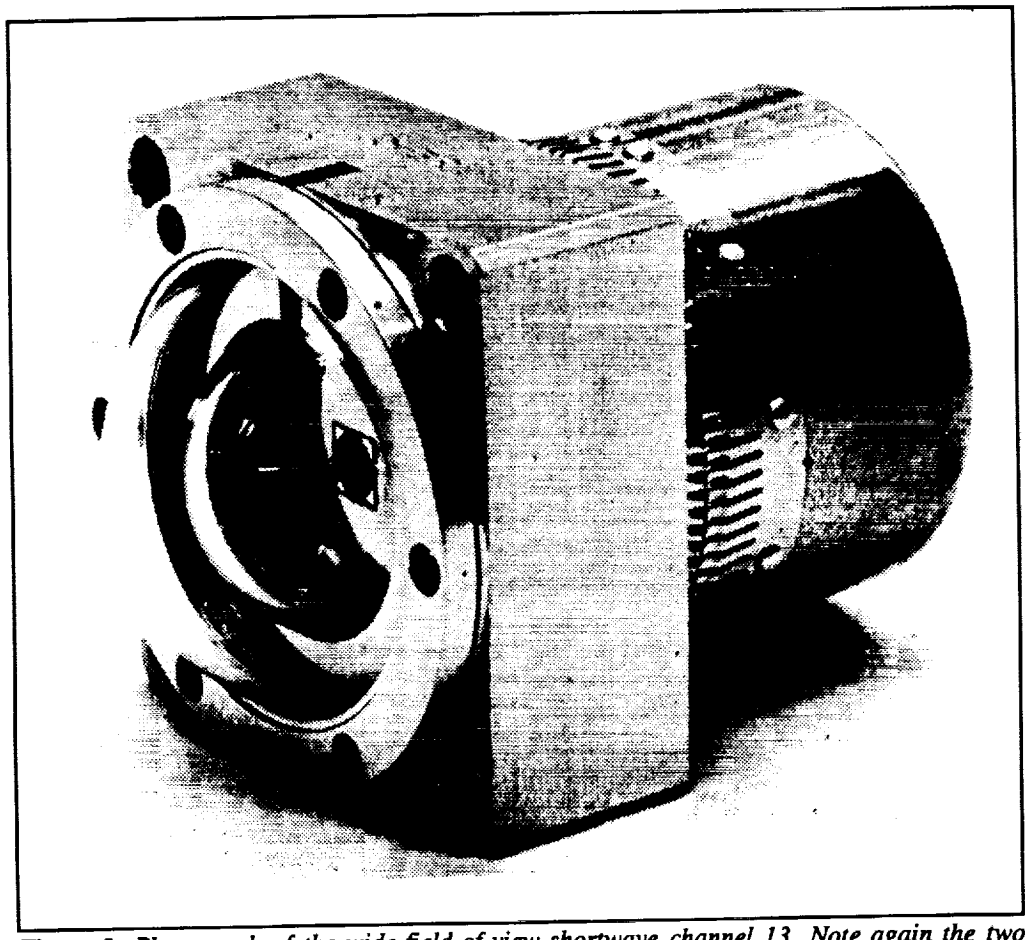

Figure 2. Photograph of the wide-field-of-view shortwave channel 13. Note again the two Suprasil-W filter domes mounted over the detector (black circle).

External solar and terrestrial radiative heating of the ERB instrument varies with orbital position and time of year while fluctuations in internal spacecraft heating occur with the turning on and off of the various instruments on the Nimbus observatory. Such short-term periodic variations are also observed in the measurements of the filtered channels (at night, for example, when the shortwave channels should read zero) and thus they are assumed to be governed by the effects of changing solar, terrestrial, and internal instrument heating. Similar perturbations are absent or hardly discernible in the data record of the total channel 12, and much reduced in channel 11. Thus, their effects in the filtered channels are considered to be related to the domes on these sensors and the fact that the terms of the calibration equations are incomplete. In particular, nonequilibrium infrared energy exchange between the receiver and the inner cavity dome is neglected in the prelaunch calibration equations while the effects of thermal gradients on the offset voltage are not considered. Both of these features of the prelaunch calibration equations proved inappropriate in the changing thermal environment on the satellite.

A loss of dome transmissivity and related changes in sensitivity also degraded the long-term accuracy of the filtered channel measurements. In the total channel 12, the infrared reflectivity of the WFOV baffles is observed to be greater in space than anticipated from the initial laboratory calibration studies, and this lead to an uncertainty in the values of the detector configuration factor and the channel sensitivity. In a related issue, direct and baffle-reflected solar radiation in the satellite observations resulted in some loss of data coverage at high and midlatitudes. Five principal operational problems exist, each closely related to one of the terms, or missing terms, in the prelaunch calibration equations. These are listed below

along with the associated calibration parameter. Because on-board calibration sources were not provided, diagnosis and correction of calibration problems have been accomplished mainly through careful scrutiny of the inflight data. A discussion of the radiometric record associated with each of the five major operational problems is given in the subsections to follow. ERB Master Archive Tape (MAT) data are used. These are satellite altitude irradiances processed using only the original prelaunch calibration equations; that is, subsequent calibration corrections are not yet applied.

1. Irradiance of solar target (not included in prelaunch calibration)
2. Long-term sensitivity changes in all the channels (S_0)
3. Reflectivity of the WFOV baffle in channel 12 (S_0 and F_D).
4. Temperature variations and thermal gradients in channels 13 and 14 (V_0).
5. Dome heating in channels 13 and 14 (not included in prelaunch calibration).

3.1.1 Irradiance of Solar Target

Figure 3 is a typical plot of an orbit of data, shown for channels 12-14 as a function of time (t) in seconds of day. Twice an orbit, the Sun enters the space ring of the sensors and is viewed directly, producing the "sunblip" spikes at satellite sunrise ($t \approx 15348$) and sunset ($t \approx 19420$). Because of the Sun-synchronous, near-polar satellite orbit with noon/midnight equator crossings, the sunblips always occur on the descending node (DN), the nighttime side of the orbit. If the FOV-limiting baffles worked perfectly reflecting all incoming energy back to space, the sunblips would run from solar zenith angles (SZAs) of 113° to 120° (cf. Figure 1). The cutoffs at 120° occur as the satellite enters (sunset) or leaves (sunrise) the Earth's shadow with the Sun hidden, but within the detector's unencumbered FOV. These events are readily distinguished in the figure, for channels 13 and 14, by the sharp increases in irradiance that takes place from the near-constant "zero" nighttime reference level.

On the daylight side of the sunblip peak, irradiance changes also occur rapidly, this time due to the movement of the solar disk across the baffle wall into (satellite sunset) or out of (satellite sunrise) the unencumbered FOV. However, a more gradual irradiance increase can also be seen near the base of the sunblip spike. This is not due to increasing terrestrial irradiance because it occurs in all seasons and for a sequence of WFOV footprints each enclosing a greater fraction of darkness than the one before. Rather, it is the sensor response to out-of-field solar radiation scattered back at the receiver by the baffle walls. Out-of-field scattering is possible in the range of sensor normal incident angles from 60° (SZA = 120°) to 90° (SZA = 90), the former marking satellite entry into or out of the Earth's shadow. Laboratory measurements, shown in Figure 4 for channels 11-14, confirm that baffle scattering leads to a positive signal in channels 12-14 at incident angles greater than 70° (SZA = 110°). The channel 11 response is approximately zero because the black baffles of this channel effectively absorbed all of the radiation incident upon them. The anomalous negative response in channel 12 at incident angles greater than 82° (SZA = 98°) is explained by Maschhoff et al. (1984) as due to a channel bias that has not been removed from the data. In the postlaunch and Pacific CAT procedures, ERB WFOV products were not calculated for satellite sunrise ($99° < SZA < 123°$) and sunset ($102° < SZA < 123°$), and data from 93° SZA to 99°/102° (sunrise/sunset) were used with no correction for scattered sunlight. In the global CAT, some adjustments plus an interpolation algorithm (see Section 6.2) are used to estimate emitted and reflected flux densities from 90° to 121°.

3.1.2 Long-Term Sensitivity Changes in All the Channels

Some degradation in the sensitivity of all the WFOV channels occurs in the space environment, most strongly in the shortwave channels 13 and 14 but also noticeable in the total channel 12. Figure 5 illustrates three time series of shortwave sensitivity estimates for each of channels 11-14 in panels a-d,

respectively. Each point on the curves corresponds to an unobstructed observation of the Sun taken by tilting the satellite toward (pitch-up) or away from (pitch-down) the direction of the spacecraft velocity vector (see Appendix A). For these measurements, the Sun is the calibration source, variable by perhaps up to 0.3 percent for a few of the individual observations but constant in the yearly mean to ± 0.075 percent (Hoyt et al., 1992; Kyle et al., 1993b). Sensitivity is computed by inversion of the measurement equation separately for satellite pitch-ups and pitch-downs, and also by averaging the results of the pitch-up and pitch-down sensitivities. The mean sensitivity curves for channels 11 and 12 are depicted by best-fitting trend lines to avoid obscuring the pitch-up and pitch-down data. Breaks in the curves indicate sampling periods of more than twenty four days which is the nominal schedule for execution of the satellite pitch maneuvers. The relatively high frequency signal (24 days) in these data is not believed to replicate sensitivity changes in the sensors. Instead it is effectively noise originating from uncertainties in the method including spacecraft attitude errors, solar variability, and estimation of terrestrial background signal.

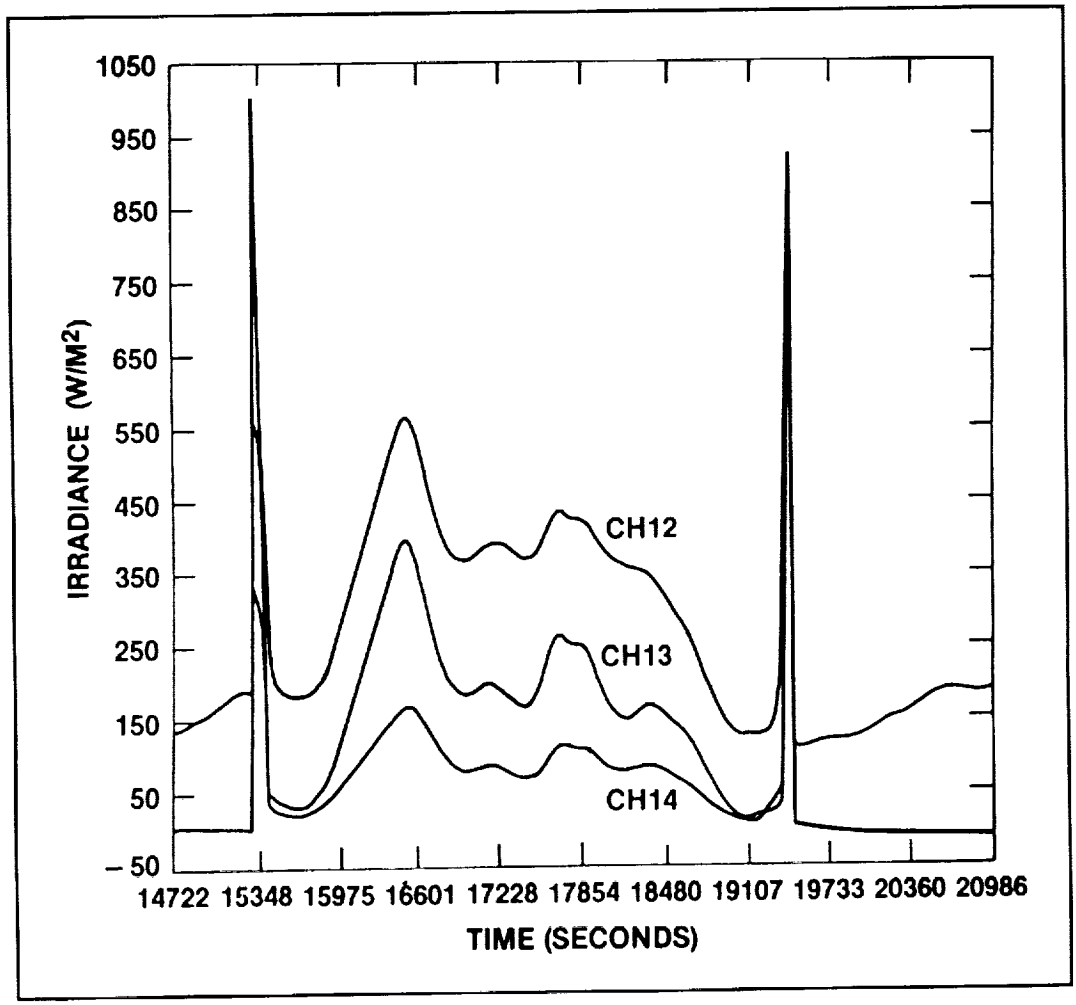

Figure 3. Channel 12, 13, and 14 irradiances (in watts per square meter) are shown during a typical orbit. The channels view the Sun directly close to the poles, producing the strong sunblip signals. When in the Earth's shadow, the signals from channels 13 and 14 should ideally be zero.

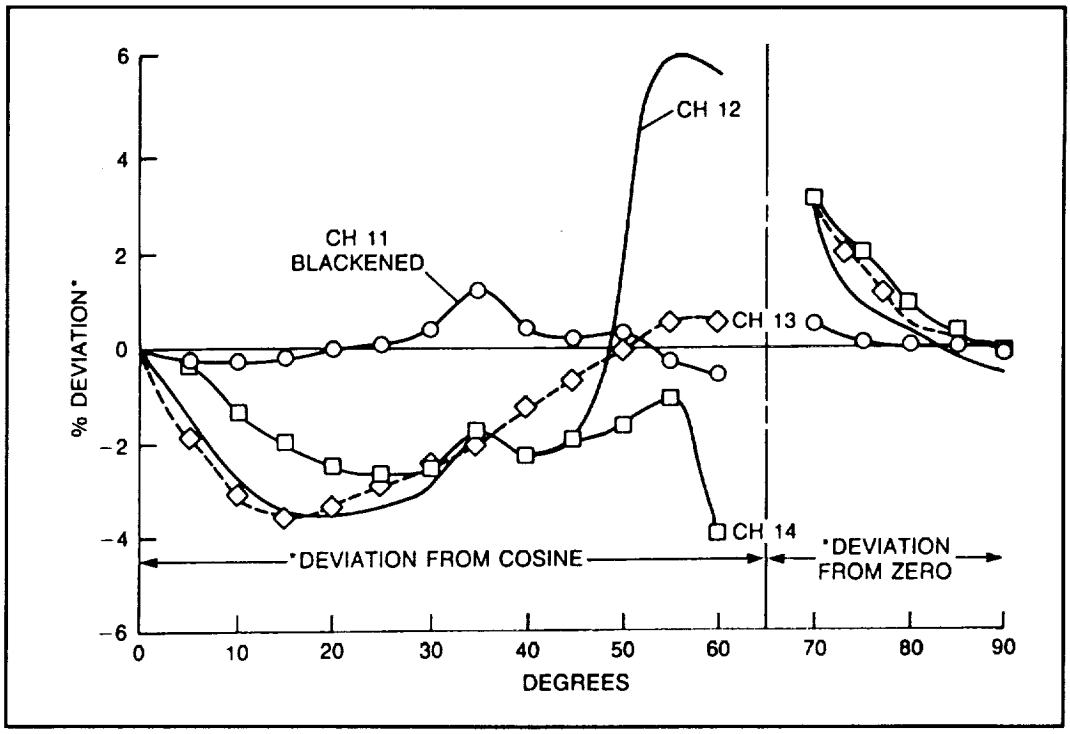

Figure 4. Laboratory measured responses as a function of the angle of incidence measured from the normal for the four WFOV sensors, channel 11-14. For angles less than 66.7°, direct rays can strike at least a portion of the detector chip and the curves show the percent difference from a cosine response. For angles greater than 66.7°, multiple bounces off the baffles cause the out-of-field response indicated in the graph as a percentage of normal incidence. (Figure was taken from Maschhoff et al., 1984.)

The sensitivities of channel 11 show little evidence of any secular trend through almost 10 years of pitch data, beginning in November of 1978 and ending in July of 1988. The slope of the mean curve indicates a +0.026 percent sensitivity change per year, but this is uncertain to ±0.032 percent per year (based on random departures from the trend line) and so should not be taken as significant. This channel was shuttered during the first 6 years of the experiment (except during pitch maneuvers) and, undoubtedly, this aided in protecting the receiver and baffles from deterioration. The operational total channel 12 has been open continuously throughout most of the mission, but it too has degraded only slightly (panel b) compared to channels 13 and 14. The trend line of mean sensitivities for channel 12 has a slope of -0.31 percent change per year. This degradation is most probably due to (1) a loss of baffle reflectivity, and (2) deterioration of the 3M black velvet paint pigment used to coat the receiver surfaces of all the channels (Soule, 1983). In comparison, solar "constant" measurements during this same period indicate a decrease in the solar constant of -0.15 percent between 1979 and 1984 with year-to-year changes of from 0.05 percent to 0.001 percent. After 1986 the solar "constant" begins to increase again (Hoyt et al., 1992).

Degradation in the shortwave channels 13 and 14 is due chiefly to an asymmetric loss of transmissivity in the Suprasil W filter domes covering these channels, the part facing the direction of spacecraft motion losing transparency faster than the opposite dome half. As with the ERB solar channels (Predmore et al., 1982), the decrease in transmissivity may have resulted from a number of causes including film formed through the condensation of organic vapors originating from outgassing of the satellite (Campbell et al., 1980), polymerization of organic films on the filter and optical surfaces after interaction with ultraviolet

solar radiation (Hall et al., 1980), and the reactions of organic vapors with fluxes of ultraviolet solar radiation, protons, and electrons (Mearns, 1969; Gillette et al., 1971; Kruger et al., 1980). Predmore et al. (1982) point out that opposing darkening and cleansing reactions go on, but the cleansing reactions are only important during the excited Sun years of the 11-year sunspot cycle. During solar maximum years, the increased solar ultraviolet causes an increase in the density of the atmosphere at the altitude of the Nimbus-7 satellite. The amount of atomic oxygen present increases by about two orders of magnitude. This highly reactive gas tends to clean the forward-facing portions of the domes. Exposure to solar ultraviolet and perhaps to the rare atmospheric gases appears required to produce noticeable darkening. Little darkening occurs on covered or sheltered windows. Both the darkening and the cleansing occur most strongly on exposed, forward-facing windows.

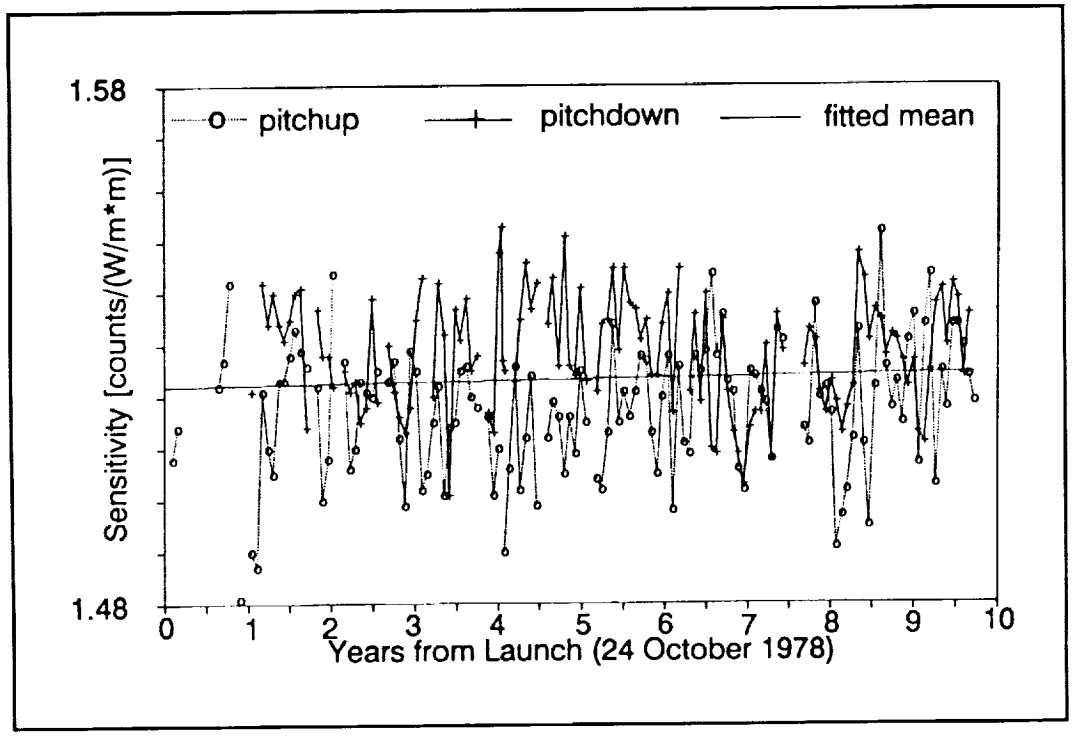

Figure 5a. Measured shortwave sensitivities of channel 11 for the period November 1978 to May 1988. The Sun was used as a calibration source after launch. The measurements were taken about once every 24 days by pitching the satellite up (sunrise) or down (sunset) to give the sensor a clear view of the Sun. The mean linear trend line is also shown.

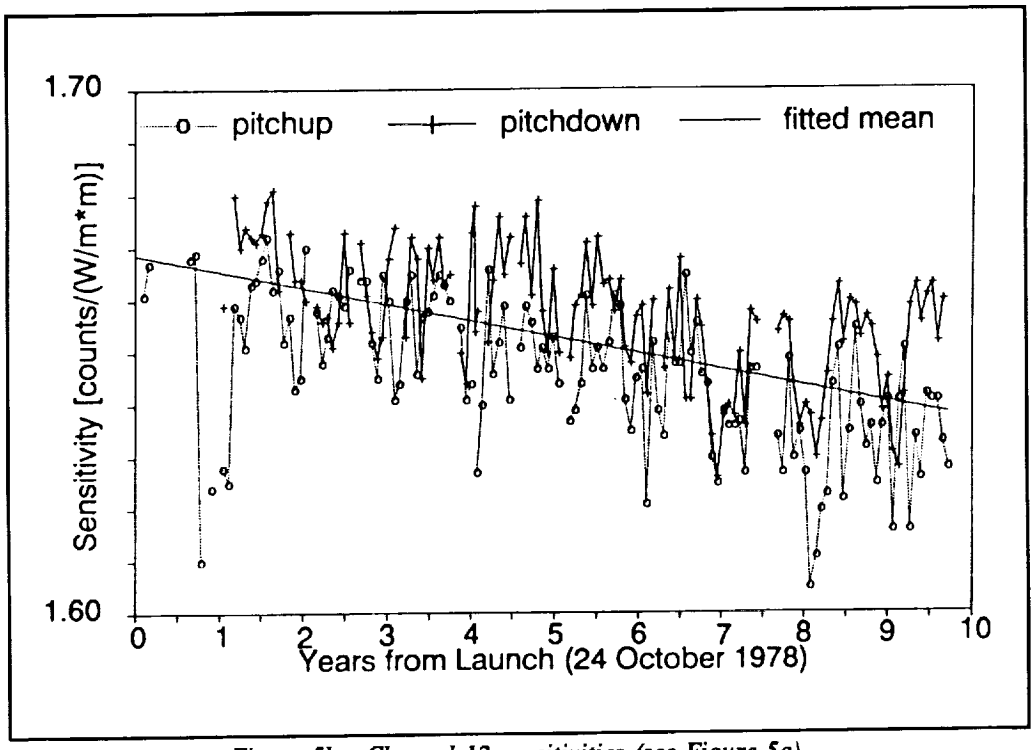

Figure 5b. Channel 12 sensitivities (see Figure 5a).

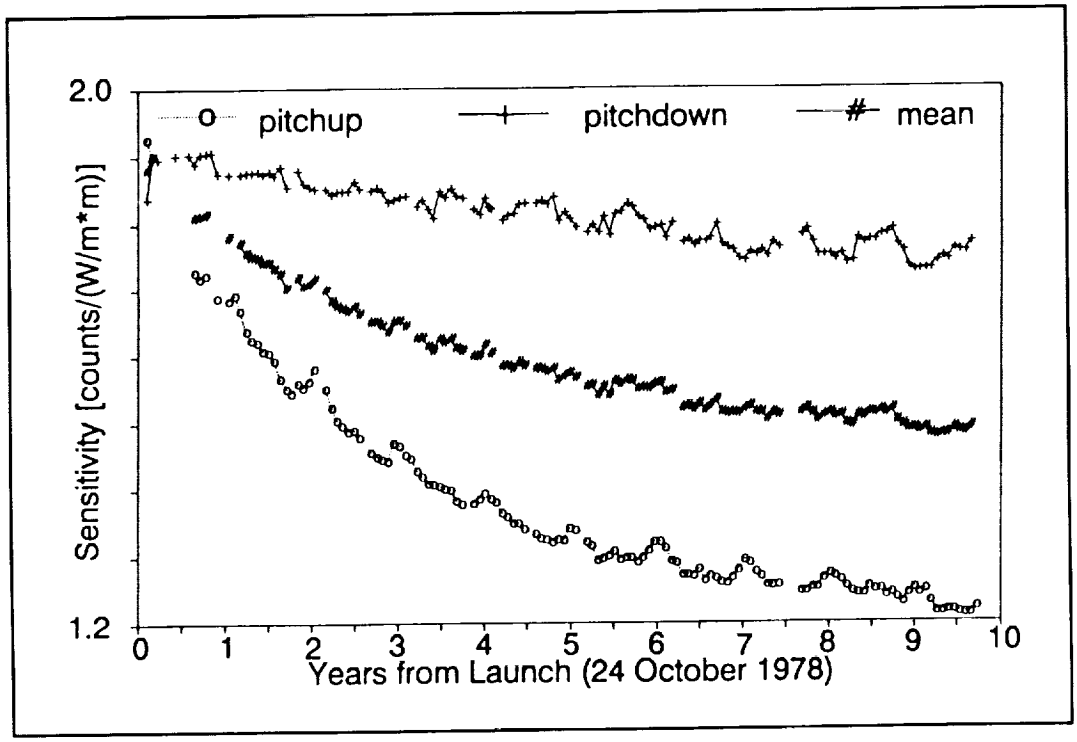

Figure 5c. Channel 13 sensitivities (see Figure 5a). The central curve represents the mean of the sunrise and sunset measurements. Only a fraction of the fogged dome is scanned during the calibration measurements hence the mean shown here, is not the true sensitivity for Earth flux measurements.

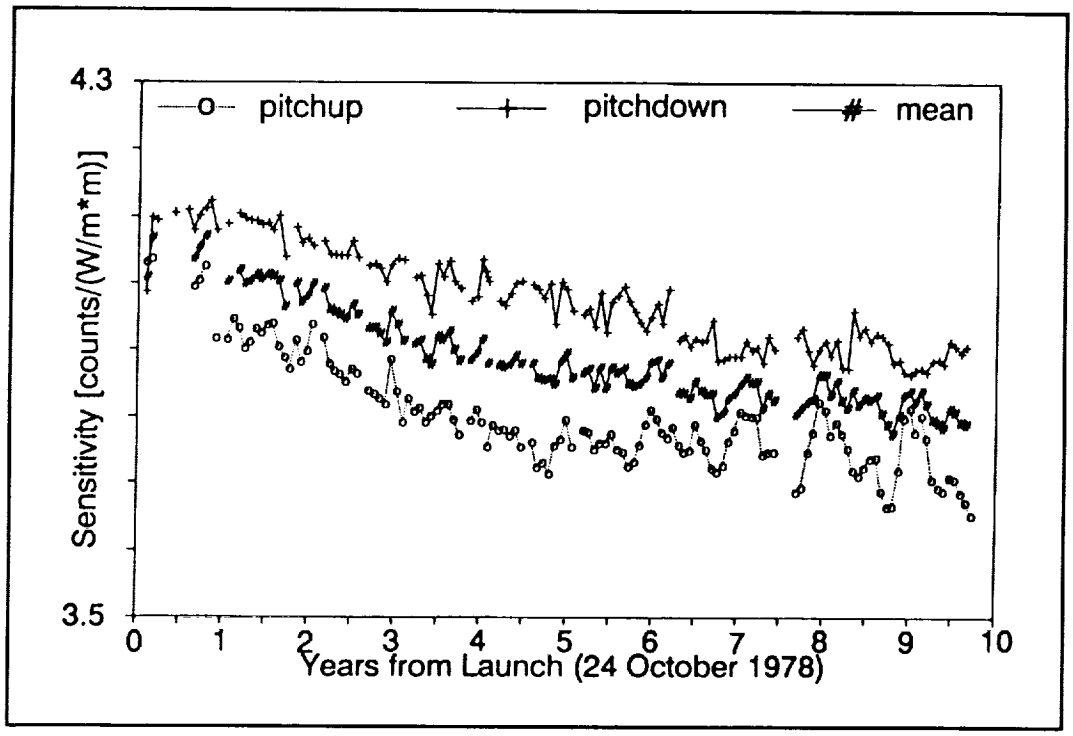

Figure 5d. Channel 14 sensitivities (see Figure 5c).

Sensitivity curves for channel 13 are shown in panel c for the same set of pitch events as displayed for the total channels in panels a and b. During pitch-up at satellite sunrise, solar observations are taken through the forward half of the filter dome while for pitch-downs, the Sun is viewed through rearward half of the dome. It should be noted, however, that while the detector views the solar disc only briefly during pitch events, all sides of the outer filter dome are irradiated by diffuse and specular shortwave radiation reflected by the Earth throughout two-thirds of every orbit. Furthermore, the forward hemisphere is subjected to 10 minutes of direct solar radiation every orbit, from spacecraft sunrise to the Southern Hemisphere terminator crossing where the ERB experiment housing then blocks direct solar illumination. Similar direct solar radiation is, to some extent, prevented from impinging upon the rear of the filter dome (at satellite sunset) by the presence of the neighboring channel 14 (cf. Figure B3 in Appendix B) through whose filter domes the radiation must pass. In addition to two longwave filters, channel 14 also contains a red-glass dome which passes near-infrared wavelengths but arrests the shorter visible and ultraviolet spectral components of the incoming solar beam at satellite sunset. As a result, the front portion of the filter dome apparently degraded more rapidly than the back as is indicated by the diverging sensitivities for the pitch-up and pitch-down time series. This asymmetry was also studied by comparison with the shortwave scanner data (Ardanuy and Rea, 1984). Only near launch do the two curves converge to suggest a more uniform sensitivity over the entire hemisphere. The average curve, based on the sunrise and sunset measurements, will apply at some point on the filter dome. However, this value is unlikely to be representative of the average sensitivity loss over the dome. An asymmetry correction based on the scanner comparison is applied to channel 13 (see Section 5.5; Kyle et al., 1984). There is evidence from the solar channels (Jacobowitz et al., 1984a) and from other experiments (Hickey et al., 1992) that the transmissivity loss is greater in the ultraviolet than in the near infrared. However, no correction has been determined or made for this wavelength-dependent problem.

Panel d presents the same three sensitivity estimates for the near-infrared filtered channel 14, and as in the preceding analysis of channel 13, both increasing sensor degradation with time and variations in

sensitivity over the filter dome are noted. Once again, the forward-facing region of the filter domes degrades more rapidly than the rearward-facing side, though not to the same degree as for the shortwave channel 13. The slower degradation rates of channel 14 may be linked to decreased transmissivity loss in the near infrared compared to the ultraviolet, as noted above. This asymmetric degradation is of a sufficiently small magnitude to obviate the need for any explicit correction, except for a time-varying mean sensitivity adjustment. Indeed, the degradation asymmetries appear to decrease after the end of the fifth data year, when the forward-facing portion of the dome apparently ceases to degrade during the next 2.5 years (through year 7.5). The transmissivity of the rear or back side of the filter, however, decreases at the more or less constant rate of about 0.7 percent throughout this period. Beyond year 7.5, the time series of pitch-up data become more variable making trend determination less certain.

3.1.3 Reflectivity of the WFOV Baffle in Channel 12

Careful examination of the time series data of Figure 5b shows that channel 12 shortwave sensitivities are about 1.67 (c/Wm^{-2}) on or about the time of sensor turn on in November of 1978. This value is nearly 4 percent greater than the prelaunch estimate of 1.607 (c/Wm^{-2}) and indicates that the reflectivity was underestimated during laboratory calibration measurements. The detector configuration factor (F_D) was overestimated by the same factor because the product, $S_0 \cdot F_D$, was measured with greater certainty and kept constant throughout the calibration history. Thus, even though their product was a known constant, deficiencies in the prelaunch laboratory procedures led to values of S_0 and F_D that are too low by and too high by factors of 0.962 and 1.040, respectively (see Section 3.3.1). Although these ratios pertain specifically to shortwave radiation, they should also apply to longwave radiation because the baffle reflectivity is assumed to be independent of wavelength.

3.1.4 Temperature Variations and Thermal Gradients in Channels 13 and 14

Channel 13 and, to a lesser extent, channel 14 are sensitive to nearby temperature gradients and, in operation, these gradients vary continually with position in orbit, the turning on and off of various experiments, and season. Thermally-induced bias shifts are illustrated in Figures 6 through 8 where ERB MAT data are plotted. Descending node daily average irradiances for channels 12, 13, and 14 are shown in Figures 6a through 6c, respectively. Daily data for 2-month intervals (September and October) are averaged over the latitude zone from 0 to 30°S and shown separately for the odd numbered years from 1979 to 1983. Channel 12 shows no obvious day-to-day pattern associated with the on-off instrument cycle. This is examined in more detail in Section 3.2. The local observing time is near midnight and, thus, both channels 13 and 14 should ideally read zero. For the years of 1979-1982, the ERB was on a 3-day-on/1-day-off observing cycle, and for this period, a strong pattern in the shortwave channel 13 bias exists. On the first day of a three-day on sequence, a near-zero but slightly negative bias is obtained. Successive days yield increasingly negative readings with values from -4 to -6 W/m^2 common by day three. This pattern was interrupted on September 11, 1983 when the ERB was turned on full-time until the following spring. Now, although the bias drifts slowly between -5 and -6 W/m^2, it is nearly constant over the relatively short 4-day periods of the previous 3-day-on/1-day-off instrument duty cycle. A 3-day pattern in the bias cycle of channel 14 also exist during the first 4 years of data as seen in Figure 6c. Day-to-day bias changes are smaller here than in channel 13 and the effects of the Scanning Multichannel Microwave Radiometer (SMMR) instrument heating are also conspicuous. When the SMMR is on, normally every other day, channel 14 biases decrease. This is the reason for the reduced day-2 biases relative to day 3. The effect of the ERB duty cycle is to decrease the bias by about 0.5 Wm^{-2} between days 1 and 3. The fact that the nighttime channel 14 signals are positive seems to indicate that the inner dome and perhaps the red glass filter are warmer than the sensor chip. A slight unidentified bias may also be present. Channel 13 also reads positive at night right after turn on but soon drifts to a negative nighttime signal (see Figure 19).

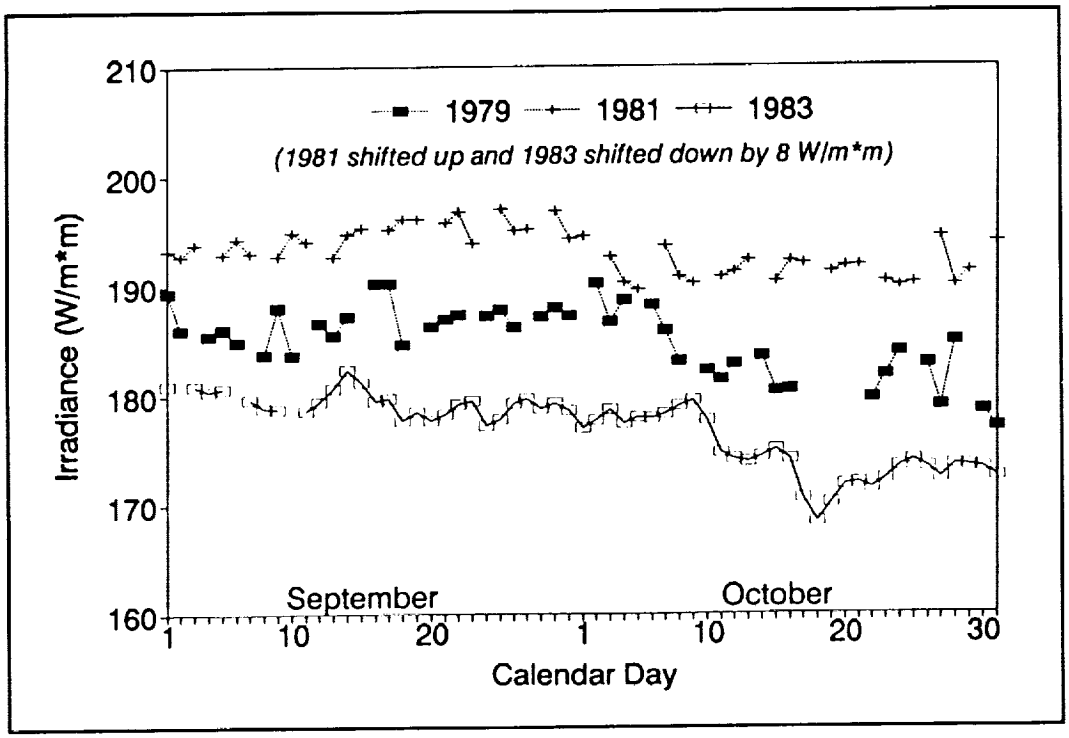

Figure 6a. Variable thermally induced biases can easily be detected in channels 13 and 14 but not in channel 12. To illustrate this, daily nighttime (descending node) data for September and October are averaged over the latitude zone from 0° to 30°S for the odd years from 1979 to 1983. Channel 12 data are shown in Figure a. The day-to-day shifts occur due both to weather variations and because somewhat different regions of the Earth are viewed on consecutive days.

Although heat sources associated with the ERB instrument appear to produce the dominant perturbations in the channel outputs, other Nimbus-7 experiments also contribute. After the ERB was turned on full-time in September 1983, a day-to-day modulation becomes visible in the channel 13 nighttime bias reading. As shown in Figure 7, the bias varied by about 0.6 W/m^2 in November and December 1983. A similar nighttime bias modulation of about 0.4 W/m^2 occurs in channel 14 (Figure 6c). When the SMMR is on, the channel 13 bias becomes more negative reflecting an increased ERB instrument temperature. About mid-November 1983 the SMMR was turned on full-time for an 11-day period. This produced a dramatic 2 W/m^2 drop in the channel 13 offset and a breakup of the coherent day-to-day offset modulation noted for the typical 1-day-on/1-day-off SMMR duty cycle. The small seasonal drift in the bias offset apparent in September and October (Figure 6b) produces larger magnitude biases in November and December. This is because the period of night from satellite sunset to satellite transition of the 0 to 30°S geographic latitude zone is greater in November and December. Thus, increased instrument cooling and greater temperature gradients are possible near solstice than near the equinox at these latitudes.

Ascending node daily average global MAT data are plotted in Figure 8 for three February's, 1979 through 1981. Channel 13 ERB averages show the same 3-day signal pattern that appears in the midnight biases. The large drop in the transmissivity of the channel 13 Suprasil-W dome during the first year of operations is responsible for part of the difference in the 1979 and 1980 averages. Bias differences of about 6 W/m^{-2}, associated with developing peculiarities in the ERB scanner during the winter of 1980, account for the rest (Kyle et al., 1984). Subsequently, on June 22, 1980, the chopper wheel on the scanner failed and the NFOV telescopes were parked in the nadir position beginning July 20, 1980. With the scanner off, channel 13 biases are smaller in February of 1981 than for the previous two February's.

in the figure by the opposing effect of continued dome degradation so global irradiances in 1981 have nearly the same values as in 1980. In channel 14, the day-to-day variations in the observed signal tend to obscure the small 3-day bias modulation.

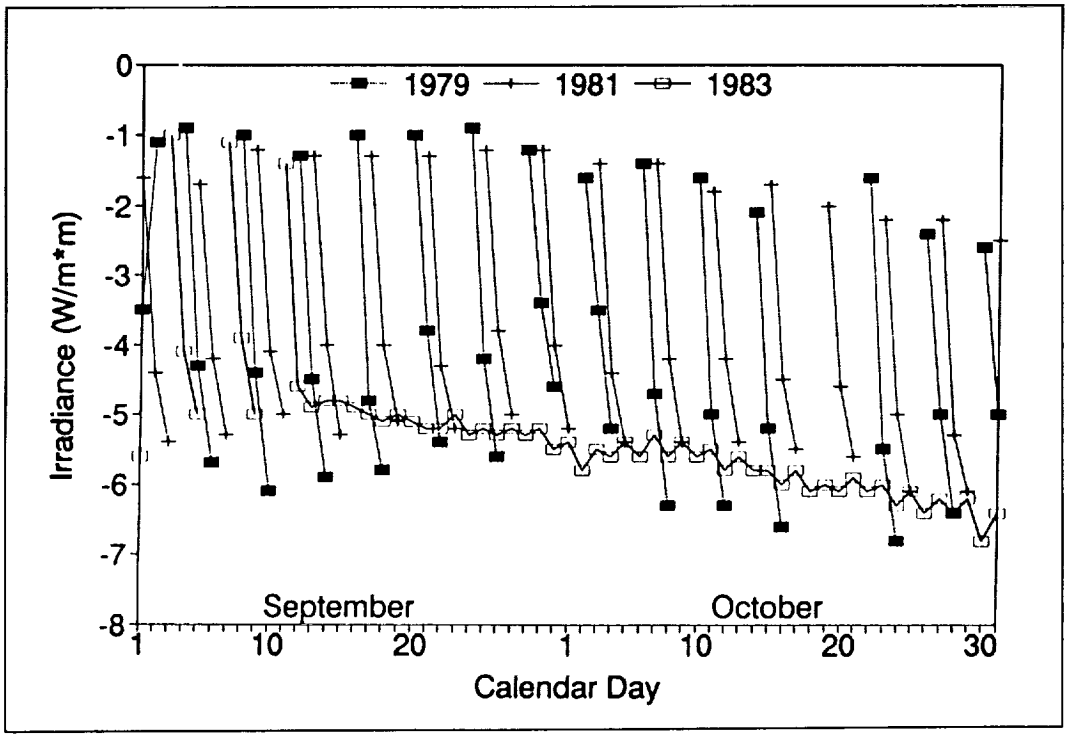

Figure 6b. Channel 13. Ideally this shortwave channel should read zero at night. In 1979 and 1981, the instrument was on a 3-day-on/1-day-off cycle. A repeated pattern of nonzero signals are observed in each group on 3 on days. The instrument was turned on full-time on September 11, 1983.

3.1.5 Longwave Dome Heating in Channels 13 and 14

The Suprasil-W silicon filter domes on channels 13 and 14 were designed to pass shortwave radiation between 0.2 and 3.8 μm, but block out longer wavelengths. However, outgoing longwave radiation (OLR) from both the sensor and the Earth heat the domes, which are thermally insolated from the rest of the sensor block, and cause an orbital mean channel offset component. Local fluctuations about the orbital mean terrestrial OLR field produce a variable, low amplitude response in the domed sensor channels which is referred to as a terrestrial *ghost* because it is time-delayed relative to the OLR forcing. This signal has been well documented by both laboratory experiments and examination of the flight data (Maschhoff, et al., 1984; and Kyle, et al., 1984). The amplitude of the ghost signal is greatest in channel 13 which contains only the two quartz filters. Channel 14 has a red glass dome between the two quartz filters and this causes additional smoothing. The effect of the sensor OLR on the domes is not well known. Originally it was assumed that the inner dome was in longwave radiant equilibrium with the sensor, but the presence of the terrestrial ghost signal shows that this is not quite true. It is possible that other thermal variations in the domes may account for part of the thermal bias observed in channels 13 and 14 (see Sections 3.1.4 and 7). Figure 9 shows the correlation of the terrestrial "ghost" signal on channel 13 with the time delayed channel 12 signal during satellite night when channel 12 receives only longwave terrestrial radiation and channel 13 should ideally read zero. Notice that the maximum correlation occurs for a lag time of about 21 major frames or approximately 336 seconds.

3.2 The Stability of Channel 12

One of the key points of the Pacific and global CAT analyses is the assumption that channel 12 does not suffer thermal perturbations as do the shortwave channels 13 and 14, whose offset voltages are not parameterized as functions of temperature and which are covered by filter domes blocking outgoing longwave radiation. Laboratory calibration data and special studies indicate that when internal instrument temperatures change rapidly or when there is strong solar heating of the sensor and/or the surrounding surfaces, the channel 12 prelaunch calibration equation becomes inaccurate. However, the perturbations are smaller than those induced in channel 14 and considerably smaller than the perturbations in channel 13. Because the thermal perturbation data on channel 12 are more qualitative than quantitative, we rely on analyses of inflight data to confirm these findings.

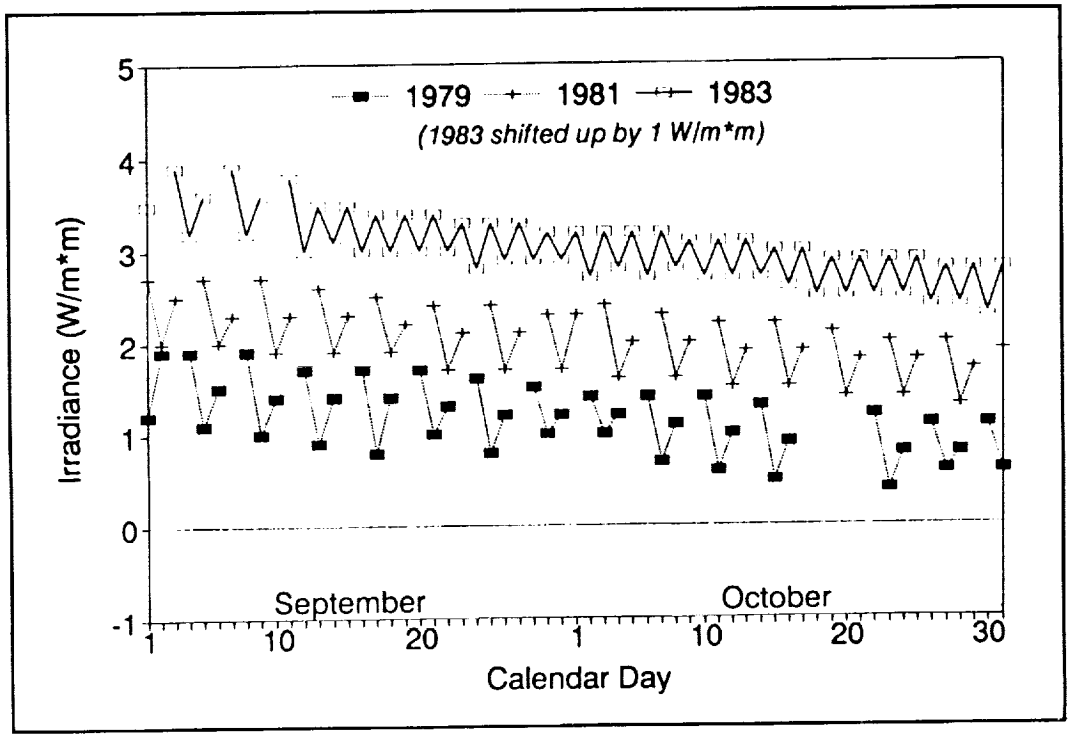

Figure 6c. Channel 14. Note that the nonzero signals are smaller than in channel 13 and the day-to-day pattern different. The positive signal seems to indicate that the inner dome and perhaps the red glass filter are warmer than the sensor. A slight unidentified bias shift may also be present. The day-to-day pattern in October and late September 1983 is due to the 1-day-on/1-day-off SMMR operating schedule.

Figures 6a, 6b, and 6c show the effect of the 3-day-on/1-day-off ERB duty cycle on channel 12, 13, and 14 MAT irradiances during satellite night. Channels 13 and 14, discussed previously in greater detail in Section 3.1.4, should ideally read zero at this time. They do not and, furthermore, day-to-day bias changes of several W/m^2 in channel 13 and 0.5 to 1 W/m^2 in channel 14 follow a pattern closely related to the instrument duty cycle. Channel 12, which is receiving only longwave terrestrial radiation, shows no definitive 3-day pattern in its nighttime average signal. The day-to-day variations that do arise can be attributed to changes both in the Earth's weather field and in the regions of coverage. The Nimbus-7 ascending node equator crossing points are some 26° apart in longitude but move 4° of longitude from one day to the next. The flat plate sensors have a nearly cosine (nadir angle) response to incident radiation and, thus, half of the signal power normally comes from a 7° Earth central angle (ECA) region

surrounding the subsatellite point. Six days are required for these channels to adequately view all regions of the globe.

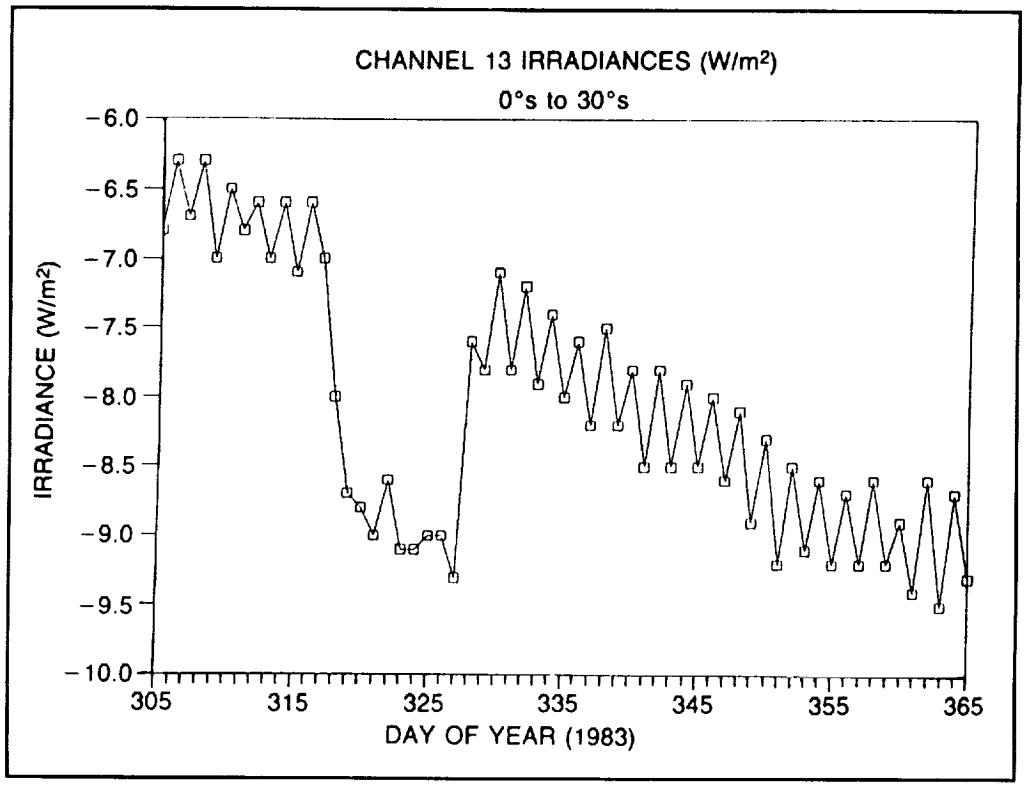

Figure 7. Channel 13 nighttime nonzero measurements for November and December (year days 305-365) 1983 averaged over the latitude band 0° to 30°S. The SMMR 1-day-on/1-day-off cycle is clearly reflected in the sensor's signal. The SMMR was on full-time from year day 318 through 327. A strong seasonal drift is also seen in the measurements.

A numerical study of the three-day MAT signal pattern in channel 12 during descending node (primarily satellite night) is shown in Table 4. Channel 12 descending node monthly global averages are formed separately for the first, second, and third days of the ERB-on duty cycle for three important seasonal periods: mid-winter (January), spring (April) and mid-summer (July). The global irradiances averaged over the ERB-on duty cycle are also shown for each period, facilitating the comparison of these data for different years. During April no definitive day-to-day variation appears. However, during January and July, the third day signal may be as much as 0.5 W/m^2 (0.3 percent) lower than the first day signal. Based on these data, we can expect perturbations of the order of (0 to 0.5 W/m^2) or (0 to 0.3 percent) out of a mean signal of about 175 W/m^2. On ascending node, the mean signal is of the order of 380 W/m^2 with expected perturbations of the order of 0 to 1 W/m^2. This compares with expected perturbations of (2 to 6 percent or 4 to 12 W/m^2) and a mean ascending node signal of 205 W/m^2 on channel 13 (cf. Figure 8). On channel 14 the expected perturbations are (0.6 to 3 percent or 0.5 to 3 W/m^2) and a mean ascending node signal of 91 W/m^2. Thus, the thermal perturbations in channel 12 are small compared to those in channels 13 and 14, and we have not been able to definitively quantize these perturbations. It is, therefore, reasonable to assume that, to the first order of approximation, the channel 12 calibration equation correctly handles instrument thermal variations.

3.3 Calibration History

The final calibration algorithm for channels 12-14 was developed in a step-by-step study that extended through the winter of 1984/85. During this time, the developing algorithm went through four operational stages and, thus, four different calibration schemes have been applied to various segments of the first five data years (November 1978 through October 1983). These were the (1) scanner CAT (first 19 months), (2) Pacific CAT (next 41 months), (3) approximate global CAT (first 5 years), and (4) definitive global CAT (9 years, November 1978 through October 1987). The first three algorithms are chiefly of historical interest, but some data were distributed with these calibrations and may still be in existence. Here we will discuss the first three calibration versions only qualitatively since our primary purpose is documentation of the definitive global CAT algorithm.

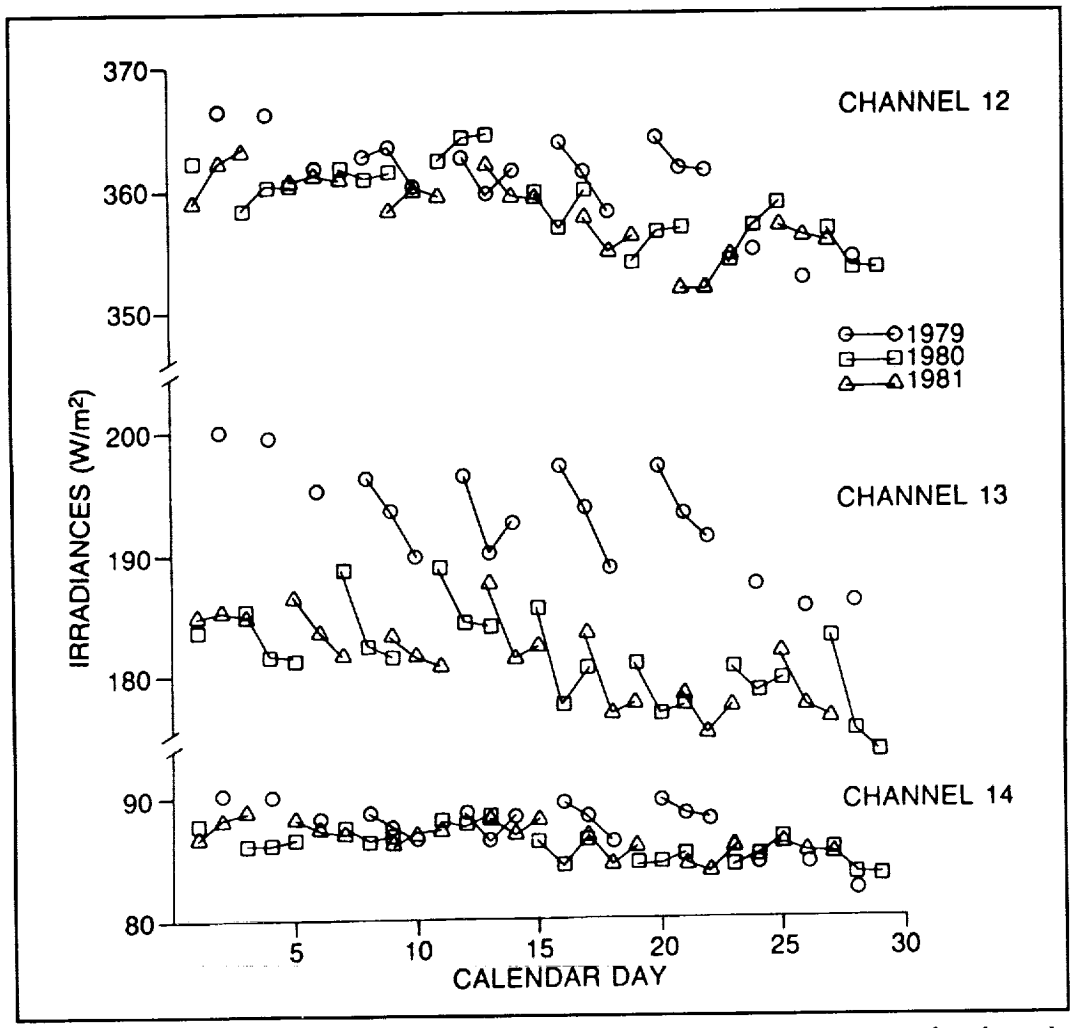

Figure 8. Daily and globally averaged ascending node (daytime) measurements for channels 12, 13, and 14 during the month of February for 1979, 1980, and 1981. In channel 13, the thermal perturbation pattern driven by the 3-day-on/1-day-off operating cycle is still observable. It is, however, perturbed by the varying shortwave fluxes reflected from the Earth. The thermal perturbations are hard to detect in channel 14 during the day and no definite repeating pattern is observed in channel 12.

The inflight calibration problems for the WFOV channels 11-14 can be classified into three types: (1) inappropriate preflight determination of the sensitivity S_0 and configuration factors F in Eqs.(1)-(3); (2) long-term sensor changes, and (3) unexpected sensor responses to short-term perturbations in the sensor environment. The procedures used to study the problems were: comparison of WFOV nonscanner and NFOV scanner measurements; use of the Sun as an inflight calibration source for the WFOV sensors; examination of short- and long-term trends and perturbations in the data; and additional laboratory calibration studies of flight spare sensors.

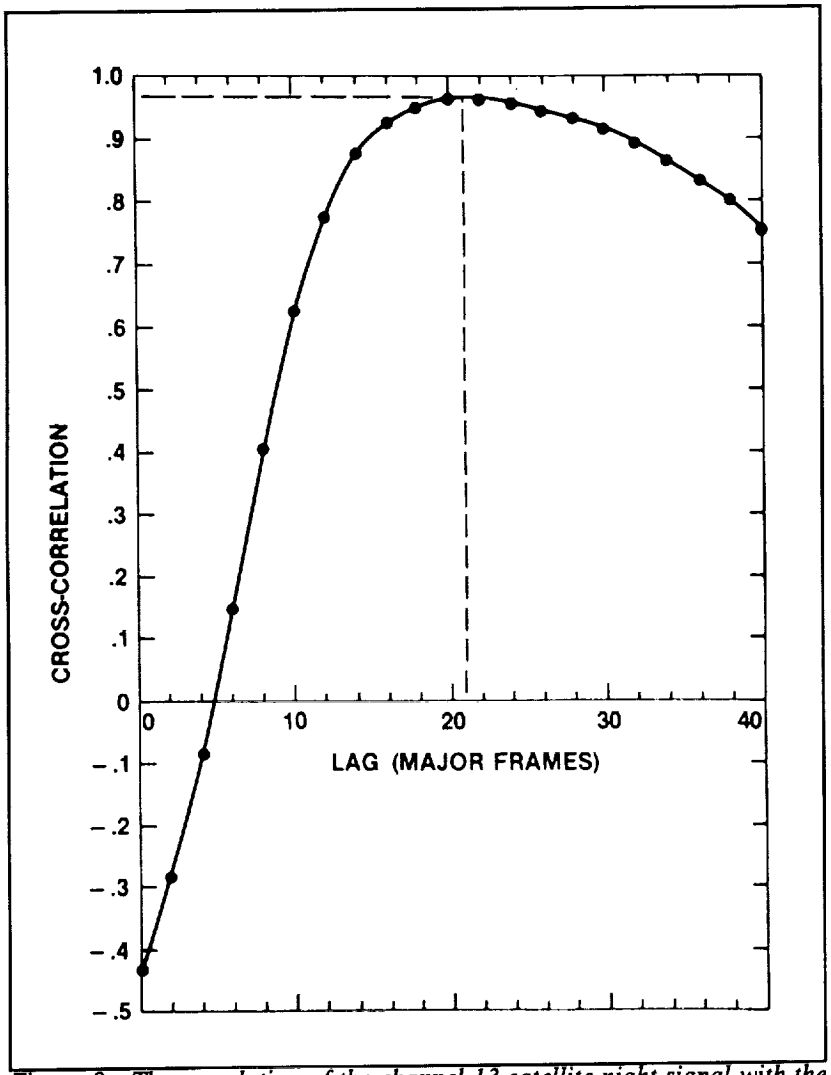

Figure 9. The correlation of the channel 13 satellite night signal with the channel 12 signal is plotted as a function of the time lag in the channel 12 data. A major frame is equivalent to 16 seconds. Nimbus-6 ERB data were used in this study. (Figure was taken from Kyle et al., 1984).

Of the 22 ERB sensors, only the solar channel 10c (see Part I of this history) and the longwave scanner channels 19-22 had accurate inflight calibration. The long-term channel 10c solar measurements demonstrated that the Sun had a year-to-year stability of ± 0.075 percent. Most of this was a downward trend during the period 1979 to 1987 due to the phase of the sunspot cycle. Short-term perturbations of ± 0.25 percent existed during the peak years (1978-1983) of the 11-year sunspot cycle (Hoyt et al., 1992). The Sun was assumed to be a constant source in the WFOV solar calibration algorithm. Thus,

only an Earth-to-Sun distance correction was applied. The longwave scanner channels used a 2-point inflight calibration. This consisted of alternate looks at a warm blackbody, mounted in the instrument housing, and cold space. The ERB scanner was designed to study bidirectional reflectance and emittence patterns. Thus, in its 112-second scanning pattern, it looked forward, to the side, and to the back while the subsatellite point moved 700-km across the Earth. This viewing pattern made it easy to compare the WFOV and NFOV measurements. Over 2-week periods, concurrent measurements were made and then regressed against each other. The longwave scanner channels were compared directly to channels 11 and 12 during the satellite night. During the satellite day, the correct shortwave measurement was assumed to be (channel 12 minus scanner longwave). This difference was compared both to channel 13 and to the shortwave scanner results (Jacobowitz et al., 1984a).

The adjustments arising from these scanner comparisons were termed the scanner CAT and were used through May 1980. Later it was discovered that the use of an incorrect temperature coefficient in the calibration equations for channels 19-22 produced radiance values that were in the mean 1 Wm^{-2} sr^{-1} too small (Kyle et al., 1985). The scanner products have since been corrected (Kyle et al., 1990b). A correction for this longwave scanner problem was introduced in the WFOV global CAT but not in the Pacific CAT algorithm. When the scanner failed on June 22, 1980, another calibration procedure had to be developed. The following schemes assumed that channel 12 was stable and that the mean shortwave signal was given by [channel 12 (day) minus channel 12 (night)]. Over the oceans, day and night longwave signals are roughly the same in the mean. Thus a large area in the central Pacific Ocean was used as a comparison region in the Pacific CAT algorithm which was used from June 1980 through October 1983. The Pacific CAT, however, had a number of problems and, thus, an improved global CAT was introduced beginning with data month November 1978. In the global CAT, the entire Earth is used as a comparison target and a mean longwave (day minus night) difference derived from the scanner results is inserted into the algorithm.

When the global CAT was developed, limited resources indicated that it might be a few years before the data from the first 5 years could be reprocessed. Therefore, an approximate correction table was published to bring the scanner and Pacific CAT products to rough agreement with global CAT results (Kyle et al., 1985). These approximate global CAT data are not as accurate as the final definitive global CAT products. However, they proved useful at the time.

3.3.1 Sensitivity Studies

Sensitivity studies continued through the development of the Pacific CAT algorithm. The following summary of these studies is largely an excerpt from Kyle et al. (1984). The long-term degradation and short-term perturbation studies also continued into the global CAT period. They are discussed further in Section 3.4, the global CAT.

The Nimbus-6 and -7 ERB instruments are twins built originally as flight and flight spare instruments for Nimbus-6, which was launched in June 1975. The spare ERB instrument was modified slightly and mounted on the Nimbus-7 satellite, which was launched on October 24, 1978. One of the modifications was to paint the baffle on channel 11 black to see if this would make it possible to use the prelaunch calibration parameters on the flight data. In the ERB 6 experiment, both channels 11 and 12 had shiny baffles, and the prelaunch calibration parameters proved inadequate. The chief problem seemed to involve the proper values of S_0 and F_D to use with the flight data. The baffles on the Nimbus-7 channel 12 were left shiny to provide continuity with the Nimbus-6 ERB experiment.

Table 4. Composite Duty-Cycle Averages of Channel 12 Irradiances for 1979-1983				
Global Averages for Descending Node Computed at the MAT-Level				
Month	Duty-Cycle Day			
January	Day 1	Day 2	Day 3	Average
1979	176.4	175.6	176.3	176.1
1980	175.3	175.1	174.7	175.0
1981	174.6	174.5	174.4	174.5
1982	173.4	173.3	173.2	173.3
1983	174.8	174.3	174.1	174.4
Mean	174.9	174.6	174.5	174.7
April	Day 1	Day 2	Day 3	Average
1979	171.7	171.2	171.5	171.5
1980	169.6	170.3	170.4	170.1
1981	169.8	169.9	169.7	169.8
1982	168.7	168.5	168.7	168.6
1983	170.2	170.1	170.5	170.3
Mean	170.0	170.0	170.2	170.1
July	Day 1	Day 2	Day 3	Average
1979	177.4	177.2	177.3	177.3
1980	177.6	177.2	177.1	177.3
1981	177.2	176.8	176.8	176.9
1982	177.6	177.2	176.8	177.2
1983	177.1	177.0	176.4	176.8
Mean	177.4	177.1	176.9	177.1
5-yr Mean	174.1	173.9	173.9	174.0

The ERB 7 instruments went through a prelaunch calibration cycle both in 1975 and 1978. Postlaunch calibration analyses have included studies of flight spare WFOV channels by both Eppley Laboratory and Gulton Industries as well as extensive examination of the flight data [Jacobowitz et al., 1984a; Maschhoff et al., 1984]. The WFOV channels 11 and 12 were calibrated in 1975 and 1978 with a special double cavity blackbody unit designed for calibrating the channels after they were mounted on the ERB radiometer. It overfilled the field of view so no ring of space surrounded the blackbody as normally occurs for Earth observations at Nimbus-7 altitude. The unit operated with an apparent emissivity in vacuum of 0.995 or greater, and 10 blackbody test temperatures ranging from 180°K to 390°K were

measured and controlled to an accuracy of 0.1 K. In addition, the ERB channels were controlled during the 1978 tests at three different temperatures: 10°C, 22°C, and 35°C. In 1978, channel 12, but not channel 11, was also calibrated by a solar simulator whose radiation was directed normal to the detector in vacuum. This directly measured the channels shortwave sensitivity. Channels 13 and 14 were calibrated only with the solar simulator.

The blackbody calibration parameters for channels 11 and 12 were obtained by setting

$$H_T = H_{BB} = \epsilon_{BB}\sigma T_{BB}^4 \tag{4}$$

where

H_{BB} = blackbody irradiance (W/m^2)
ϵ_{BB} = blackbody emissivity
T_{BB} = blackbody temperature (K)

This was substituted in Eq.(1), and using the test data, the calibration parameters were evaluated. However, this procedure yielded the products of the sensitivity S times the detector configuration factor F_D and the blackbody configuration factor F_{BB}, SF_D and SF_{BB}, respectively. One of the factors must be independently determined to complete the solution.

Table 5 lists the more important evaluations of the Nimbus-7 ERB WFOV calibration parameters S, F_D, and the product SF_D. The first column is a brief description of the method used. The primary quantity determined by the method is given in parentheses for channels 11 and 12. For these channels, the same prelaunch blackbody calibration product is used in all cases. For channels 13 and 14, it is assumed that the filters block all longwave emissions from the detector chip so only S is given. MAT irradiances for channels 12-14 are generated using the sensitivity estimates of the prelaunch solar simulator calibrations. The detector configuration factor (for channel 12) is derived from this sensitivity and the value of the blackbody calibration product, $SF_D = 1.3865$. Channel 11 MAT irradiances use a value of the target configuration factor computed analytically assuming completely diffuse thermal radiative exchange between the black baffle and receiver surface. Sensitivity is derived from F_D and the blackbody calibration product, $SF_D = 1.2002$.

In channel 11, note that painting the baffles black reduced the product SF_D by 12.4 percent. This occurs because the baffle walls are now more absorptive and, re-emitting thermal energy back to the receiver, they reduce the detector's effective field of view of space. The black paint also appears to have made the prelaunch and postlaunch behavior more comparable except for the anomalous Sun tilt evaluation. We postulate that the black-painted baffles heat rapidly in direct sunlight causing most of the difference.

For channel 12, the most accurate determinations were the Eppley postlaunch estimate of the detector factor F_D and the satellite Sun tilt calculation of the sensitivity; these agreed to within 0.05 percent. The Eppley measurement was adopted. For channel 13, the immediate postlaunch Sun tilt check of the sensitivity agreed to 0.5 percent with the prelaunch solar simulator result. The difference was 2 percent for channel 14.

3.4 The Global CAT

The global CAT procedure is an improved modification of the Pacific CAT described by Kyle, et al. (1984). This section describes the components of this procedure for adjusting the inflight calibration of

the ERB WFOV sensors (channels 12-14). As in the Pacific CAT, the global CAT depends on the stability of the total channel 12 (0.2 to 50 μm). Nevertheless, some corrections for the long-term degradation of this channel are made in the global CAT.

The development of improved inflight calibration procedures took place in stages covering some 6.5 years after the launching of the Nimbus-7 on October 24, 1978. To allow calibration traceability, all of the ERB data are first processed using the original postlaunch calibration equations (Jacobowitz, et al., 1984) and stored on the ERB MATs. The calibration adjustments are then applied to the MAT data when higher level products are made. This is described in Kyle, et al. (1985). The adjustments are summarized below and then are described in more detail in Sections 5 through 8.

Long-term Adjustments

a. Correction for slow long-term degradation in channel 12 with different shortwave (0.2 to 4 μm) and longwave (4 to 50 μm) degradation rates; this is a modification of the Pacific CAT.

b. A baffle enhancement factor for channel 12 identical to that used in the Pacific CAT. When applied to MAT irradiances, it simultaneously increases the sensitivity and decreases the target configuration factor to the best values given in Table 5.

c. An NFOV comparison-derived, constant bias offset for channel 12; this is similar to that used in the Pacific CAT but is larger because of the new correction in NFOV longwave calibration (Kyle, et al., 1985, 1990b).

d. Correction for the mean long-term degradation in channels 13 and 14; the procedure uses channel 12 as a standard. In the Pacific CAT, channel 14 was not corrected; coefficients in channel 13 are different than in the Pacific CAT because of the new corrections in channel 12.

e. A new forcing term, derived from the NFOV longwave data, is used to force the WFOV ascending node longwave flux to have a global average approximately 5 W/m^2 larger than that of the descending node measurements. This is a new correction.

f. An asymmetric dome degradation correction for channel 13; this is unchanged from the Pacific CAT.

Short-term Adjustments

a. Interpolation across the sunrise and sunset sunblip gaps in channels 12-14 to fill these descending node data voids. This is a new procedure.

b. Removal of stray light effects on the edge of the interpolation regions. This is a new procedure.

c. A longwave dome heating correction for channel 13 identical to that used in the Pacific CAT.

d. A midnight offset correction for channels 13 and 14 identical to that used in the Pacific CAT.

e. A correction to channels 13 and 14 measurements for solar heating of the instrument at satellite sunrise and sunset. This is termed a shortwave heating effect and is a new correction.

Table 5. Evaluations of ERB WFOV Channel Sensitivities S at 25°C.

Method	Channel 11			Channel 12			Channel 13	Channel 14
	F_D	S	SF_D	F_D	S	SF_D	S	S
Prelaunch solar simulator—used to compute channel 12-14 MAT irradiances				0.8628	(1.607)	1.3865	1.939	4.179
Prelaunch blackbody								
Shiny baffle (Gulton 1975)			(1.3496)					
Channel 11 baffle black (GE 1978)			(1.2002)			(1.3865)		
F_D calculated from geometry assuming completely diffuse radiation exchange within the channel—used to compute channel 11 MAT irradiances	(0.80461)	1.49166	1.2002	(0.80461)	1.7232	1.3865		
F_D calculated by integrating mean measured detector angle of incident response function				(0.829)	1.6724	1.3865		
Postlaunch comparison with ERB NFOV longwave channels	0.80442	(1.492)	1.2002	0.8687	(1.596)	1.3865	1.870	
Calculated from satellite Sun tilt data using sensor angular response function*	0.79378	(1.5387)	1.2002	0.82999	(1.6705)	1.3865	1.929	4.103
Eppley Laboratory analysis based on postlaunch "cold ring" laboratory experiment				(0.8296)	1.6713	1.3865		
Adopted best value	0.80461	1.49166		0.8296	1.6713		1.929	4.103

The units of S are counts per watts per square meter. For channels 11 and 12, the primary quantity listed from each study is in parentheses.
*Channels 11 and 12 used 4 days in first and second year. Channels 13 and 14 used days 332 and 354 in 1978 just after launch.

f. Ascending node offsets for channels 13 and 14 based upon globally-averaged comparisons to the shortwave component of channel 12. These comparisons use half monthly averages. The Pacific CAT used the central Pacific as a comparison area instead of the whole globe.Figure 10 is a flow chart of the global CAT algorithm that references each of the long- and short-term adjustments mentioned above. Panel a illustrates the course of the overall processing scheme and defines an intermediate level product referred to as DELMAT data. Panels b and c provide additional details of the computations of channel sensitivities (b) and the DELMAT level calibration offsets (c). Panel (d) summarizes the computation of the ascending node (mostly daytime) offsets; panel (e) shows final calculation of the global CAT data beginning with DELMAT data.

4. INFLIGHT WFOV CALIBRATION ADJUSTMENT

A linear model of the form

$$a_{baffle} \cdot H_{MAT} = a_{degrad} \cdot H_{sat} - b \qquad (5)$$

is utilized to separately recalibrate the MAT longwave and shortwave spectral irradiances of channel 12, and the filtered irradiances of channels 13 and 14. In (5), H_{MAT} and H_{sat} are MAT and actual satellite altitude irradiances, respectively; a_{degrad}, a_{baffle} and b are recalibration coefficients. The term a_{baffle} is applied to channel 12 only and accounts for the loss of receiver-emitted thermal radiation to space by means of baffle scattering. With a value of 0.962, it acts to decrease the estimates of satellite altitude irradiances and may be regarded as the effect of a one-time increase in sensor sensitivity and decrease by the same factor in detector configuration factor relative to MAT values. For the other channels, a_{baffle} is formally set to unity.

The degradation factor, a_{degrad}, and offset b are dynamic recalibration factors that account for possible ongoing long-term sensitivity changes, and short-term detector responses not considered in the prelaunch energy balance equation (Equation 1), respectively. Note carefully that MAT irradiances (after correction with a_{baffle} are assumed to be separable into two components: one consisting of the satellite altitude ERB field (but degraded due to sensitivity loss) and the other representing perturbations to the ERB signal due to all other forcing (i.e. non-ERB signals). These non-ERB signals are characterized and removed via the additive offset b. The degradation correction factor, $1/a_{degrad}$, permits us to rescale these attenuated ERB irradiances, $a_{baffle} \cdot H_{MAT} + b$, to recover the actual satellite altitude flux. Transmissivity loss in the filter domes covering channels 13 and 14 is the primary reason for sensor degradation in these channels, although changes in receiver absorptivity and baffle reflectivity may also occur. The total channels 11 and 12 are, of course, uncovered and their sensitivity changes are observed to be markedly less than those of channels 13 and 14.

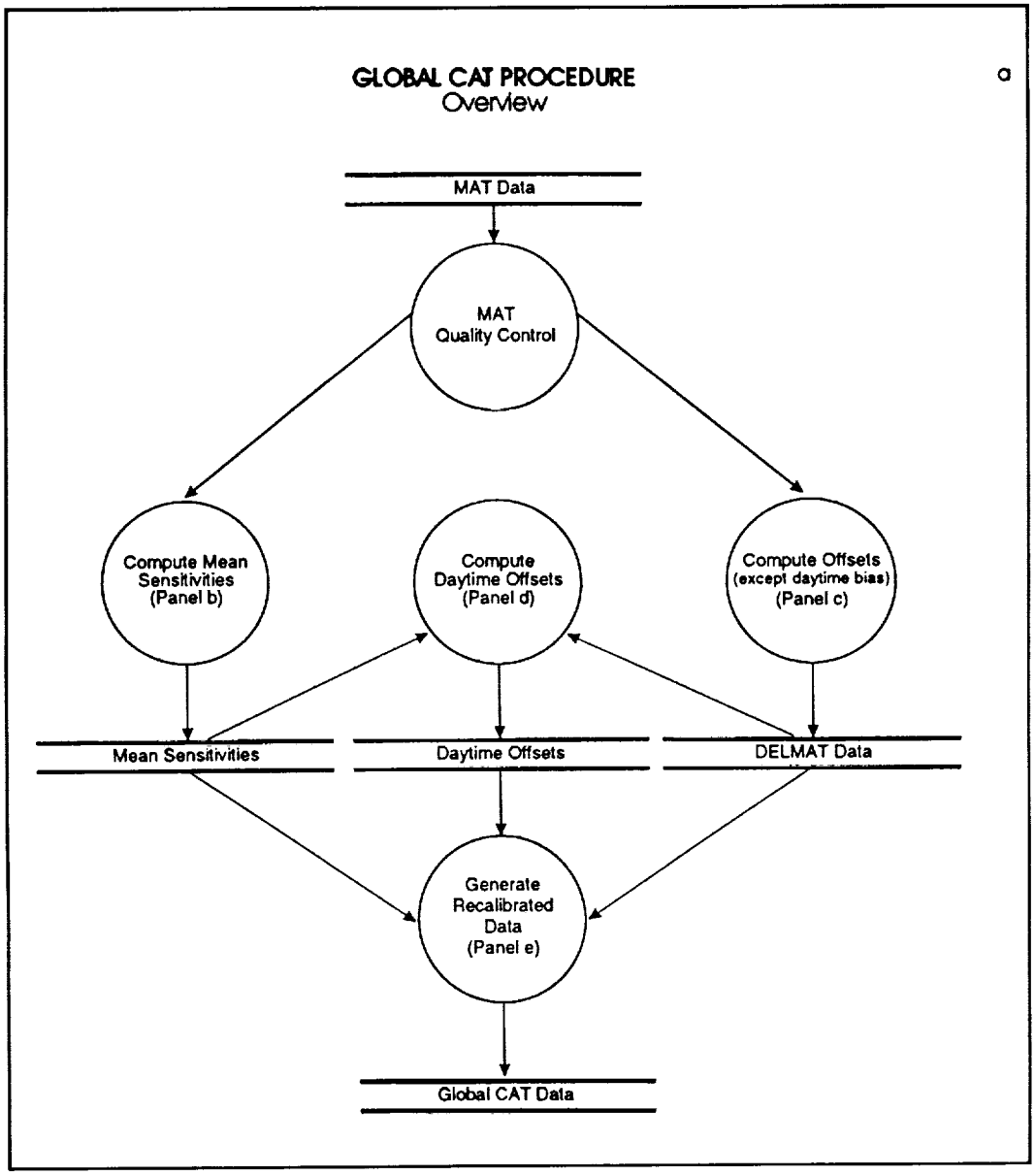

Figure 10a. This is a flowchart of the global CAT algorithm that performs the final calibration of the Earth flux measurements. An overview is given in (a). Procedural details are outlined in the other panels.

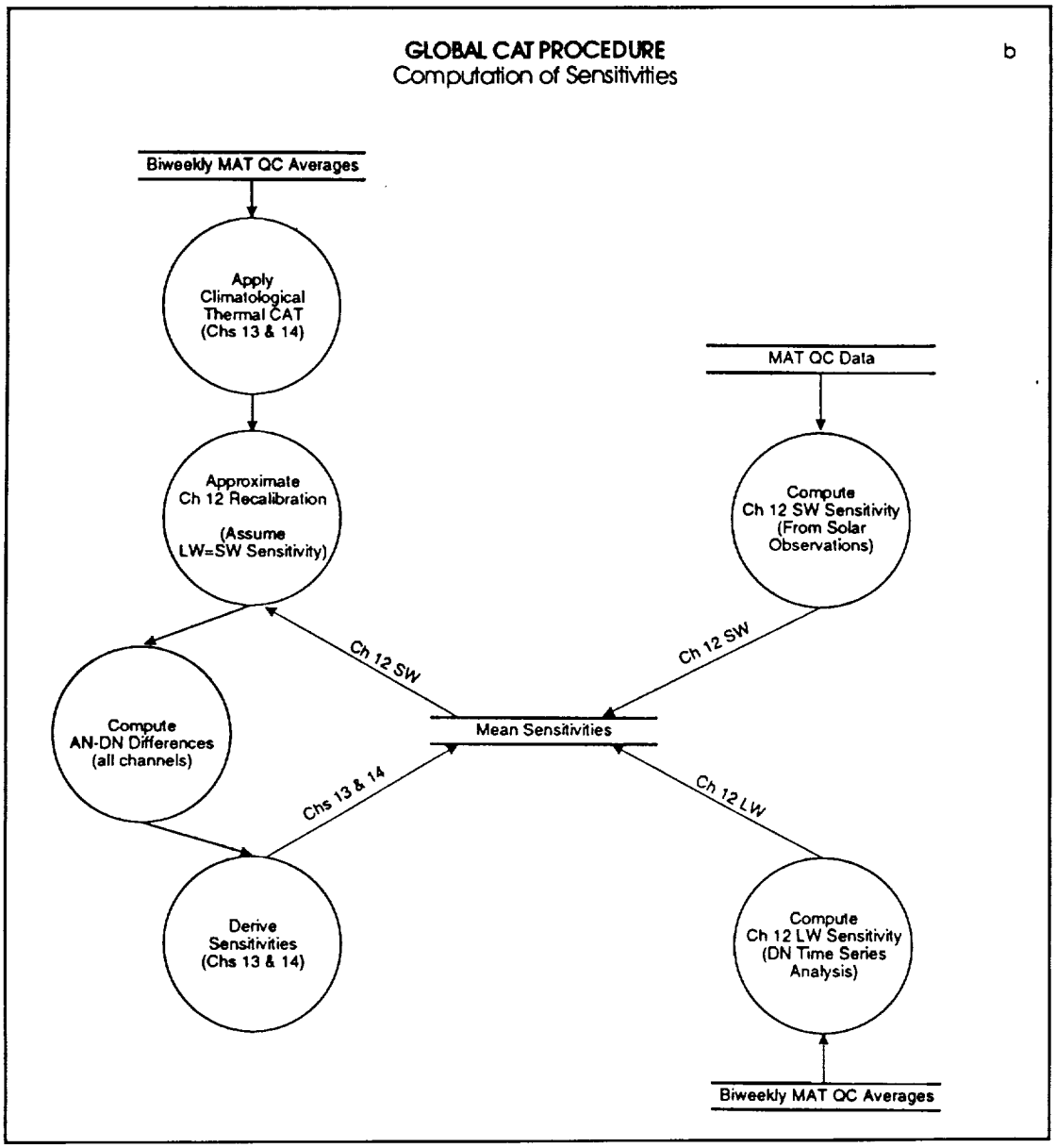

Figure 10b. The computation of sensitivity changes.

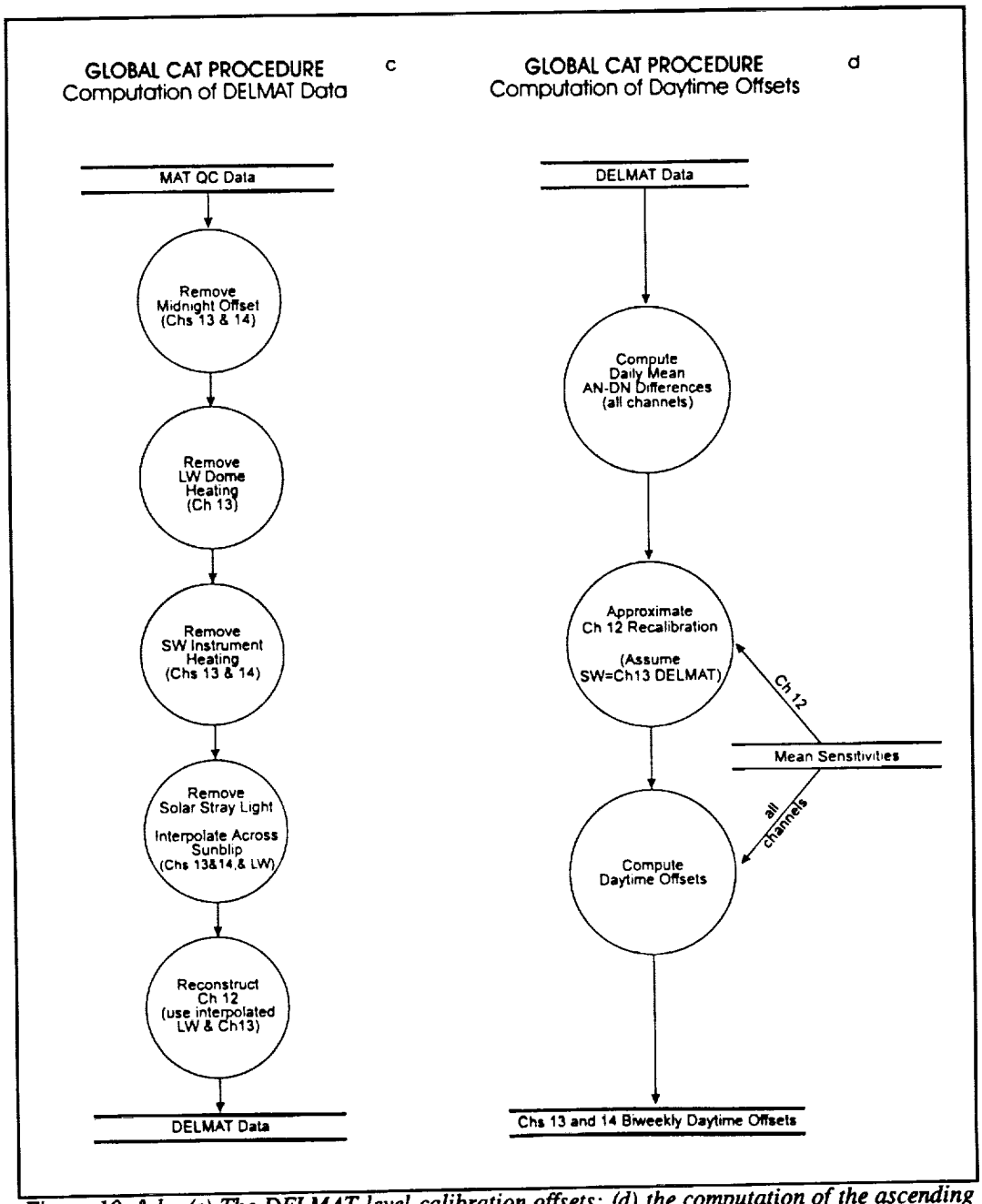

Figure 10c&d. (c) The DELMAT level calibration offsets; (d) the computation of the ascending node (mostly daytime) offsets.

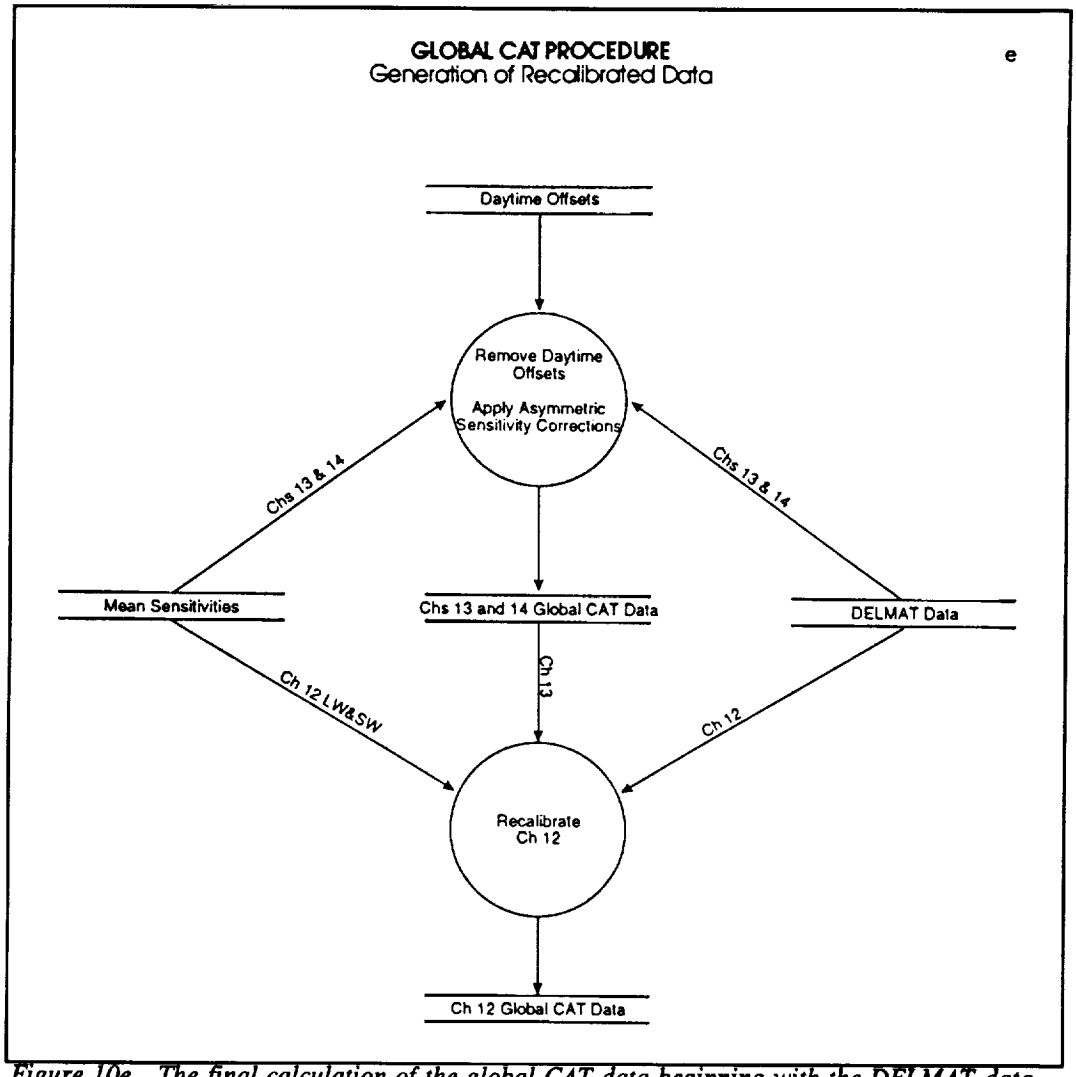

Figure 10e. The final calculation of the global CAT data beginning with the DELMAT data.

5. LONG-TERM DEGRADATION MAINTENANCE

Characterization of the long-term sensitivity changes of the WFOV channels has been a complex task because of the presence of thermal forcing and the lack of on-board calibration sources. We have relied on several methods to evaluate changes in sensitivity, the principle ones being:

1. Unobstructed observations of the Sun, normally once every 24 days, obtained during satellite pitch maneuvers.

2. Comparison of the two total spectral channels, beginning in April 1984. At this time, channel 11 was unshuttered and kept opened on a full-time basis.

3. Comparison of the WFOV channels with the in-space calibrated NFOV scanning channels during the 20-month scanner lifetime (Jacobowitz et al., 1984a; and Ardanuy and Rea, 1984).

4. The stable channel 12 calibration is transferred to the shortwave channels 13 and 14.

5. Consistency in the results of the above procedures is confirmed by analyses of time averaged global mean irradiances for all the WFOV channels.

5.1 Shortwave Sensitivities of the Total-Radiation Channels

Figures 5a (channel 11) and 5b (channel 12) show the shortwave sensitivities for the two total channels as derived from satellite pitch data. A discussion of these results has already been given in Section 3.1.2 where we concluded that no observable degradation in channel 11 sensitivities can be detected through the first 9 years. Channel 12 sensitivities change slowly, but by year 6 a definite decrease is observable. This decrease is emphasized by the best linear fit line shown in Figure 5b. The actual channel 12 SW degradation terms, T_{SW}, used are summarized in Table 6. They are derived from Table C1 in Appendix C. Before launch it is assumed that $T_{SW}=1$. As indicated in Table 6, T_{SW} actually appears to change monotonically but not in a strictly linear fashion. Accumulated shortwave degradation 9 years after launch is 1.5 percent.

Table 6. Channel 12 longwave, T_{LW}, and shortwave, T_{SW}, degradation factors.

Year	Date	T_{LW}	ΔT_{LW}	T_{SW}	ΔT_{SW}
	October 24, 1978	1.00		1.00	
0	November 16-30, 1978	0.9961	(0.0039)	0.9997	(0.0003)
1	October 16-31, 1979	0.9801	0.0160	0.9975	0.0022
2	October 16-31, 1980	0.9780	0.0021	0.9953	0.0022
3	October 16-31, 1981	0.9765	0.0015	0.9938	0.0015
4	October 16-31, 1982	0.9755	0.0010	0.9930	0.0008
5	October 16-31, 1983	0.9752	0.0003	0.9926	0.0004
6	October 16-31, 1984	0.9752	0.0000	0.9926	0.0000
7	October 16-31, 1985	0.9752	0.0000	0.9898	0.0028
8	October 16-31, 1986	0.9752	0.0000	0.9868	0.0030
9	October 16-31, 1987	0.9752	0.0000	0.9848	0.0020

ΔT_i is the difference (T_{i+1} - T_i). At launch, October 24, 1978, it is assumed that $T=1$.

During the period from April 1984 through April 1986, both WFOV total radiation sensors viewed the Earth. Although there were several periods when these channels experienced shutter problems rendering the data unusable (e.g., channel 11: 26-28 April 1984 and channel 12: 3-15 July 1985), these anomalies may be eliminated and a set of consistent half-monthly, global averages computed. Because the radiometer FOVs are collocated and possess identical spectral responses, the signals are quite similar. Noting the differential degradation of the sensors inferred by the pitch maneuver data of Figures 5a and 5b, we would expect this behavior to be clearly demonstrated in an irradiance comparison between the two channels. Figure 11 presents the ratio of the MAT irradiance difference (channel 12 - channel 11)

relative to channel 12 for ascending (mostly day), and descending (mostly night) orbit halves, and the ascending-descending orbit difference. There is more variability in the nighttime (primarily longwave radiation) curve than in the daytime (both longwave and shortwave radiation) curve.

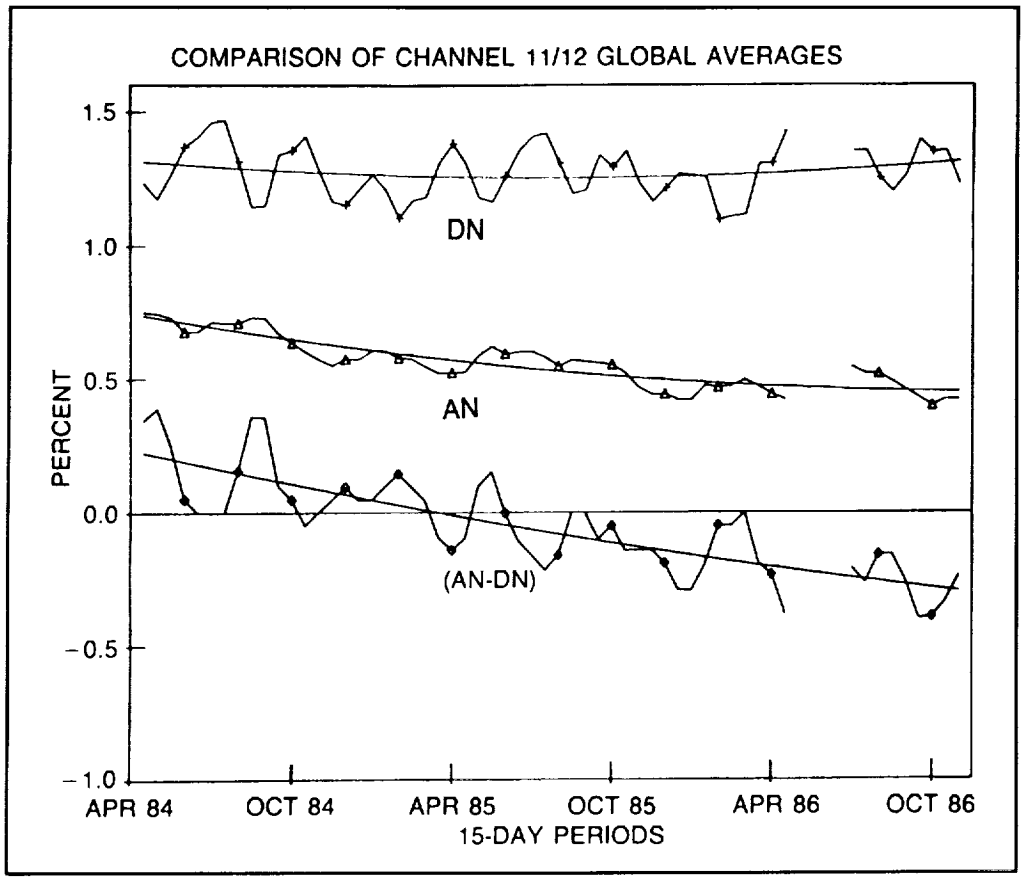

Figure 11. The MAT irradiance global mean difference (channel 12-channel 11) divided by channel 12 is plotted in percent. Half-monthly averages are plotted for the period April 1984 through October 1986. The descending node (longwave) curve is at the top, followed by the ascending node (longwave plus shortwave) graph. The bottom curve shows the difference in the ascending and descending node differences normalized by the channel 12 (ascending minus descending node) difference. The slope of the bottom two curves indicates a relative change in the shortwave sensitivity of one channel with respect to the other.

For the ascending and ascending-descending orbit half curves there is a noticeable downward trend in the data. This suggests a change in the sensitivity of one of these channels. From the pitch analysis in Figure 5a there is no indication of any long-term drift in the sensitivity of channel 11, in contrast to the small (-0.2 to -0.3 percent/year) loss of sensitivity in channel 12. This comparison of channel 11 and 12 suggests a -0.3 percent (ascending node) to -0.4 percent (ascending-descending) per year trend in the difference curves for this period, and tends to support the pitch-maneuver results.

A third, empirical means may be employed to examine the interannual stability of the total channel 12. Consider the 9-year (n=9) time series of half-monthly, global irradiance averages (F_i; i=1, 24n). Present in these data, which have been subjected to only the prelaunch, time-invariant calibration, are the time-dependent responses due to sensor degradation. Also present is the Earth's climate signal. Though

the latter contribution is of ultimate interest, for understanding the instrument it is simply a source of noise that must be removed. To a first approximation, the seasonal cycle is removed by taking a set of annual differences ($D_i = F_{i+24} - F_i$), and from these deriving a times series of deseasonalized contiguous half-monthly irradiance differences, d_i. A solution for the d_i is obtained by noting that annual differences should be the sum of 24 contiguous half-monthly differences, a condition expressed by

$$D_i = \sum_{j=i+1}^{i+23} d_j \qquad (6)$$

However, the system of equations is under-determined, there being $(24 \cdot n-1)$ d_i but only $24 \cdot (n-1)$ D_i. Thus, we implement a boundary condition at the end of the time series assigning equal values, 1/24 of the tendencies suggested by the pitch maneuver study, to the final 23 d_i. Although the boundary conditions necessarily influence the solution, they do so only weakly guaranteeing that the results of this analysis are independent of those of the satellite pitch study. Each point of the solution vector, d_i, represents the irradiance change from one half-month to the next in the absence of a seasonal cycle. These are then summed from the beginning of the dataset to give a cumulative signal change. Even though the mean seasonal oscillation is removed, the desired instrument signal plus a spurious component due to interannual and other variability remain. Figure 12 depicts this time-series analysis for the AN in terms of the input vector of normalized annual irradiance differences, D_i/F_i, (triangles), the cumulative sensor degradation (diamonds), and a quadratic fit to the sensor degradation (squares). Note that tick marks along the abscissa represent time intervals in years beginning in November of 1978 (N 78), and data points are plotted at half-monthly increments; symbols are added to the curves at bimonthly intervals. The quadratic fits to this data and similar analyses for the AN-DN differences give sensitivity change rates of -0.18 to -0.24 percent per year by November 1985. Thus, while we do not use this method to calibrate the instrument (as it would alter the true climate signal), the resultant solution is clearly in excellent agreement with the sensitivity estimates obtained from the satellite pitch, and the channel 11 and 12 comparison studies.

A summary of the adopted channel 12 longwave, T_{LW}, and shortwave, T_{SW}, degradation rates for the first 9 years is given in Table 6. In practice, values were determined for each half-month period and these are given in Appendix C. Table 6 lists the values for only one-half-monthly period per year. In this Table, ΔT is the difference from one entry to the next, and thus represents the yearly changes in the degradation. By the end of year 9, the shortwave sensitivity had decreased by 1.5 percent. By examining the time series of globally-averaged terrestrial observations, supportive evidence for the instrument's characterization is clearly found. This also demonstrates the stability of the global annual averages (see Section 9 and Ardanuy et al., 1992).

5.2 Longwave Sensitivities of the Total-Radiation Channels

While shortwave absorption at the receiver surfaces of the WFOV channels is determined by the properties of the pigment of the velvet black paint covering each of them, infrared absorption depends mainly on the paint's binder. Because of this distinction, one does not expect a flat absorption response over both the solar-reflected (0.2 to 3.8 μm) and Earth-emitted (3.8 to 50 μm) wavelength regions. Additionally, there is the potential—due to different absorption mechanisms—that any degradation experienced in flight will be spectrally-dependent. This is apparently the case for the ERB total channel 12.

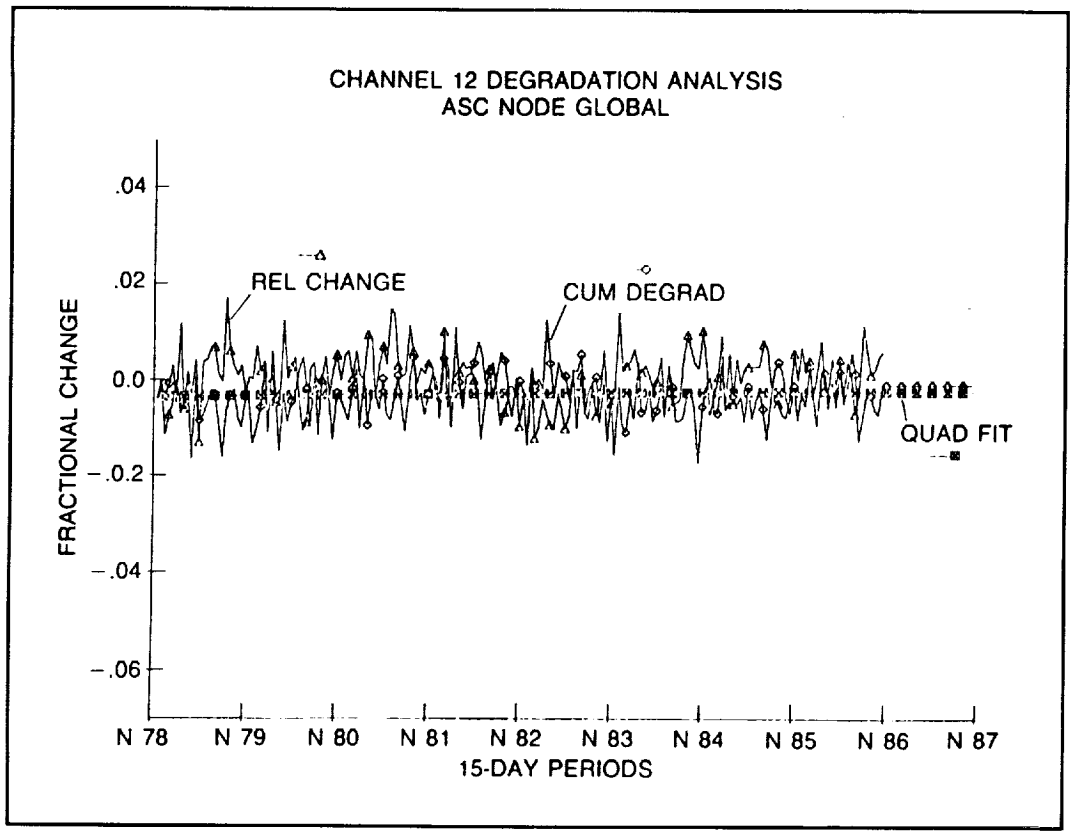

Figure 12. Long-term trends in channel 12 (shortwave plus longwave) MAT level measurements are examined by a time series analysis of globally averaged, ascending node (daytime) measurements. The data are deseasonalized by considering year-to-year changes in the 24 annual half-monthly averages (see text). The triangles indicate consecutive year changes. The cumulative changes are indicated by the diamonds and by a quadratic fit (squares) which most accurately represents the sensitivity loss.

Figure 13 illustrates the long-term variability of the nighttime (infrared) globally-averaged irradiances taken by channel 12 after removal of the seasonal cycle (Equation 6). As in Figure 12, the input vector of normalized annual irradiance differences (triangles), cumulative sensor degradation (diamonds), and a polynomial fit (squares) are illustrated. The "spurious" component in the cumulative degradation is most likely caused by the normal meteorological variability of the Earth. Of interest, however, is: (1) the apparent rapid initial degradation in sensitivity of nearly 2 percent; and (2) indications of an additional 0.5 percent sensitivity loss during the first 5 years of data, before the time series becomes stationary in the latter half of the observing period. Thus, most of the longwave sensitivity loss occurred during the first 4 months of operation (see Table C1 in Appendix C). Indeed, some sensitivity loss may have occurred in the first three weeks of flight, prior to the experiment's activation. If so, this would at least partially explain the need for the application of an offset to the total channel 12 irradiances to obtain agreement with measurements taken by the NFOV scanning channels (Section 3.4; Kyle et al., 1984). Comparisons with the total channel 11 confirm the stability of the sensitivity during the later years (Figure 11, descending node). Relative comparison of channel 11 and 12 data over the first 5 years of operations is not possible because channel 11 was shuttered most of the time during this period. Based on this evidence, it is believed that the sensitivity of the total channel 12 in the longwave spectral regime was essentially constant for the period 1983 to 1987. By 1983, the radiometer had lost about 2.5 percent in total sensitivity for this spectral band.

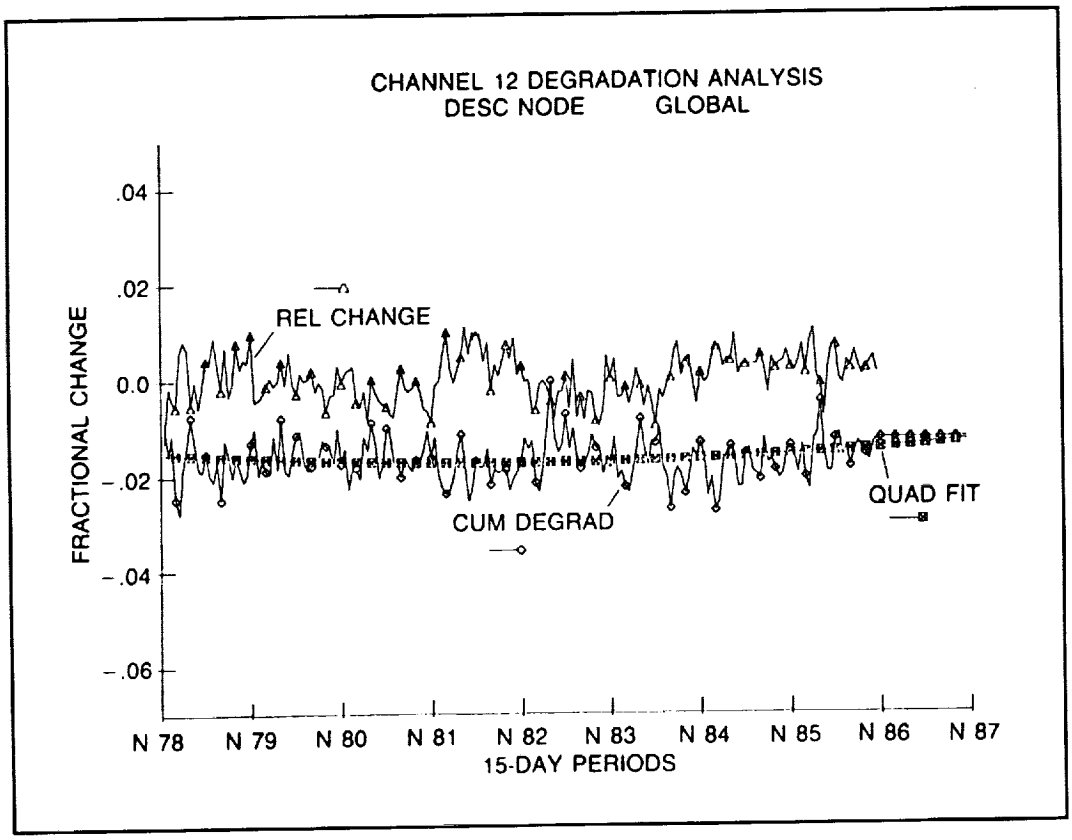

Figure 13. Analysis of long-term trends in the channel 12 descending node (nighttime), longwave, MAT level measurements (refer to Figure 12).

The shortwave sensitivity of channel 12 is monitored using the Sun as the basic calibration standard. The time series analysis of the ascending node global measurements and the channel 11 and 12 comparisons (Figures 11 and 12) both support the solar calibration results and help to verify the time analysis procedure. The longwave sensitivity is monitored only by the time analysis and channel 11 and 12 comparison studies. Analysis of 9 years of calibrated longwave global averages shows a remaining downward trend of about 0.05 percent/year and this seems climatologically unrealistic (Ardanuy et al., 1992). No particular trend appears in the shortwave data which depends on solar calibration. Thus is possible that the longwave sensitivity did continue to slowly degrade after 1983. Since channel 11 should have also suffered some degradation after it was opened, the channel 11 and 12 intercomparison gives only limited information.

5.3 Sensitivity of the Shortwave Filtered Channel

While analysis of a time series of Sun observations for upward and downward trends can provide a powerful tool for calibration purposes (Figure 5c), the solar disk subtends an angle of only 0.5° and thus only a small region of the hemispheric filter domes is examined. Even when allowing for seasonal variations in the solar declination, the total solid angle mapped out by the projection of receiver surface on the dome remains a small percentage of the hemisphere. For this reason, and unlike the total channels which are not filtered, the pitch-maneuver sensitivity estimates for the shortwave channel 13 serve only to establish bounds within which the effective sensitivity will fall.

An alternative approach to determination of the definitive calibration of the shortwave channel is based on comparison of channel 12 and 13 irradiances using the entire Earth as a target area. Irradiance data

for each radiometer are first zonally averaged and then integrated over the Earth sphere, separately for ascending node (AN) and descending node (DN) orbit halves. Day-night differences are then taken both to eliminate the seasonal and instrument-related nighttime bias from the shortwave channel measurements (cf. Figure 6b), and to remove the mean longwave flux component from the total channel irradiances. It is also necessary to eliminate the mean global day-night longwave flux differences from channel 12. This difference is estimated climatologically from the NFOV observations acquired during the first two data years. The correction amounts to approximately 5 W/m^2 at the top of the atmosphere. The ratio of the AN-DN differences of the shortwave estimates of the total channel 12 (after sensitivity corrections are applied) to the filtered channel 13 is illustrated in Figure 14 (triangles) where time increments along the abscissa are once again given in years beginning with November 1978. Any small errors in the channel 12 longwave calibration should have little effect here since a (AN-DN) difference from channel 12 is used. As expected, the ratio is near unity at the start of the experiment. The upward trend over time clearly states the cumulative sensitivity loss of the shortwave radiometer. The seasonal oscillation should not be interpreted as sensitivity fluctuations, but rather as bias shifts in the intra-orbital offset of channel 13 caused by seasonal changes in the thermal forcing.

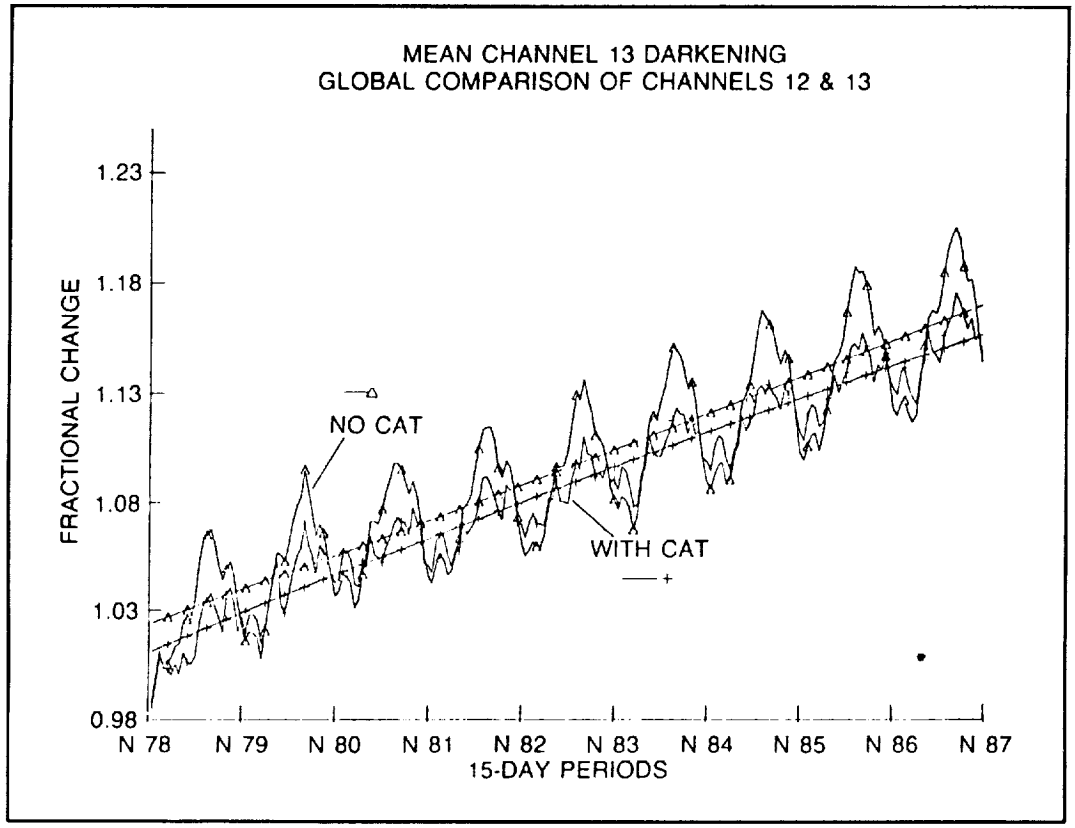

Figure 14. The mean relative darkening (inverse transmissivity) of channel 13, starting at turn on, versus time in years. The global mean "true shortwave" is taken to be the corrected channel 12 (AN minus DN) measurements. This value is divided by the mean channel 13 (AN minus DN) signal to determine the darkening. Channel 13 MAT level data were used uncorrected (triangles) and as corrected using the thermal CAT (pluses). Quadratic fits to both curves yield the final darkening estimates.

For degradation determination, this seasonal mode and any other biases to the estimates caused by the orbitally-varying sensor offsets are reduced by applying corrections obtained from the ERB shortwave channel thermal model (the thermal CAT model is discussed in Appendix B). The thermal CAT accounts for short-term variability in the WFOV sensor calibration based solely on temperature readings in and around the ERB instrument. These temperature measurements are provided with every MAT observation and make it possible to generate offset corrections smoothly and continuously throughout the data record. In the current application, an approximation of the thermal CAT is used which we refer to as the climatological thermal CAT. This model was developed prior to finalization of the global CAT algorithm and consists of global averages of the more detailed offset corrections generated by the thermal CAT. These global averages are given month-by-month throughout the first five years of the experiment, but they rely on only brief periods (i.e. several days) of data in each of the months. Beyond year five, the monthly estimates of year five are simply repeated. These climatological thermal CAT offsets contain the effects of the seasonal and interannual (first 5 years) cycles of solar and terrestrial thermal forcing, and internal instrument heating, on the sensor response. When applied to the half-monthly averages of Figure 14, the revised curve (pluses) is obtained. Notice the reduction in the amplitude of the seasonal oscillations that are obtained relative to the MAT data (triangles), even though the climatological thermal CAT offsets only approximate the half-monthly corrections required for these data. Based on seasonal and annual tabulations of this calibration data (i.e. the revised curve), channel 13 has apparently experienced a 15.3 percent loss of sensitivity during the first 9 years of the mission (Table C1).

Low-order (quadratic) polynomial curves, fitted to the two time series, are also plotted in Figure 14. The fitted curves show that: (1) the sensor degradation was more rapid earlier in the mission and (2) the thermal CAT by removing much of the sensor's offsets brings the sensitivity adjustments closer to unity in November 1978, validating the channel 13 pre-flight sensitivity determination.

Confirming evidence of sensitivity changes is found when an interannual time-series analysis of the shortwave channel's globally-averaged irradiances (Equation 6) is performed. In the cumulative degradation estimates (Figure 15), three scales of variability are noted. The highest frequency component (with periodicities on the order of 1 month—the Nyquist limit—to 2 months) is assumed to derive from normal synoptic and associated cloudiness variability. The multi-year mode, with minima in data years 3 (1980 to 1981) and 6 (1983 to 1984) and a maximum in data years 4 and 5 (1981-1983) is apparently a manifestation of the ENSO event, which exhibits an identical phase and period. Of immediate interest for instrument characterization is the longest-term, secular trend, which is fitted by a quadratic curve. This independent result clearly mirrors the degradation estimates obtained by the global comparison method (i.e., solar calibration of channel 12 transferred to channel 11 via the ratio of their AN-DN differences).

In practice, the shortwave-channel's sensitivity estimates used for production of the ERB parameters is obtained by fitting the transfer ratio (shown in Figure 14 with pluses) with a piecewise polynomial. Recognizing that the degradation occurred most rapidly near launch, a cubic polynomial is used for the first seven months of year 1. Further, in recognition of the nearly constant degradation rate of the sensor at present, a linear polynomial is applied after data year 5, with a rate of sensitivity loss of 1.4 percent/year. A quadratic polynomial is applied to the intermediate period. Note that the similar solar sensor, channel 2, actually showed an increase in transmissivity in 1988 as the solar activity increased in solar cycle 22 (Figure A5 in Kyle et al., 1993b). A smaller but similar increase in transmissivity also probably occurred in channel 13, but the WFOV data for this period has not been examined in detail. This cleansing is associated with high solar activity which results in strong increases in both atomic and singly ionized oxygen at the Nimbus-7 altitude (Predmore et al., 1982). An earlier cleaning of channel 13 occurred in the spring of 1979 (see Figure 8 in Ardanuy and Rea, 1984).

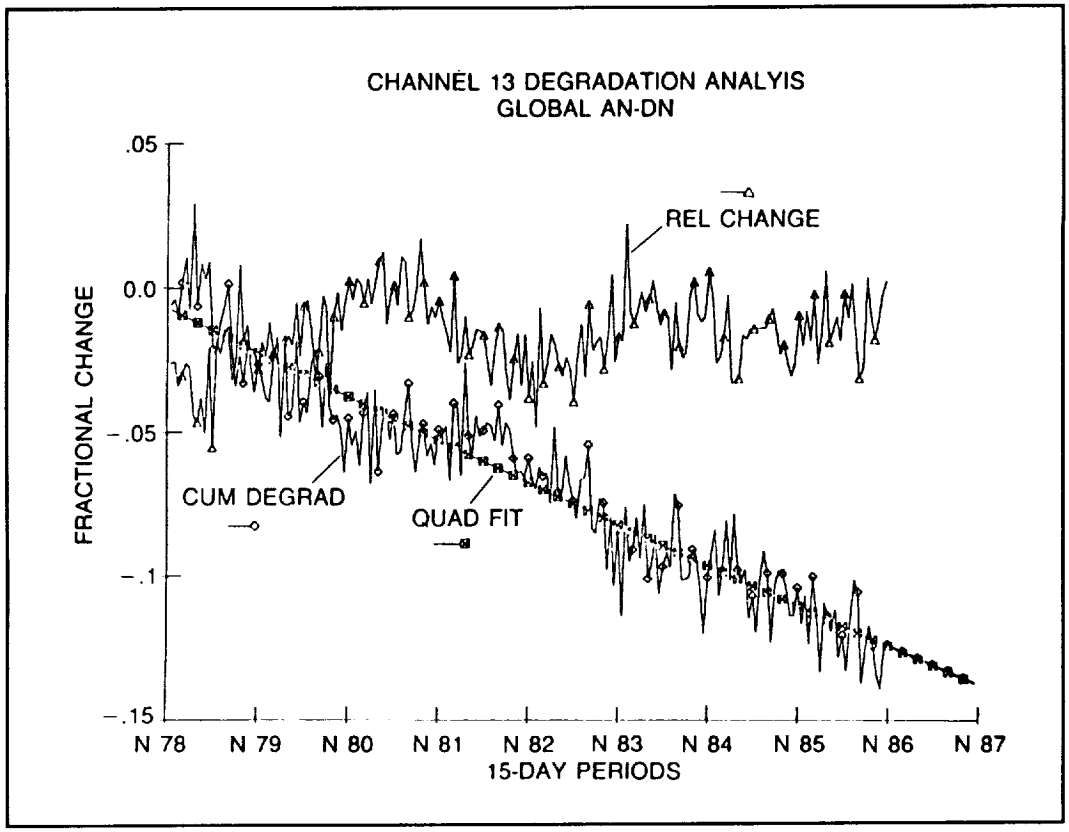

Figure 15. The channel 13 mean relative transmissivity changes are estimated from the long-term trend in the channel 13 mean MAT level (AN minus DN) measurements. the time series analysis referred to in Figure 12 and in the text is used. The mean long-term degradation is given by the quadratic fit to the cumulative degradation curve.

5.4 Sensitivity of the Near-Infrared Filtered Channel

Similar to the shortwave channel, the definitive calibration adjustment of the near infrared channel sensitivity is based upon a comparison with channel 12. Irradiance integrals are taken over the Earth, and day-night differences computed as in the procedure for channel 13. The residual diurnal component of longwave emission is likewise removed. However, the radiation estimate derived from the total channel's measurements is then reduced by slightly more than a factor of two to account for the reduced amount of the solar radiation available to a sensor in the near-infrared portion of the spectrum (see Appendix C.4). The precise value of this reduction factor is chosen to yield a sensitivity adjustment of unity at the start of data.

The resultant time series, plotted over the length of the dataset, is portrayed in Figure 16 (triangles). A comparison to the shortwave channel's analog in Figure 14 indicates clear similarities in the seasonal cycle, the cumulative degradation of the sensor, and the most rapid loss of sensitivity early in the mission. The orbitally- and seasonally-varying sensor biases are largely removed by applying, as with the shortwave radiometer, a set of corrections provided by the ERB near-infrared channel thermal model. The corrected curve is also presented in Figure 16 (pluses), as well as a pair of quadratic curves fitted to the respective time series. By the end of the first 9 years of the mission, the channel had apparently degraded 6.3 percent relative to its initial sensitivity, with a terminal rate of sensitivity loss of about 0.5 percent per year (see Table C1 in Appendix C). Time-series analysis of interannual globally-averaged,

near-infrared channel irradiances (Figure 17) confirms the estimates of both the rate and the cumulative degradation of this radiometer.

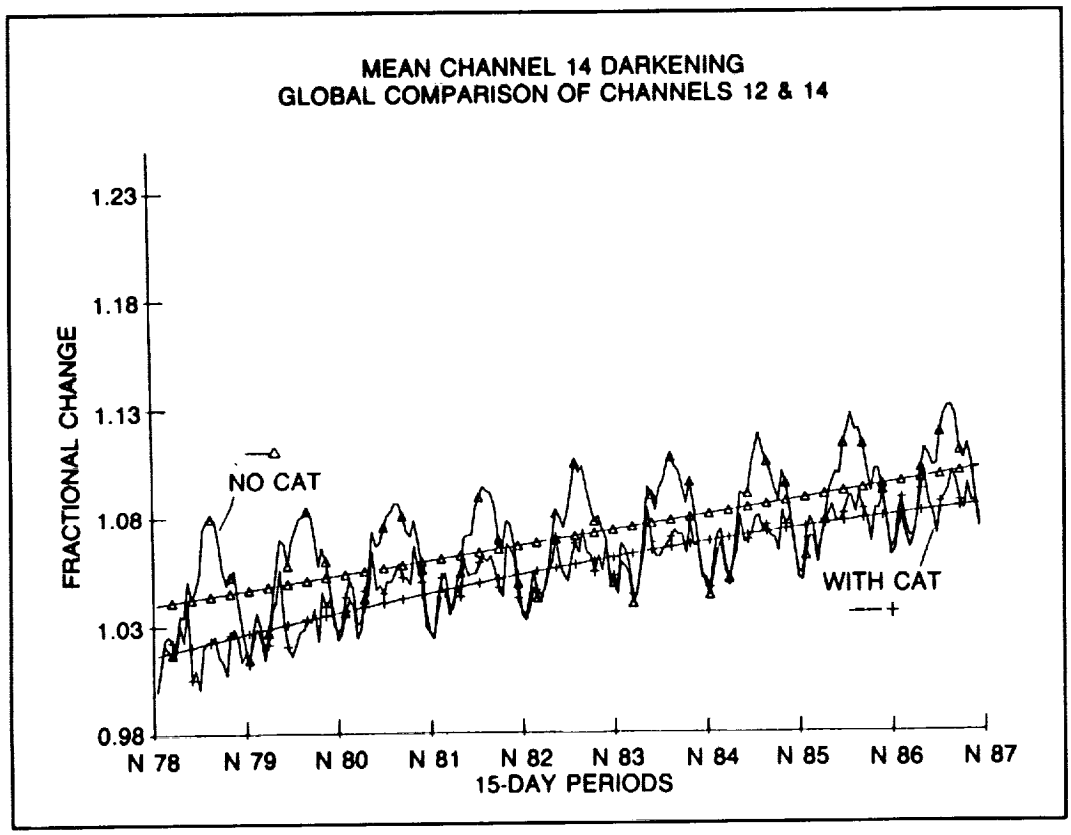

Figure 16. The mean, time-dependent darkening of channel 14 determined by comparison with channel 12 (see text and Figure 14).

5.5 Asymmetric Degradation of the Filtered Channels

Once the mean degradation of the shortwave channels has been accounted for, an asymmetry algorithm described by Kyle et al., (1984) is applied. Here we review the procedure for estimating the asymmetry in channel 13. This method is based on the comparison of channel 13 daylight measurements with concurrent NFOV scanner measurements (Ardanuy and Rea, 1984) during the time the scanner was active. The sheltered scanner shortwave filters apparently suffered no loss in transmissivity and are used as reference values. Three basic steps are required:

1. Monthly satellite altitude irradiance averages for a set of twelve 30° SZA bins are obtained. Of the 12 bins, 6 correspond to the satellite approaching and 6 to the satellite retreating from the Sun. Here the channel 13 irradiances are binned and averaged after removal of direct in-field and out-of-field solar response in the 90° to 120° SZA ranges (Section 6) and all other calibration offsets (Sections 7 and 8). Together these constitute the term b in Eq.(5).

2. The satellite altitude irradiance averages are inverted to the "top of the atmosphere" (TOA) to realistically enhance the scene variability. Here the weighting function (King and Curran, 1980; Ardanuy and Jacobowitz, 1984), which relates the satellite altitude and the TOA irradiances, is

cast into a diagonally symmetric 12 by 12 weight matrix. This is accomplished by integrating over 1/12 of an orbit, or 30° of Earth central angle for each matrix element. A 30° satellite altitude band is affected by the nearest three TOA bands by the normalized weights of (0.087, 0.826, 0.087). This matrix is inverted to yield the inverse relationship, where a 30° TOA band is affected by the nearest satellite altitude bands through the inverse weights of (-0.001, 0.014, -0.132, 1.238, -0.132, 0.014, -0.001). With the direct effects of solar radiation removed, only terrestrial-reflected solar radiation is left for the inversion. The inverted matrix is applied to obtain the 12 TOA irradiance bin averages. Here the anisotropy of reflected solar radiation is neglected. However, the dependence of solar flux on SZA is present implicitly in the binned averages of the irradiances.

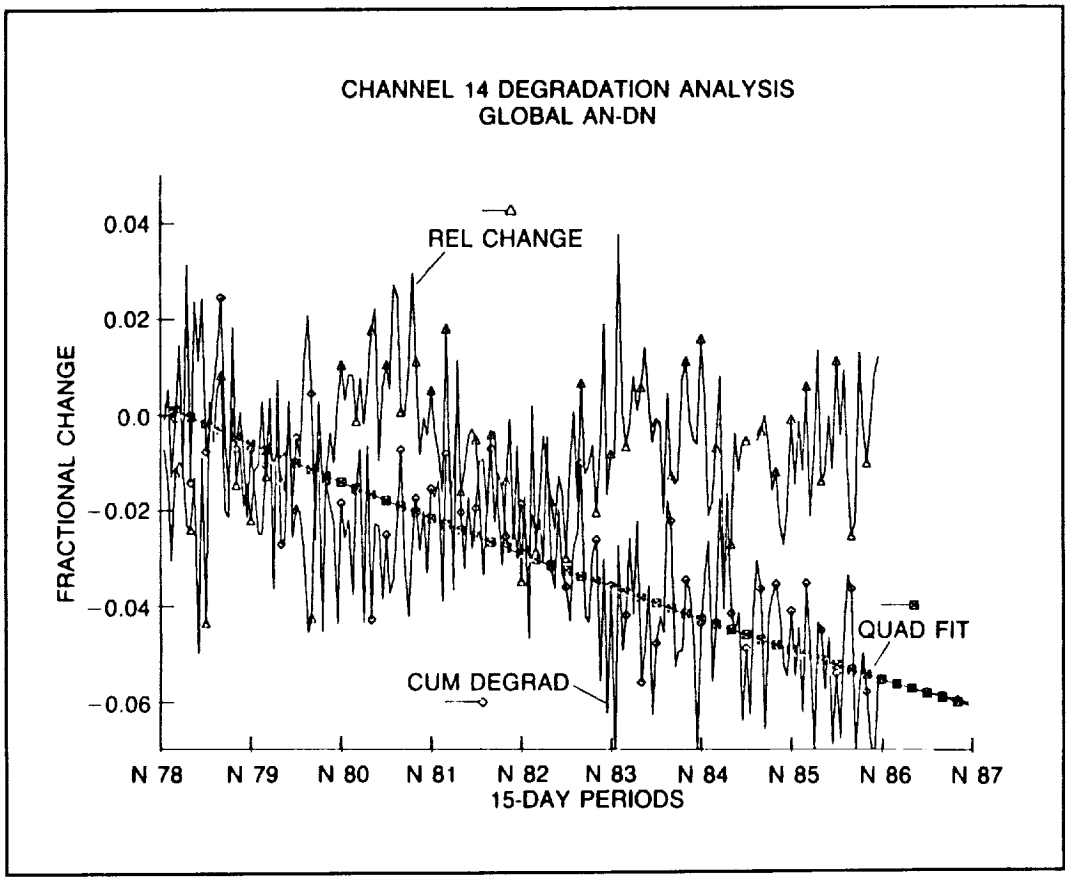

Figure 17. The channel 14 mean relative transmissivity trend is estimated by the time series analysis referred to in the text and in Figure 12. The actual long-term trend is given by the quadratic fit to the cumulative degradation curve.

3. Asymmetric degradation corrections are computed as a function of orbital position based on evaluation of the effective transmissivity, T_e, given by

$$T_e = T_s \{1 - \frac{\Delta}{R}(\alpha - \frac{1}{2})\} \quad (7)$$

where T_s is the mean degradation of the hemispherical dome and is independent of satellite position, Δ is irradiance difference between adjacent bins, R is irradiance average between adjacent bins, and α is the dome degradation asymmetry factor. Alpha represents the fractional degradation of the backside (away from the direction of the satellite velocity vector) of the filter dome relative to the dome mean degradation. Its is fixed after February 1979 at 0.51, the value to which the instrument converged prior to the failure of the scanner (Ardanuy and Rea, 1984). From launch through February 1979, α is interpolated between the value of 0.50 for a symmetric dome and its terminal value of 0.51. The coarse 30° spatial resolution of the correction procedure eliminates most high frequency variability in T_e due to orbital fluctuations in the TOA radiance. Interannual variability in T_e is also removed by replacing actual values of R and Δ, during evaluation of the term in braces, by their monthly climatological means values. These climatological means are based on scanner data.

An example of how the scheme works is shown in Table 7. The 12 SZA bins are shown on the left, but only one is associated with a given observation and it is determined based on the location of the subsatellite point. The three central columns represent steps in the inversion of the band-averaged irradiances to the top of the atmosphere as discussed in Step 2 above. The two right-hand columns give the transmittances T_s and T_e for each band. The value of T_s shown was picked for heuristic purposes and is only a guide estimate of T_s on November 19, 1979. For actual data processing, the T_e of Eq.(7), not T_s, are used to correct the channel 13 irradiances obtained from the MATs. No asymmetric correction is applied to channel 14. The evidence indicates the transmissivity loss was greater in the ultraviolet visible portion of the spectrum than in the near infrared (Kyle et al., 1993b). In addition, the northern hemisphere is brighter in the near infrared than is the southern hemisphere (Kyle, et al., 1986). Thus, a good asymmetric algorithm has not been developed for the smaller problem on channel 14. Even on channel 13 we assume the asymmetry to be constant from March 1979 onward. This algorithm is thus unchanged from the Pacific CAT.

6. REMOVAL OF SOLAR TARGET IRRADIANCE

All of the ERB WFOV receivers are in direct sunlight between SZAs of 113° and 120° and, except for the black-painted channel 11, they continue to be illuminated by indirect solar radiation from 90° to 113° (cf. Figures 3 and 4 and Section 3.1.1). It is desirable to attempt to remove the effects of solar contamination across the entire 90° to 120° SZA range for two reasons. First, "recovering" the Earth signal from this data would substantially enhance the coverage of the ERB WFOV dataset since nearly one-sixth of an orbit is affected. Second, since continuous orbit corrections for LW dome heating in channels 13 and 14 rely on terrestrial emissions minutes prior, an uninterrupted set of WFOV observations is required.

Interpolation across the entire zone of solar contamination is one method of removing the solar signal from WFOV data. We tested the accuracy of such an approach by generating simulated WFOV observations from NFOV data which contain no solar contamination and may be used as a reference field. Using a cosine of nadir angle weighting function, simulated WFOV irradiances were obtained by integrating NFOV data over the footprint size of the WFOV. Given the approximately 7° Earth central angle half-power radius of WFOV observations, however, insufficient information exists to bridge the interval from 90° to 121° of SZA with reasonable accuracy. It was thus decided to interpolate across no more than three half-power radius widths, i.e., from 99° to 121° of SZA. In tests with simulated longwave irradiance data, this interpolation width produced a midpoint bias of less than 1 W/m^2 and a standard deviation of the error of 4 to 6 W/m^2, reduced from biases of up to 5 W/m^2 and

standard deviations of 7 to 8 W/m^2 for the entire interval 90° to 121° SZA range as shown in Table 8. A different technique to estimate the stray-light signal from 90° to 99° of SZA is discussed below.

Table 7. Example of Degradation Correction for Asymmetric Effects (November 19, 1979) CH 13.

	Irradiance (W/m^2)			Transmissivity (%)	
Solar Zenith Angle Range (°)	After Application of Calibration Offsets	After Correction for "Out of Field" Response	TOA	Symmetric Transmissivity T_s Prior to Correction for Asymmetries	Effective Transmissivity T_e After Correction for Asymmetries
Satellite Leaving Sun					
150 to 180	-0.3	0.0	0	NA	NA
120 to 150	-0.4	0.0	0	NA	NA
90 to 120	87.0	12.0	0	97	99
60 to 90	112.1	112.1	119	97	97
30 to 60	167.4.	167.4	168	97	97
0 to 30	203.3	203.3	208	97	97
Satellite Approaching Sun					
30 to 0	217.5	217.5	204	97	97
60 to 30	307.3	307.3	336	97	98
90 to 60	178.5	178.5	183	97	96
120 to 90	89.1	18.2	0	97	95
150 to 120	0.5	0.0	0	NA	NA
180 to 150	-1.1	0.0	0	NA	NA
Midnight					

$T_e = T_s \{1 - (\Delta/R)(\alpha - 1/2)\}$, where Δ is the irradiance difference between adjacent bins, R is the irradiance average between adjacent bins, and α is the degradation asymmetry ~0.51.

Table 8. Estimates of bias introduced by interpolation across sunblip.

Month	Interpolation Interval	Midpoint Bias (W/m^2)	Midpoint Standard Deviation (W/m^2)
December	90° to 121°	0.3	8.0
December	99° to 121°	0.9	4.0
June	90° to 121°	5.5	7.7
June	99° to 121°	0.4	6.4

6.1 Elimination of Stray Light

Interpolation across the sunblip interval is accomplished by using a tensioned cubic spline (for instance, see Cline, 1974) with the tension factor determining how "tight" or "slack" a fit is produced. Two sets of four "knots", or anchor points, are spaced every 12 major frames (one major frame is 16 seconds) on either side of the data gap and including the endpoints at 99° and 121° of SZA; thus, knots are taken at the following SZA's: 90.6°, 93.3°, 96.1° and 98.9° on the daylight side of the sunblip; 121.2°, 123.9°, 126.7°, and 129.5° on the nighttime side. The interpolated values are channel 13 irradiance, channel 14 irradiance, and longwave irradiance, the latter first computed as the difference between the channel 12 and channel 13 irradiances. Since knots on the daylight side of the sunblip interpolation interval are contaminated by stray light, they are, in general, also biased. An estimate of this bias was made by comparing observed channel 13, 14, and computed longwave irradiances at a SZA of 99° with estimates of these values obtained from an interpolation across the interval 90° to 121° SZA. If we assume the latter value is the "truth", the difference between this value and the observed value at 99° SZA is the bias introduced by solar contamination. This bias was analyzed for six 3-day samples and found to be consistent throughout the year. A similar analysis of the other three sunblip knots produced progressively lower biases, but again consistency throughout the year. The average results are shown in Table 9. The values vary between sunrise and sunset because of the different angle at which sunlight strikes the instrument.

Table 9. Biases due to solar contamination of WFOV sensors in solar zenith angle range 90° to 99°.

Solar Zenith angle of knot	Channel 13 Bias		Channel 14 Bias		Longwave Bias	
	Sunrise	Sunset	Sunrise	Sunset	Sunrise	Sunset
98.9°	3.4	3.0	1.8	2.2	4.9	2.3
96.1°	2.3	2.0	1.2	1.5	3.3	1.6
93.3°	1.1	1.0	0.6	0.7	1.6	0.8
90.6°	0.0	0.0	0.0	0.0	0.0	0.0

In Figure 18, channel 12 minus channel 11 irradiance differences (normalized by the value of channel 12) are shown for 20 August 1984 (orbit number 29405) in the SZA range from 90° to 110°. In this SZA interval, no direct sunlight strikes the receiver and both radiometers register the flux of terrestrial radiation at satellite altitude. In addition, channel 12, but not 11, records a solar stray light signal, evident in the figure by the increasing irradiance difference with SZA. At 99° of SZA, satellite observations are taken on descending node at a latitude of about 80°S (the solar declination is near 10°N in August). Estimates of the stray light flux on the channel 12 detector are obtained by reading irradiance differences off the curve (about 6.7 percent), subtracting the mean orbital irradiance difference (i.e., differences at SZA<90°, about 1.5 percent), and multiply by channel 12 signal strengths (about 100 W/m^2 at the TOA), due almost entirely to emitted terrestrial radiation. These values yield a stray light signal of about 5.2 W/m^2. This value is very comparable to the bias given in Table 9 for LW radiation at the same SZA, thus supporting the procedures used in computing the fixed biases.

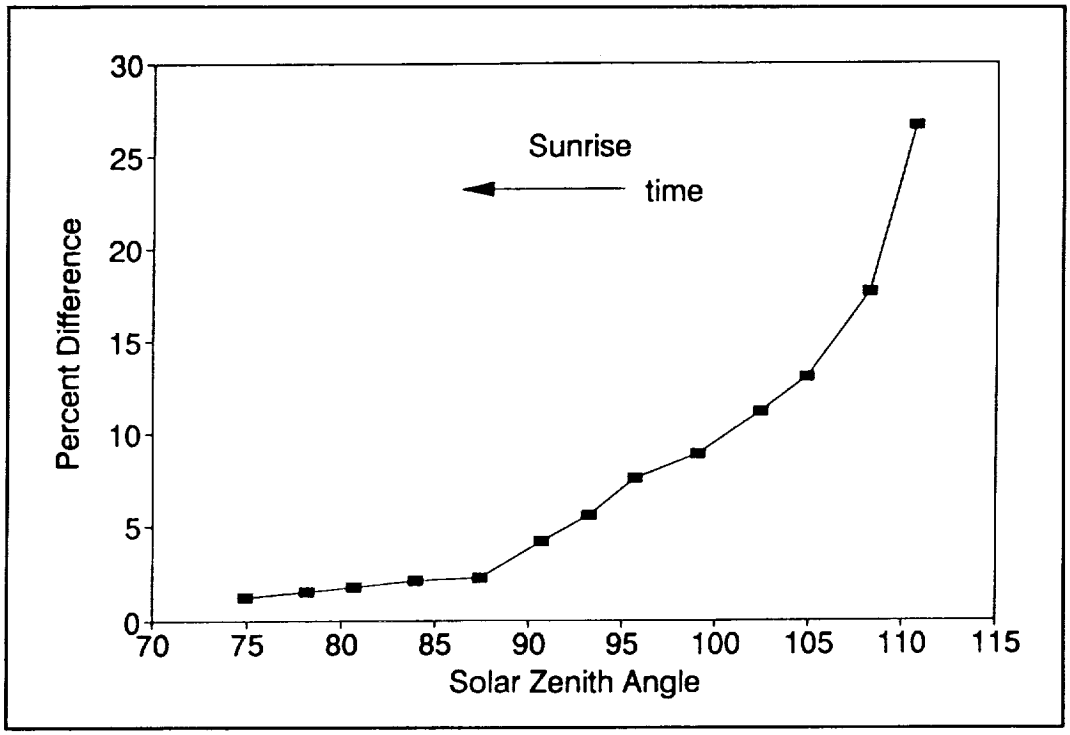

Figure 18. The channel 12 minus channel 11 difference (normalized by the value of channel 12) is shown for a portion of the orbit where direct sunlight starts to strike the baffles but not the sensor chips. The data come from orbit number 29,405 which occurred on August 20, 1984. The baffle on channel 11 is black and that on channel 12 is shiny. In this region, the direct solar signal increases with the subsatellite solar zenith angle and so does the difference in the two signals.

6.2 Interpolation Across Sunblip

During implementation, stray light contamination in the 90° to 99° SZA range is removed first by application of the fixed bias corrections to the interpolation knots on the daylight side of the sunblip. Then, interpolation across the sunblip and between the four daytime knots is performed using a moderate tension factor of 0.6 based on the simulated WFOV/NFOV interpolation studies. The total correction extends from 90° to 121° of SZA and all observations within this interval are replaced by interpolated values. Channel 12 total irradiances within the interpolation interval are reconstructed as the sum of the modified longwave and channel 13 shortwave irradiances.

7. THERMAL ADJUSTMENTS OF CHANNELS 13 AND 14

The accuracy of the prelaunch WFOV calibration equations in a changing thermal environment is greatest for the total channels 11 and 12 and least for the filtered channels 13 and 14. The basic difference is that the filter domes covering channels 13 and 14 apparently induce unanticipated bias fluctuations. These arise from the nonsteady state satellite environment and were not noticed in the preflight calibration program. As shown in Appendix B, these bias fluctuations can be modeled as a function of various sensor and instrument temperatures. The domes may magnify the amplitude and/or the importance of temperature difference fluctuations across the thermopiles of channels 13 and 14 relative to channels 11 and 12. In addition, channels 13 and 14 receive a background longwave bias signal from the inner dome.

It is reasonable to assume that the temperature of this dome may vary around the orbit in a manner similar to the sensor temperature (cf. Figure 22). A third point is that while the domes modify the path by which longwave radiation is emitted to space, relative to channels 11 and 12, they do not stop this emittance.

Note that the MAT calibration, Eq.(3), for channels 13 and 14 contains no temperature dependence for the offset voltage V_o. That this is a serious drawback in the calibration of the filtered channels is demonstrated in Figure 19 which shows a time series of channel 13 irradiances for descending node equator crossings over the 3-day period November 27-29, 1979. Because it is nighttime, there is no shortwave signal in these data and yet instrument readings are not zero. In fact, they are not even constant, varying by some 12 W/m^2 over the interval. Moreover, these variations are highly correlated to instrument temperatures as may be seen by comparing the two curves in the figure; the second is a plot of the channel 2 thermopile base temperature that is considered typical of the thermopile base temperatures of all the channels. During the first few orbits (there are ~13.9 per day), the thermopile base temperature rises from about 14°C to approximately 21°C. This is associated with the warming of the ERB instrument by its own electronics and motor. Turning the ERB scanner and other experiments such as the SMMR on and off during the rest of the period perturb the thermopile temperatures. The increase on November on 28 is most probably due to the SMMR being "on" on November 28 but "off" on November 27 and 29. Thus, it is evident that both the ERB and SMMR instrument duty cycles have a strong effect on the channel 13 offset voltage.

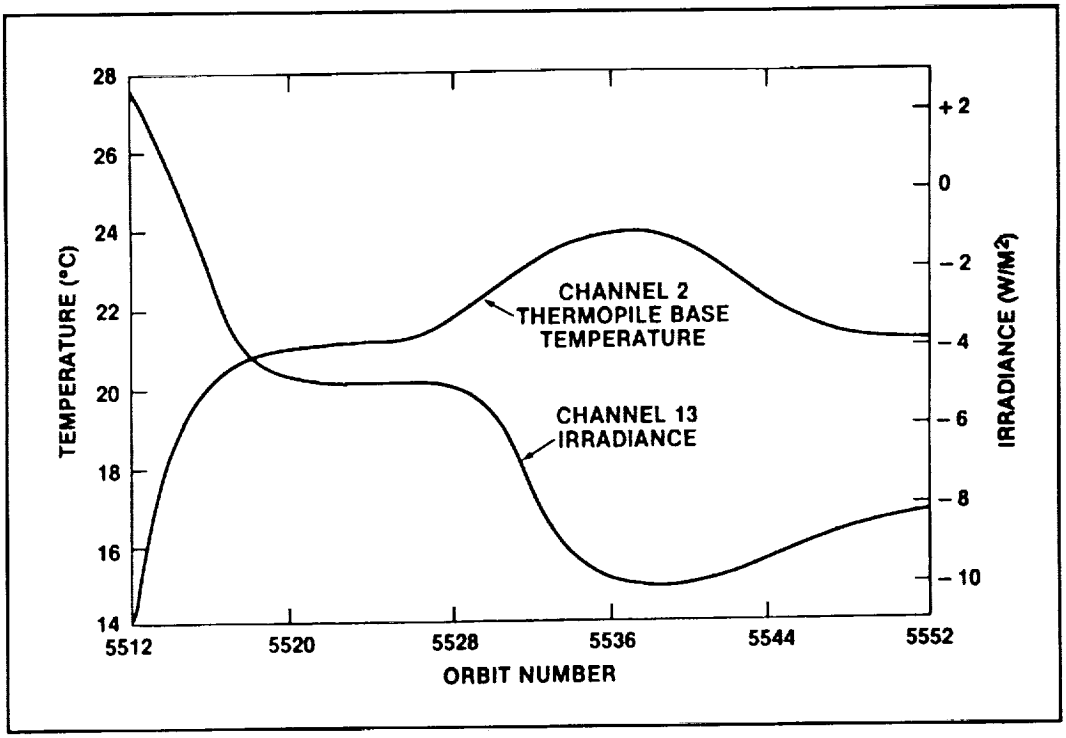

Figure 19. Plot of channel 13 signals at the descending node (night equator crossing) and of associated channel 2 thermopile base temperatures throughout a typical 3-day ERB on period. The horizontal scale gives the satellite orbit number with 13.85 orbits per day. At this time in the orbit the signal should, ideally, be zero; note how it varies inversely with the temperature. The nonzero signals are caused by thermal gradients in the sensor module. The same characteristics are shown by all of the thermopile base temperatures. The curves vary seasonally and from year to year (figure from Kyle et al., 1984).

Within an orbit, there is additional forcing associated with the passage of the satellite through a varying external environment. In the global CAT, we recognize three orbit segments, each having a different configuration of solar and terrestrial radiation incident upon the instrument.

- Satellite night with only terrestrial thermal radiation incident on the sensors and casings.
- Satellite sunrise and sunset with direct sunlight warming the front and back of the instrument, respectively, and to a lesser extent its Earth-viewing side.
- Satellite day with both terrestrial reflected sunlight and thermal radiation incident on the sensors, but no direct solar radiation.

During the application of thermal adjustments, we consider sources of thermal forcing separately for each of the three orbit regions. The effects of instrument duty cycles, while not considered individually, are accounted for in this strategy by quasi-continuous corrections throughout each orbit.

7.1 Satellite Night

Irradiance offsets at night as well as during the day reflect the thermal condition of the instrument and individual detectors. At a given moment, heating sources inside (instrument workload) and outside (upwelling terrestrial radiation) the instrument, and prior history determine this thermal state. Although not easily computed, their effect on the offsets is approximately known based on instrument readings at night. Analyses show that these readings vary with season, from orbit to orbit, and over an orbit cycle. The midnight offset correction, so named because it is based on channel readings taken once per orbit at satellite midnight, accounts for the orbit-to-orbit (chiefly instrument duty cycle effects) and seasonal component of this variation. These irradiance observations provide direct measurements of the calibration offset b in Eq.(5) since the measurements should be zero at this orbital phase. Continuous estimates of the midnight bias component are generated by interpolating the channel readings from midnight to midnight over an orbit period. This extends the midnight offset correction to the daytime domain. Additional thermal perturbations are due to variable solar and terrestrial heating within an orbit cycle. These are largely removed by the shortwave heating (Section 7.2) and daytime offset (Section 7.3) corrections that are also applied.

7.2 Satellite Sunrise and Sunset

Clipping the sunblip (that portion of the orbit between SZAs of 90° and 121°) removes the direct and stray light components of solar irradiance from the WFOV measurements. However, even after the sensors are no longer illuminated by sunlight, solar heating of the instrument and casings continues as long as these components remain exposed to direct sunlight. Of course, instrument cooling also takes place and both terms govern the level of internal temperature gradients and the changes in offset irradiance that actually occur. As an approximate correction scheme, we consider an impulse model in which incremental gains of absorbed solar radiation in the SZA range from 90° to 120° produce independent heating signals in channels 13 and 14. Net response is cumulative, but the separate exponential decay of each signal amplitude leads to eventual dissipation of the entire solar heating perturbation. Residual thermal fluctuations within an orbit are assumed to be adequately accounted for by the day (Section 7.3) and midnight (Section 7.1) offset corrections that are also applied.

7.2.1 Solar Heating

The instrument is directly heated by the Sun for subsatellite SZAs between 90 and 120°. The intensity profile of this heating is similar to the cosine variation of the solar irradiance during sunblip spikes (Figure 3), but it is modified by the reflectance of ERB channel surfaces and instrument casing. The solid line in Figure 20 shows laboratory measurements of this heating in a simulated inflight environment. The curve is normalized by the value at SZA = 120° where the maximum heating occurs. The important effects take place between SZAs of 100° and 120° with maximum heating at 120°. Beyond 120°, the satellite is in the Earth's shadow and no shortwave heating can occur. For angles less than 90°, the satellite shields the sensors and again no direct solar heating is possible. Daytime heating by terrestrial reflected radiation (SZA < 90°) is considered separately in section 7.3. Due to uncertainties in the laboratory data (reflectance and angular geometry) the shape of the solid curve in Figure 20 is only approximate. Thus, the triangular heating function represented by the solid line between 120° and 100° and its extension to 98° (dashed) is adopted for the global CAT. The maximum heating strength at an incident angle of 60° (SZA = 120°) is different for each of the channels and varies according to whether it is sunrise or sunset. Thus, we define a channel and orbitally dependent amplitude factor, A, which when applied to the solar constant and modulated by the Earth-Sun distance, yields the maximum instantaneous solar heating contamination. In terms of A and the triangular response function, F (normalized to unit amplitude), the sensor solar heating response is expressed as

$$H_{heating} = A \cdot I_{sun} \cdot F \tag{8}$$

where I_{sun} is the solar constant adjusted for Earth-Sun distance, and F is non-zero only over incident angles from 60° to 82°.

The channel amplitudes (A) required for evaluation of Eq.(8) as a function of SZA were determined by analyses of empirical data for the solstice months of December 1982 and June 1983. A value of 0.002050 zeroed the channel 13 sunset irradiance at 135° of SZA in both months with all other calibration corrections applied. A similar result was obtained for channel 14 using an amplitude of 0.001100. At sunrise, both channel amplitudes are reduced by a unique factor which varies sinusoidally between extreme values of 0.56 in December to 0.43 in June. This seasonal component in the sunrise amplitudes was inferred by analyses of the same empirical data, namely the months of December 1982 and June 1983.

7.2.2 Thermal Cooling

The sensor response generated by each increment of absorbed solar radiation decays according to the exponential model

$$H_{cooling} \propto \exp(-\frac{t}{T}) \tag{9}$$

where t is time and T is the time decay length. The time delay constant in Eq.(9) was estimated by laboratory tests to be 20 major frames (320 seconds) for Channel 13 and 30 major frames (480 seconds) for Channel 14. Note that according to the impulse model of heating and decay that we have adopted, increments of shortwave heating dissipate independently. Thus, at sunset where the greatest solar heating

impulse is also the last, the channel response persists for a longer period (after cutoff of direct solar heating) than at sunrise.

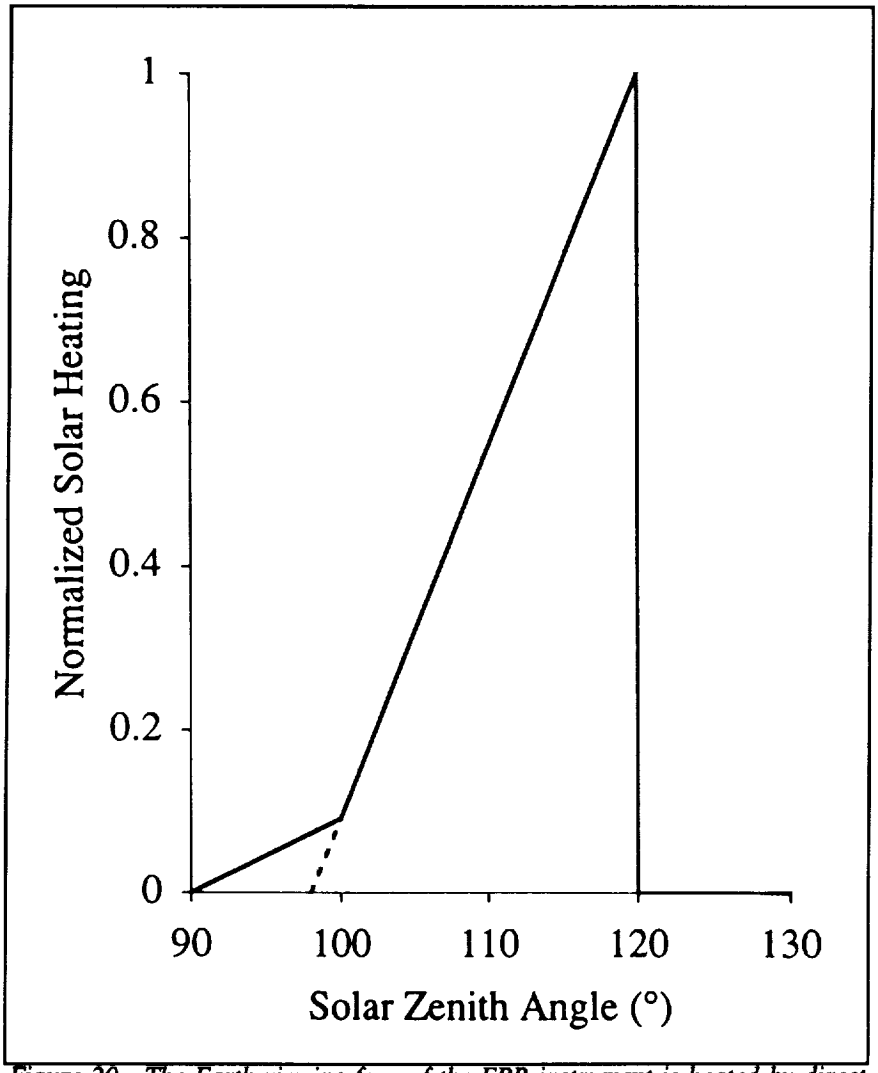

Figure 20. The Earth-viewing face of the ERB instrument is heated by direct sunlight only at satellite sunrise and sunset. At sunset, direct sunlight starts to strike this face as the solar zenith angle (SZA) increases past 90°. At an angle of 120°, the satellite enters the Earth's shadow thus terminating the direct solar heating. A reverse path is followed at satellite sunrise. The direct solar heating function is approximately triangular as shown normalized to unit amplitude.

7.2.3 Convolution

The elements of forcing and decay are combined to produce the resultant instantaneous shortwave heating estimate. Since they are cumulative, the net heating at a time t is given by

$$H_{\text{net heating}}(t) = A \cdot I_{\text{sun}} \cdot \int_{o}^{t} F(t') \cdot \exp\left[-\frac{t-t'}{T}\right] \cdot dt' \qquad (10)$$

where the variable of integration, t', may be referenced to zero at the time of launch. Figure 21 shows the magnitude of the shortwave heating response on 29 July 1992 as a function of SZA for one orbit cycle (orbit number 69498). Notice that at sunrise, the peak channel response, ≈ 8 W/m^2, occurs at about 105° of SZA, before the satellite exits the domain of direct solar heating. At sunset, the maximum heating perturbation is larger than at sunrise, $\approx$ 23 W/m^2, and it is cutoff as the satellite enters the Earth's shadow. The shortwave heating correction, as implemented during calibration adjustment, is simply the negative of the channel response developed here.

7.3 Satellite Day

The shortwave heating correction of Section 7.2.3 accounts for the intensive heating of the ERB instrument and detectors under direct solar illumination near satellite sunrise and sunset. Additional more subtle shortwave heating and instrument cooling occur along the length of the orbital path due to variable terrestrial and solar shortwave heating of the ERB instrument and Nimbus observatory. Temperature monitors (TMs) near channel 13 show an orbital fluctuation of the temperatures of about 1.5°C from satellite night to satellite day. This is illustrated in Figure 22a where the temperatures from sensors in and near channel 13 are plotted for a typical orbit. Note in Figure 22a that the inside of the assembly block is always warmer than the outside. Thus, the warm instrument box is always losing heat to space by radiative cooling. Most of this heat comes from the electronic components and motors on the satellite. The external warming by radiation from the Sun and the Earth merely modifies the rate of net energy loss. This modification can have important effects on channel 13 as we have shown in Section 7.2. The temperature changes at sunrise and sunset are relatively small despite the rather large bias changes. Thus, curiously, the TMs close to channel 13 do not seem well correlated with the strongest observed sensor bias changes.

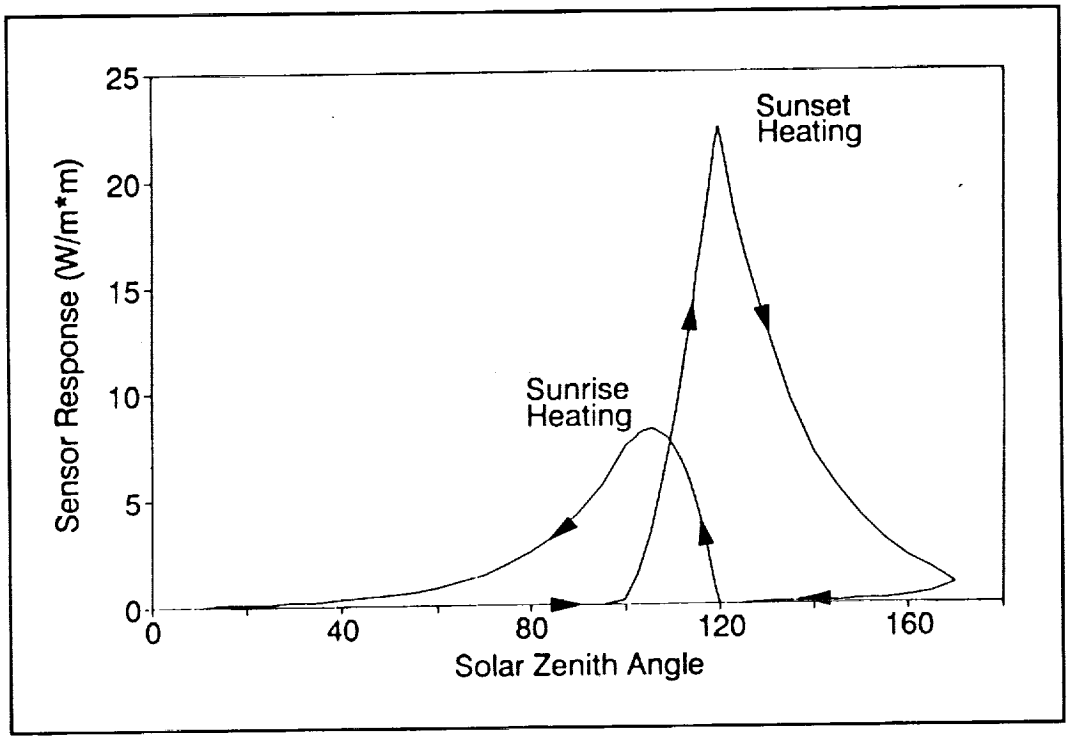

Figure 21. Calculated changes in the channel 13 signal due solely to direct solar heating at satellite sunrise and sunset. This particular graph was based on data from orbit no. 69,498 which occurred on July 29, 1992.

However, a few surface TMs do show dramatic intraorbit variations. Figure 22b shows the temperature curve for the TM at the channel 12 FOV stop for an orbit near the June 1988 solstice. Here temperature is plotted against latitude to allow comparison with the calculated bias corrections shown in Figures 23b and 24b. The numbers on the curve show the solar zenith angle (SZA) at that position. Note the over 12°C temperature rise at both satellite sunrise (near South Pole) and sunset. Recall that the satellite exits (enters) the Earth's shadow at SZA = 120°. This TM cools about 20°C from satellite sunset to sunrise. After the sunrise heating, cooling occurs in the morning followed by gentle heating in the afternoon. Figure 22b should be inverted for best comparison with Figures 23b and 24b since a temperature increase corresponds to a decrease in the bias correction. We are not certain just what physical mechanism causes the strong correlation between some fairly remote surface TMs and the channel 13 bias. We hypothesize that the channel 13 window domes may be at least partially involved. The outer dome may have a temperature curve related to that in Figure 22b, with the inner dome showing a subdued copy. Insulation was used to reduce conduction between the domes and the sensor case, but the outer dome could be heated both by direct shortwave radiation and by longwave radiation from heated instrument surfaces. While the domes were originally highly transparent to shortwave radiation, at least the outer dome has suffered considerable darkening over time (Figures 5c and 14). In this theory, alternate radiant heating and cooling of the outer and inner domes would cause a modulated temperature imbalance between the sensor chip and the inner dome. This might produce most of the intraorbit biases observed in both channels 13 and 14. A modulation due to variations in the incident terrestrial longwave signal has been definitely identified (Sections 3.1.5 and 8). Direct and indirect heating due to shortwave radiation and longwave cooling to cold space probably create even larger modulations. This remains a conjecture since our studies have concentrated on developing empirical bias corrections and not on exact modeling of the physical behavior of the sensor package.

The global CAT daytime thermal correction is determined as a half monthly global mean value. It is a bias remainder after the other four short-term bias corrections have been made on an orbit-by-orbit basis. These first four are: sunblip clipping, midnight bias, SW sunrise and sunset, and LW heating as described, respectively, in Sections 6, 7.1, 7.2, and 8. Figure 10c shows that, except for a daytime bias, all global CAT calibration offsets (i.e. the components of b in Equation 5) are applied in deriving DELMAT data. Differences of these DELMAT data (corrected for sensor degradation) with actual satellite altitude irradiances are used, therefore, to specify the effects of daytime shortwave heating and any other offsets that may be present in daytime data.

The computation of the daytime correction starts with an estimate of the "true" mean global SW radiation

$$SW_T = Ch12(AN) - Ch12(DN) - \delta(LW) \qquad (11)$$

This true value is then compared with a similar expression for the channel 13 measurements. The components of Eq.(11) are half-monthly, global average irradiances for ascending and descending nodes. Calibration corrections are applied to the channel 12 data (See Appendix C), and the ascending-descending node LW irradiance difference (δ(LW), determined from scanner data) is also removed. The channel 13 comparison values are corrected for the other short-term perturbations. The details of the calculation are given in Figure 10d and Appendix C.

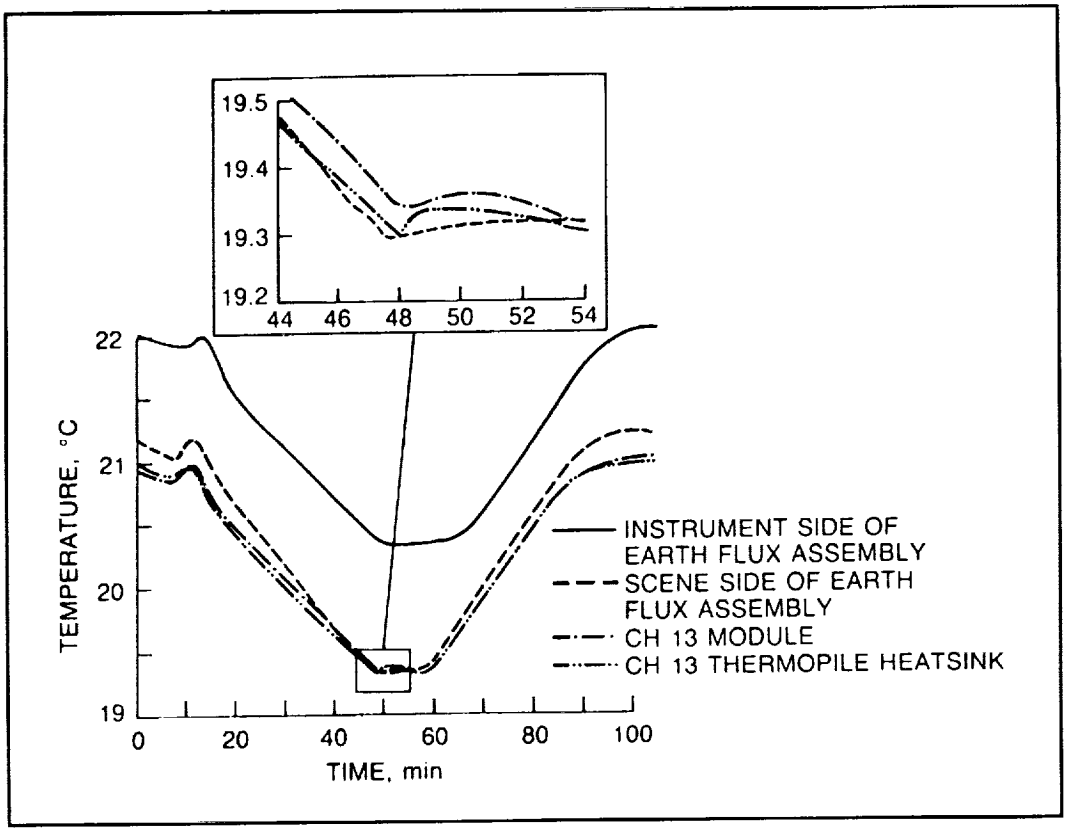

Figure 22a. Typical orbital temperature signatures for temperature monitors (TMs) in and near the channel 13 sensor module. Cooling during the satellite night and heating during the satellite day account for the major temperature variations. Note that the inside of the instrument box is about 1°C warmer than the outside. Only small temperature perturbations occur at satellite sunset (hump at far left) and sunrise (at center and insert). This figure is taken from Maschhoff et al. (1984).

7.4 Validation Using Thermal Models

Figures 14 and 16 illustrate time series of the ratio of channel 13 and 14 irradiances to those of the stable channel 12, respectively, based on half-monthly averages of the data. The curves with pluses were produced by first removing the continuous bias corrections generated by the climatological thermal CAT; the thermal CAT is described in Appendix B. As can be seen, most short-term variability in the uncorrected irradiance ratios (triangles) is removed by the thermal CAT. Thus, for averaged data, the thermal CAT generates a much improved WFOV irradiance data set. It is not used for definitive calibration bias adjustments, however, because being based on regression results, it is dependent on the instrument operating schedule which has been variable over the lifetime of the experiment. Nevertheless, we used the average results of the thermal CAT as a means of validating the global CAT.

The thermal and global CATs are in qualitative agreement, but they do exhibit some significant ascending node differences. The global CAT uses half-monthly averages to compute the daytime offset correction (to the midnight) offset while the thermal CAT calculates the offset for each measurement. Typical solstice and equinox thermal CAT channel 13 orbital bias offsets are shown in Figure 23. Global CAT offsets for the same period are shown in Figure 24. The global CAT orbital offsets are characterized by nearly constant (flat) ascending-node and descending-node offsets connected by the sunrise (near South Pole) and sunset (near North Pole) shortwave heating perturbations. The thermal CAT offset varies

continuously throughout the orbit. The best agreement between the two orbital offset models occurs at the winter solstice. While the actual AN and DN offsets are not constant, the thermal CAT estimates of these offsets may be no more accurate than those of the global CAT.

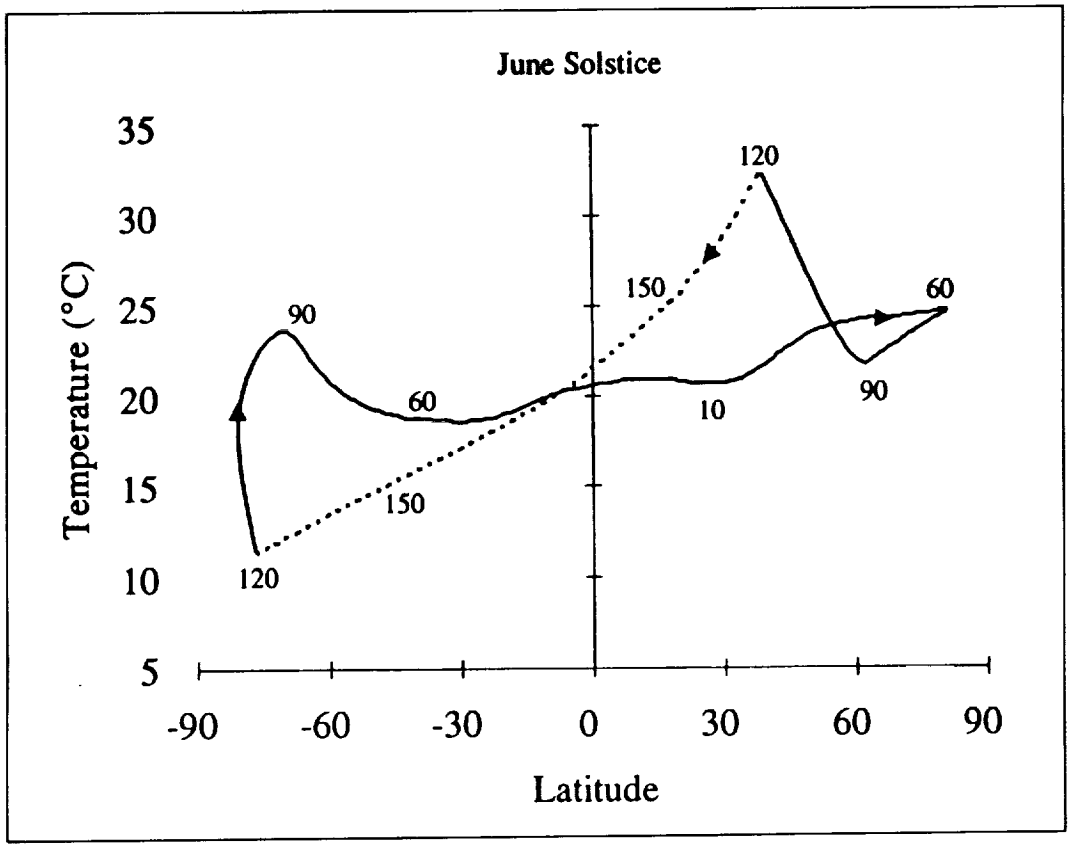

Figure 22b. Temperature variations at the channel 12 field-of-view stop during orbit near the 1988 summer solstice. The temperature is plotted against latitude to allow comparison with Figures 23 and 24. The numbers on the curve indicate the solar zenith angle at these orbit positions. This is one of the temperatures used in the thermal CAT (see Appendix C).

To examine this question, a study was performed using the independent ERB scanner data as a "truth field." Six days in June 1979 and six days in December 1979 were chosen and both global and thermal CAT calibrations were applied to the WFOV MAT data. Degradation of the WFOV channels 12 and 13, in addition to offset corrections, were also taken into account. Comparison was then made between the fine resolution NFOV data and the coarse resolution WFOV global and thermal CAT longwave fluxes. During daylight the WFOV longwave irradiance is given by

$$I_{LW} = I\ (\text{Ch}\,12) - I\ (\text{Ch}\,13) \qquad (12)$$

Thus both channels 12 and 13 are involved in the OLR measurements. The corresponding NFOV longwave AN fluxes were averaged over each six-day period.

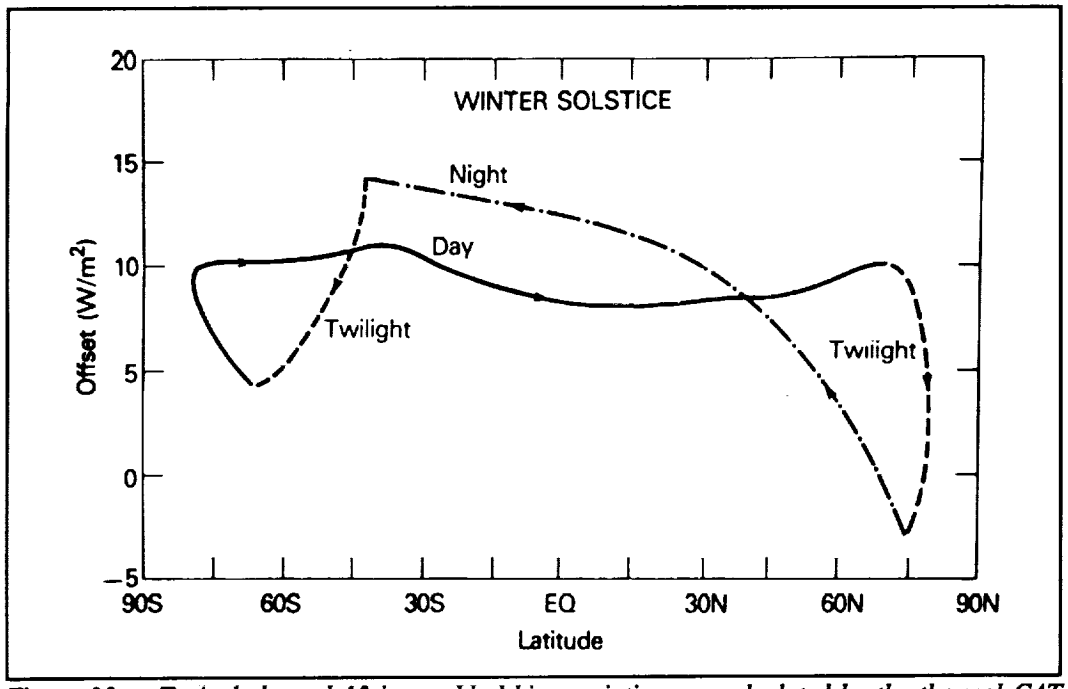

Figure 23a. Typical channel 13 intraorbital bias variations as calculated by the thermal CAT method for the winter solstice.

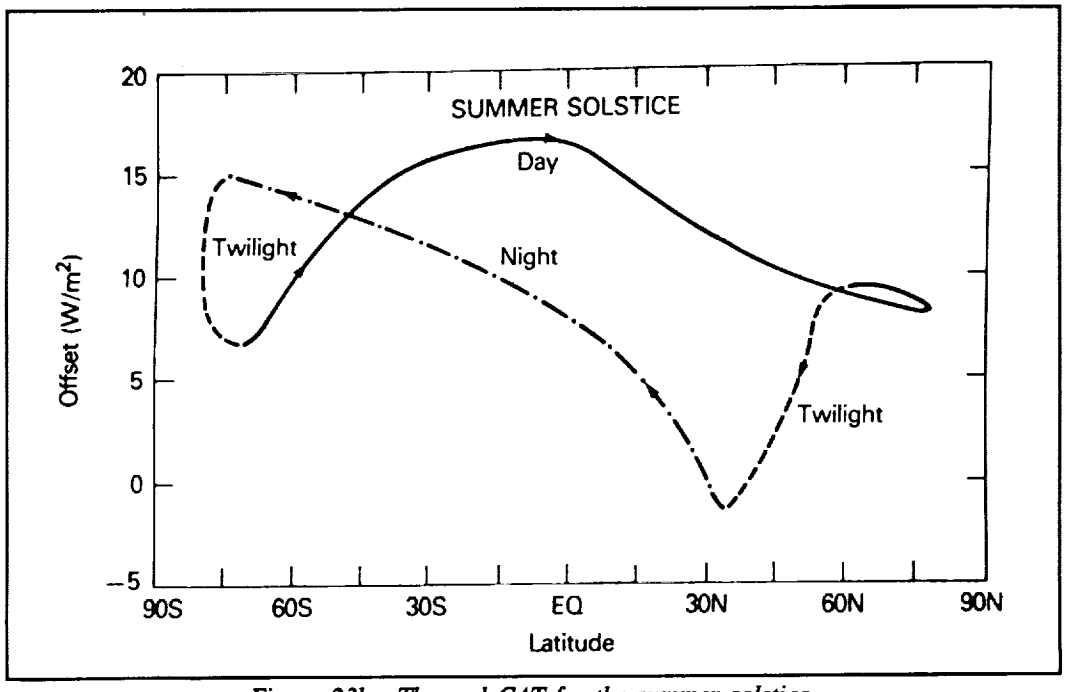

Figure 23b. Thermal CAT for the summer solstice.

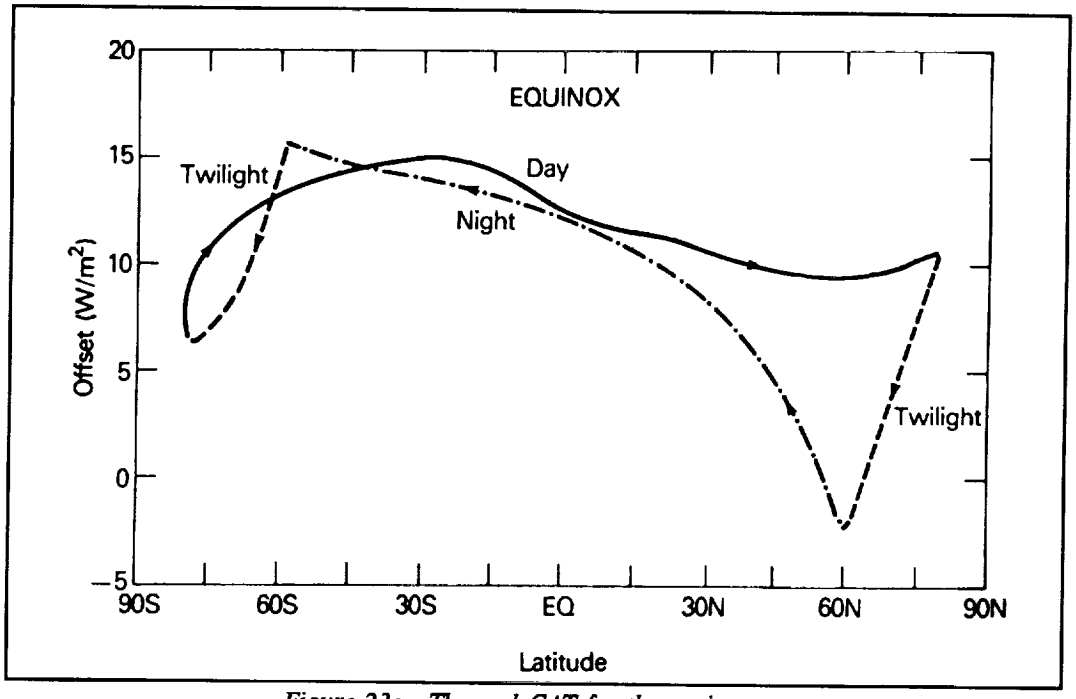

Figure 23c. Thermal CAT for the equinoxes.

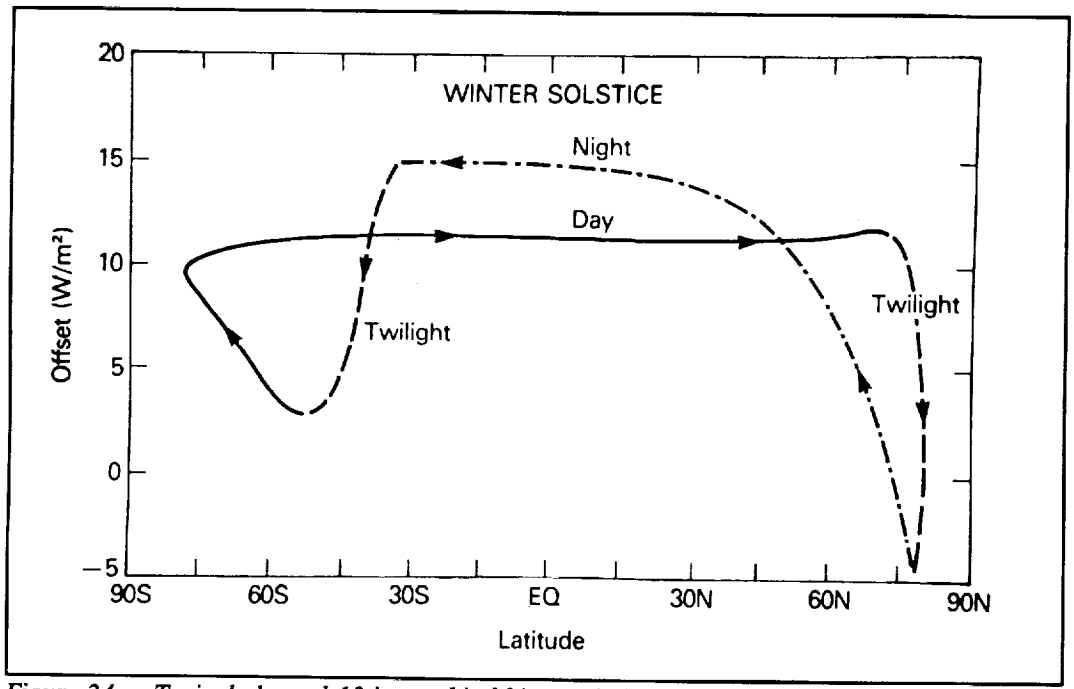

Figure 24a. Typical channel 13 intraorbital bias variations as calculated by global CAT metho d for the winter solstice.

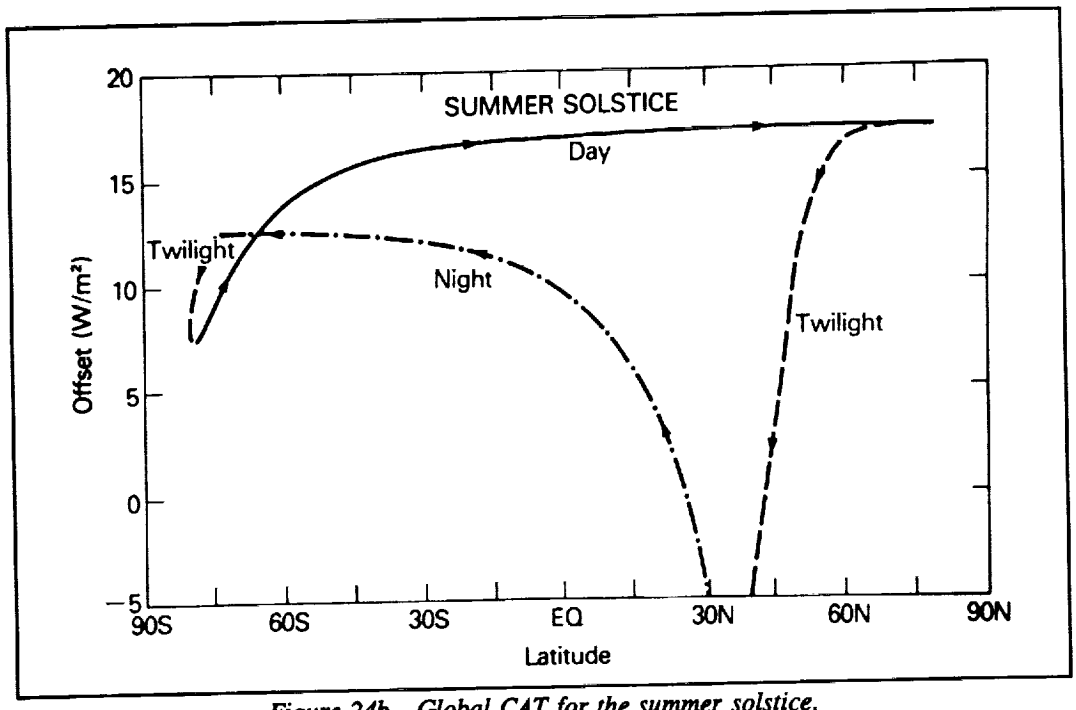

Figure 24b. Global CAT for the summer solstice.

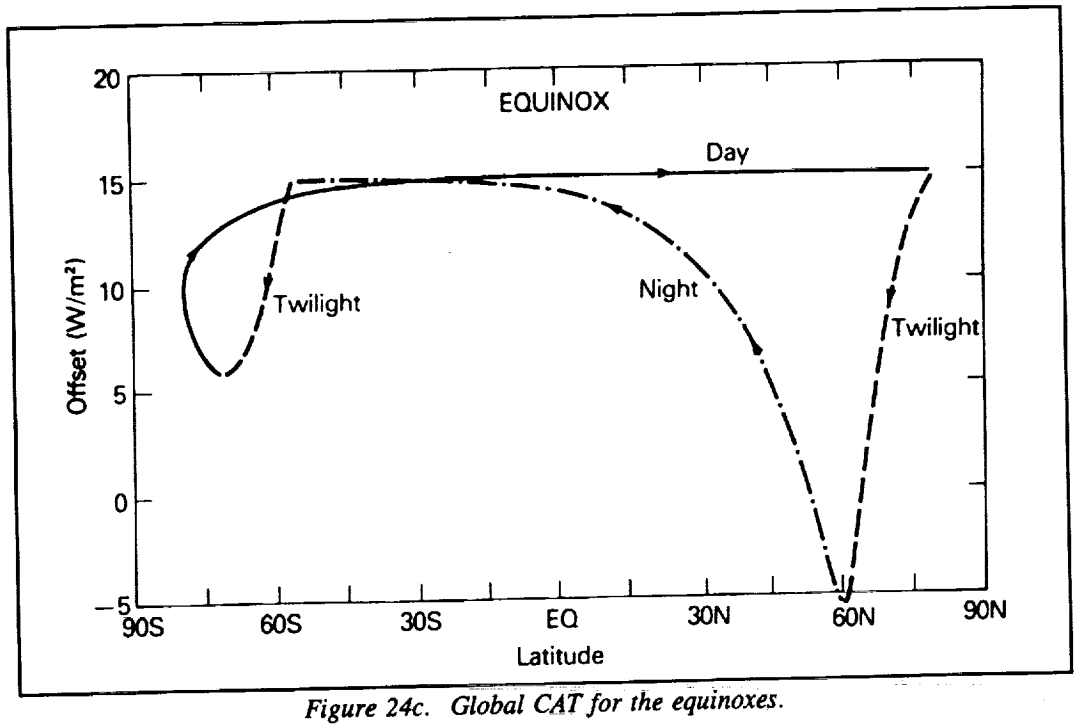

Figure 24c. Global CAT for the equinoxes.

All data were prepared in the normal way (Jacobowitz, et al., 1984a) and TOA averages were displayed on the ERB world grid which divides the Earth's surface into 2070 approximately equal regions. Each region or target area is ~500 km by 500 km. The average NFOV footprint is about 150 km by 150 km while the WFOV views the whole visible disk. However, the cosine-like response of the WFOV flat plate sensor makes the sensor most sensitive to radiation within a circle 1,200-km in radius, centered at the subsatellite point. Thus, the WFOV measurements produce a flux field smoothed over a cluster of target areas while the NFOV samples each target area separately.

At the top of the atmosphere, comparisons of the standard deviation of the difference between WFOV and NFOV datasets were made for the global and thermal CATs. This yields an estimate of total error. Recognizing that the total error is composed of calibration (in both the NFOV and WFOV) and sampling (for the WFOV in a 500-km^2 grid) errors, it is appropriate to try to arrive at estimates of the calibration errors as a residual, given the total and sampling errors. The sampling errors were obtained between the NFOV and pseudo-WFOV fields, where the latter were obtained synthetically by "flying" a simulated Nimbus-7 ERB experiment over an Earth composed of the NFOV target area data, thereby eliminating calibration errors.

If all sources of error are uncorrelated, the total error variances is simply the sum of the individual error variances, or

$$\sigma^2 \text{ (Total)} = \sum_{i=1}^{n} \sigma_i^2 \tag{13}$$

Neglecting any source of error other than sampling and filtered-channel calibration (such as total-channel or NFOV calibration errors), N = 2 and

$$\sigma^2 \text{ (Total)} = \sigma^2 \text{ (Calibration)} + \sigma^2 \text{ (Sampling)} \tag{14}$$

The WFOV data were compared both in their archived (MATRIX tape) format and in a higher resolution, deconvolved format. The deconvolution of the WFOV world grid data yields a somewhat higher spatial resolution product. The procedure is described in Ardanuy and Kyle (1986) and Ardanuy, et al. (1987). The results of the study are shown in Table 10; the thermal model produces a lower calibration error for June than the global model. For December, the global model is more accurate in replicating the NFOV dataset. (It is implicitly assumed that the NFOV data are correctly calibrated to within an offset.)

Table 10. Root mean square differences of global and thermal CAT WFOV irradiances relative to NFOV reference data.

Month	Calibration Adjustment Technique	Sensitivity Correction			Archived Product Difference (W/m^2)	Deconvolved Product Difference (W/m^2)		
		Channel 12 SW	Channel 12 LW	Channel 13	Total	Total	Sampling	Calibration
June	Thermal	1.002	1.022	1.019	14.8	13.7	11.8	6.9
June	Global	1.002	1.022	1.019	15.0	14.0	11.8	7.6
December	Thermal	1.003	1.023	1.031	14.3	12.7	10.8	6.7
December	Global	1.003	1.023	1.031	14.4	12.4	10.8	6.2

This study indicates that the global and thermal CAT's are about equally accurate. However, the global CAT is more stable and easier to use for production purposes. The thermal CAT requires careful quality control of all the required temperature measurements. And, while the thermal CAT is stable for any given operating schedule it must be re-evaluated and adjusted whenever the operating schedule changes. The operating schedule has changed a number of times since data collection started. Different operational configurations which would effect the thermal CAT include: scanner operating/scanner not operating; scan head temperature control on/scan head temperature control off; ERB 3-day-on and 1-day-off/ERB on full-time. During the first year, a number of special modes occurred including one period when the scanner was on for two-thirds of the orbit but off the other third. The apparent equal accuracy of the two schemes coupled with the additional effort and care required to use the thermal CAT led the ERB Experiment Team to adopt the global CAT.

8. LONGWAVE DOME HEATING CORRECTION IN CHANNELS 13 AND 14

An empirical examination of the Nimbus ERB data indicates that the time delayed, terrestrial longwave heating error in channel 13 at night (see Section 3.1.5) can be adequately removed by the simple algorithm

$$H_{LW\ heating}(t) = k \cdot H_{LW}(t-t_l) \tag{15}$$

where $H_{LW\ heating}$ is the induced shortwave signal due to LW dome heating, H_{LW} is LW irradiance at satellite altitude, k is a constant of proportionality, t is time, and t_l is lag time interval (Kyle et al., 1984). Analysis of eight 3-day datasets spaced throughout the first 20 data months of the Nimbus-7 ERB gave values of $k = 0.04$ and $t_l = 336$ s (21 major frames). The use of a more sophisticated correction algorithm does not appear warranted because of the other sources of error in the calibration and data analysis system. This correction becomes important only during the satellite day when the shortwave signal is none zero.

Channel 14 has a red glass dome between the two quartz domes, and this decreases the transmitted longwave signal and lengthens the decay time. Maschhoff et al. (1984) found that the channel 14

response to impulse longwave heating peaked about 10 minutes after the start of the heating pulse and fell to half the peak value about 23 minutes after the start of the pulse. Further, the channel 14 peak response to a given impulse was only 30 percent of the channel 13 response. Analysis of the flight data found no significant correlation between the channel 12 and channel 14 signals. The longwave heating effect on channel 14 is thus so small and smooth that making a separate correction is not worthwhile.

9. CONCLUSIONS AND DISCUSSION

9.1 Calibration Conclusions

The Nimbus-7 ERB WFOV Earth-viewing channels 12, 13, and 14 have been characterized in their satellite environment by accounting for sources of variation in the space data not considered in the prelaunch calibration equations. That is, calibration adjustments for the effects of: (1) extraterrestrial radiation incident on the detectors, (2) long-term degradation of the sensors, and (3) thermal perturbations within the ERB instrument have been derived and applied to the satellite observations. The first item is important in all the channels, the second mainly in channels 13 and 14, and third only in channels 13 and 14. The Sun is used as a stable calibration source to monitor the long-term degradation of the various channels. Channel 12, which is reasonably stable both to thermal perturbations and sensor degradation, is used as a reference and calibration transfer agent for the drifting sensitivities of the filtered channels 13 and 14. The result is a stable ERB dataset spanning 9 years (November 1978 to October 1987).

The principal difference between channels 13 and 14 and channel 12 lies in the filter domes covering former. These domes slow the flow of thermal radiation to and from the sensors and apparently amplify the thermal perturbations in these filtered channels. In addition, most of the long-term degradation in channels 13 and 14 is attributable to the gradual transmissivity loss of the domes. Thermal-induced perturbations in channel 12 (0.2 to over 50 μm) are of the order of fractions of a percent and normally below 1 W/m^2; thus, they are ignored as too small to accurately quantify. Long-term degradation of channel 12 is also small, in this case on the order of 1 or 2 percent. Thermal perturbations in the shortwave (0.2 to 3.8 μm) channel 13 are normally several percent (6 to 12 W/m^2) with sensor degradation reaching 16 percent by the fall of 1987. For the near infrared (0.7 to 2.8 μm) channel 14, thermal perturbations are between 1 and 4 percent (0.5 to 4 W/m^2) and cumulative sensor degradation is 8.5 percent by the fall of 1987.

Two independent algorithms were developed to correct for the in-orbit thermal perturbations in channels 13 and 14. These were the global CAT, which uses channel 12 as a calibration transfer agent, and the thermal CAT. The latter is an empirical algorithm which models thermal perturbations in channels 13 and 14 using temperature readings from several temperature monitors (TM's) in the ERB instrument package. Tests indicated that the overall accuracy of the global and thermal CAT's are equivalent, but the global CAT is easier to use. The global CAT was selected, therefore, for implementing the multi-year production program.

The ERB Science Team considers the global CAT algorithm optimal in that it would require a major effort to produce even a marginally better one. This is not to say that the algorithm is perfect. Direct sunlight contaminates the WFOV measurements during sunrise and sunset of every orbit between 90° and 121° of SZA. From 102° and 120° of SZA, the direct sunlight signal becomes large (cf. Figure 3). In the global CAT, a scattered sunlight correction is made from 90° to 99° of SZA permitting the interpolation of Earth flux values across the interval from 99° to 121° of SZA. While midpoint bias errors are less than 1 W/m^2 in the mean, the midpoint standard deviation is on the order of 5 to 6 W/m^2 (cf. Table 8). The purpose of this interpolation is to furnish outgoing longwave flux estimates for the time and space averages and for use in the dome heat correction in channel 13. The interpolation regions

lie in most cases at latitudes greater than 40°. Large sunrise and sunset solar heating perturbations in channel 13 also occur at high latitudes. The global CAT corrections for shortwave heating improve the original (MAT) calibration but an uncertainty of a few watts per meter squared still remains in the data (cf. Figures 23 and 24). In general, therefore, the global CAT calibration has a greater uncertainty at high latitudes than at medium and low latitudes. Qualitative evidence indicates that the transmission loss in the shortwave channel 13 is considerably larger in the ultraviolet than in the near infrared. Only a mean sensitivity (transmissivity) correction is made in the global CAT. No way was found to develop a wavelength dependent correction. An unknown, spurious element is thus introduced to monitored year-to-year regional ERB changes. Overall, however, the global CAT algorithm produces a dataset with a good multiyear calibration stability.

The long-term stability of the 9-year Nimbus-7 ERB dataset is indicated in Table 11. This table is taken from Ardanuy et al. (1992) and considers the time- and space-averaged products on the ERB MATRIX summary tape (EMST), the ERB solar measurements (Hoyt et al., 1992), and surface temperature variations from Hansen and Lebedeff (1987, 1988). Ardanuy et al. emphasize that physical year-to-year variations are being observed in the listed quantities. From 1980 to 1987, a downward drift of about 1 W/m^2 (0.4%) occurs in the OLR. This is thought to be due to calibration difficulties.

Table 11. The observed range of variation of radiation budget and related geophysical variables on annual, global scales (Ardanuy et al., 1992).

Parameter	Observed Range of Variation From Mean
Outgoing Longwave Radiation[1]	$\pm$0.4 Wm^{-2} [$\pm$0.2%]
Absorbed Shortwave Radiation[1]	$\pm$0.6 Wm^{-2} [$\pm$0.2%]
Net Radiation[1]	$\pm$0.5 Wm^{-2}
Solar Constant[2]	-0.7 to +1.3 Wm^{-2} [-0.05 to +0.1%]
Surface Temperature[3]	$\pm$0.1°

[The bracketed values are relative quantities; all other figures are absolute quantities.]
[1]9-year period, 1979 to 1987
[2]13 years, 1979 to 1991
[3]12 years, 1979 to 1990

Superimposed on this trend are year-to-year variations of $\pm$0.5 W/m^2 or less. When the OLR trend is removed, the year-to-year variations have a correlation of 0.97 with the annual global temperature variations. The OLR entry in Table 11 refers to the detrended OLR. The absorbed shortwave radiation does not show a long-term trend. This of course results in a slight increase in the net radiation in the latter years of the dataset. As described in Section 5, the LW and SW sensitivities of channel 12 are monitored by separate procedures. The shortwave uses the Sun as a calibration source, and during the period in question, the mean annual solar constant was stable to $\pm$0.075 percent. The longwave method assumed that long-term trends were instrument-related and should be removed. However, the long-term trend was estimated in a piecewise fashion. The LW procedure is potentially less accurate than the shortwave method.

An error analysis of the time- and space-averaged products in Table 11 would have to consider both calibration and time and space averaging problems. On a regional, monthly basis, time- and space-averaging problems can, at times, be dominant. The global mean longwave radiation is known to vary diurnally by between 5 and 10 W/m^2. Thus, a Sun-synchronous satellite whose equator crossing time

drifted over the years, the NOAA-9 for instance, might well introduce a spurious long-term trend into the measured longwave. However, the Nimbus-7 equator crossing time varied no more than 15 minutes during its first 9 years. Thus, on a global-annual basis, calibration difficulties should dominate for the Nimbus-7 dataset. This is particularly true when long-term stability is considered.

9.2 Discussion

The 9-year Nimbus-7 ERB dataset would become even more useful if it could be combined with previous and follow-on measurement sets to examine even longer term climate variations. A few studies have tried to do this. Ten years of combined Nimbus-6 and -7 ERB data have been analyzed by Bess et al. (1992) and Smith et al. (1990). Also, Minnis et al. (1993) used some Nimbus-6 and -7 data in conjunction with ERBE data (Barkstrom et al., 1989) in a recent study. However, as discussed by Kyle et al. (1990a, 1993a), considerable care should be taken when using combined datasets.

Earth radiation budget measurements are made instantaneously at the satellite. Calibration procedures are used to maintain the stability of the sensors over the lifetime of the experiment. However, the published end products normally consist of time- and space-averaged values at the top of the atmosphere. Besides the calibration, these products have been processed through inversion (Smith et al., 1986) algorithms. In addition, the regional and, to some extent, the global results are influenced by the time and space sampling patterns, rates, and averaging algorithms as well as by the size of the sensor field-of-view (FOV) on the Earth (Barkstrom and Smith, 1986; Brooks et al., 1987; Ardanuy et al., 1987). Thus, scanners with a nadir FOV of from 40 to 100 km across give much more regional detail than do WFOV whose effective footprints range from 1,200 to 1,600 km across. All of the factors from calibration to FOV tend to vary when two independent Earth radiation budget datasets are compared.

Global, annual averages from several existing Nimbus-6, -7, and ERBE datasets are listed in Table 12. Two versions of the Nimbus-6 ERB data are shown while six Nimbus-7 ERB versions (four WFOV and two NFOV) are represented. These differ in calibration procedures and often other processing algorithms differ also. Only one ERBE dataset is referenced but numerous others exist. In the ERBE experiment, identical instrument packages flew on three satellites: the Earth Radiation Budget Satellite (ERBS), and the NOAA-9 and NOAA-10 polar orbiting weather satellites. Each package contained scanner (NFOV), medium-field-of-view (MFOV), and WFOV sensors. Potentially datasets could be derived from each type of sensor on each satellite plus combinations of the three satellites using a particular type of sensor (see for instance Table A2 in Kyle et al., 1993a). The combined (ERBS/NOAA-9) scanner data are shown in Table 12. Comparison of the observed year-to-year variations in Table 11 with the different dataset results in Table 12 shows that mixing datasets can easily confuse the interannual signal which can be found in a single consistent dataset. For instance, note in Table 12 the three Nimbus-7 WFOV versions listed for the year (June 1979 to May 1980). A range of 2.4 W/m^2 appears in the three OLR means. But between 1979 and 1987, the annual global mean shows only a range of 1.38 W/m^2 (see Table 1 in Ardanuy et al., 1992). The observed range includes a part of the approximately 1 W/m^2 decrease assumed to be due to uncorrected sensor degradation. Thus the true range is probably closer to 1 W/m^2.

Table 12. Radiation Budget Annual Global Averages

Source	Solar Constant (W/m^2)	I_s[a] Solar Insolation (W/m^2)	F_{sw} Reflected[b] (W/m^2)	A (%)	OLR (W/m^2)	Net Radiation Formula[c] (W/m^2)
Nimbus-6 WFOV						
Campbell & Vonder Haar (1980)	1391			31	230	
Jacobowitz et al. (1979)						
(Adjusted results to scanner)	1391			31	234	
Nimbus-7 Original (11/78 to 10/79)						
Jacobowitz et al. (1984b)						
WFOV	1371.5	342.88	104.9	30.6	228.8	9.18
NFOV			113.5	33.1	232.7	-3.32
Nimbus-7 Reprocessed (6/79-5/80)						
Bess and Smith (1987)[d] WFOV					234.2	
Corrected Original WFOV[d]					236.6	
(MATRIX) WFOV	1371.5	342.88	103.2	30.07	235.4	4.4
(MLCE) NFOV			104.7	30.55	235.97	2.21
2/85-1/86 (MATRIX) WFOV			103.4	30.14	234.2	5.28
ERBE (N9 ERBS)	1365	341.25	102.1	29.92	233.99	5.16
2/85-1/86 (5° grid, scanner)						

[a] Calculated as (solar constant)/4
[b] Calculated using given albedo and solar constant
[c] Calculated by $NR = I_s - F_{sw} - OLR$
[d] Used original product adjusted by procedure given in Kyle et al. (1985)

Each of the listed datasets assumed the Sun had a constant luminosity when calculating the albedo. However, each experiment chose a solar constant measured during the experiment. The solar constant is the mean solar irradiance just outside the Earth's atmosphere. The chosen values are listed in column 2. Jacobowitz et al. (1984b) reviewed the first year (November 1978 to October 1980) of initially processed Nimbus-7 data. Note, in the last column, the 12.5 W/m^2 difference in the WFOV and NFOV annual net radiation. This was a clear sign that various algorithm and calibration problems existed. Just below, the reprocessed (MATRIX) WFOV and (MLCE) NFOV mean net radiations now agree to within 2.9 W/m^2. For the year (February 1985 to January 1986), the net radiation values listed for the Nimbus-7 WFOV and ERBE (N9ERBS) scanner (NFOV) agree to within 0.12 W/m^2. The significance of this close agreement is somewhat spoiled by the fact that both values are over 5 W/m^2 away from the presumed, theoretical value of zero. Barkstrom et al. (1989) use this difference from zero as one method of evaluating the mean error in the ERBE dataset.

Kyle et al. (1990a) compared the Nimbus-7 and ERBE datasets in some detail. Table 13 summarizes the results of the comparison of simultaneous Nimbus-7 and ERBS WFOV measurements at orbit crossing points. Both measurements are transformed to the top of the atmosphere (TOA) to allow the comparisons to be made. For consistency in the study, the same procedures were used to transform both the ERBS and Nimbus-7 measurements to the TOA. These results are listed under the heading "Calc". In the ERBE dataset, a somewhat more sophisticated inversion procedure was used which they labeled WS (WFOV shape factor). The results were essentially the same for both TOA ERBS values. The Nimbus-7 altitude was 950 km while that of the ERBS was about 610 km. Thus, the Nimbus-7 WFOV footprint was larger and this contributes to the size of the standard deviations in the measurements. Recall that there are shortwave (SW; 0.2 to 4 μm) and total (0.2 to over 50 μm) WFOV sensors. During satellite night the longwave (LW) radiation is measured by the total channel. During daylight

$$LW = Total - SW$$

The study indicated that the Nimbus-7 SW channel was in the mean reading 2.5 percent higher than the ERBS sensor but the difference was about 2 percent in April and October and about 3 percent or higher in July and November. The Nimbus-7 LW averaged about 0.6 percent less than the ERBS value with the difference larger in July and November than in April and October. The Nimbus-7 total channel read about 1.2 percent higher during the day but -0.8 percent lower at night than did the ERBS sensor. Again the differences were larger in July and November than in April and October.

The diurnal differences in the WFOV total channels is intriguing. As indicated in Section 3.2, the Nimbus-7 total channel intra-orbit thermal perturbations are thought to be of the order of 0 to 0.3 percent and were ignored because they were not well characterized. Studies by House (1989) and Green et al. (1990) found apparent intra-orbit perturbations in the ERBS and NOAA-9 WFOV LW and SW signals. Again no correction was made. Thus, it is possible that different thermal perturbation patterns caused some or all of the observed diurnal differences. It is also possible that the apparent diurnal variation may arise chiefly from differences in the longwave and shortwave calibrations of the two total channels. Note in Table 13 that the diurnal variation in the longwave difference is only 0.4 percent, but that in the daytime the Nimbus-7 shortwave values are 2.5 percent higher than those of the ERBS. Kyle et al. (1990a) compared the ERBS/NOAA-9 scanner and WFOV time- and space-averaged products for the months of April, July, and October 1985 and January 1986. In the global mean, the longwave products agreed to within 0.2 percent. But, the WFOV albedo was 3.24 percent less than the scanner result. This reinforces our hypothesis that longwave and shortwave calibration differences account for most of the diurnal variation in the total channel difference shown in Table 13.

Table 13. Top of the atmosphere comparison of ERBS and Nimbus-7 wide-field-of-view sensors

					Total			
	LW (AN)		SW (AN)		AN		DN	
	Calc	ERBE (WS)	Calc	ERBE (WS)	Calc	ERBE (WS)	Calc	ERBE (WS)
	4-Month Average (November 1984 and April, July, and October 1985)							
Difference, W/m^2	-1.2	-1.1	7.9	7.4	6.7	6.3	-2.0	-2.1
σ, W/m^2	3.3	3.3	2.0	4.0	3.4	3.9	0.8	0.5
Percent Difference	-0.5	-0.4	2.6	2.5	1.2	1.2	-0.8	-0.8

Monthly averaged differences with Nimbus-7 (N7-ERBS). The mean difference is removed before the monthly root mean square difference, σ, is calculated. Table taken from Kyle et al., 1990a.

The final TOA LW and SW Nimbus-7 and combined (NOAA-9/ERBS) products are compared for the months of April and July 1985 in Table 14 which is taken from Kyle et al. (1990a). Here calibration, sampling patterns, inversion, and time and space averaging differences are all involved, but fortunately some of the various differences tend to cancel. The (N9ERBS) scanner products are compared with the Nimbus-7 WFOV values in column 2 and with the (N9ERBS) WFOV values in column 4. In terms of bias, the scanner LW agrees about equally well with the two WFOV LW products but the scanner SW shows a slightly better agreement with Nimbus-7 WFOV SW product. In terms of RMS differences, the NOAA-9/ERBS WFOV longwave does a little better than the Nimbus-7 product. But, this may be partly due to the smaller ERBE WFOV footprints which yield a little better spatial resolution. When the shortwave RMS differences are examined, the ERBE WFOV products are no better than those from the Nimbus-7. The Nimbus-7 and (N9ERBS) WFOV values are compared in column 3. As expected, the RMS differences are considerably reduced compared to the WFOV/scanner comparisons because both WFOV footprints are large. Also note that longwave RMS differences are only about half the shortwave values. Both Tables 13 and 14 show that the Nimbus-7 and ERBE products agree better in the longwave than in the shortwave. The RMS differences indicate that regionally the WFOV products agree better than a WFOV/scanner mixture.

The Nimbus-7 measurements started in November 1978 while the ERBS WFOV measurements run from November 1984 through at least June 1993. This is a period of 14.5 years. But care should be observed in trying to combine the two datasets. The Nimbus-7 is in a Sun-synchronous, near-polar orbit, while the ERBS' orbit is inclined at 57° to the Earth's equator. The ERBS WFOV products are normally only studied up to 40° to 50° latitude so that the high latitude regions are missing. The NOAA-9 and NOAA-10 scanner products are of considerably shorter duration while most of the NOAA-9 and -10 WFOV measurements have not been carefully examined and discussed.

Table 14. Comparison of root mean square (RMS) and bias differences for N7 ERB WFOV, N9 ERBS scanner, and N9 ERBS WFOV for April and July 1985 (Kyle et al., 1990a).

	N7 WFOV-Scanner	N7WFOV-N9 ERBS WFOV	N9ERBS Scanner-WFOV
	Longwave (W/m^2)		
April 1985			
Bias	-1.65	-0.08	+1.56
RMS (with bias)	10.12	3.55	9.51
RMS (without bias)	9.98	3.55	9.36
July 1985			
Bias	-0.03	0.10	0.13
RMS (with bias)	10.30	3.98	9.74
RMS (without bias)	10.30	3.97	9.74
	Shortwave (W/m^2)		
April 1985			
Bias	1.2	3.61	2.41
RMS (with bias)	14.68	9.4	14.74
RMS (without bias)	14.63	8.63	14.55
July 1985			
Bias	0.63	3.8	3.17
RMS (with bias)	13.88	8.46	14.59
RMS (without bias)	13.87	7.56	14.25

Units are watts per square meter. Bias and RMS differences are given for $\pm 60°$ latitude region only. The WFOV results were interpolated to the scanner 2.5° latitude times 2.5° longitude global grid system before regional differences were taken.

The Nimbus-7 WFOV measurements extend through December 1992, but they have only been calibrated through October 1987 due to a shortage of resources. We recommend calibrating and releasing to the public the last 5 years of Nimbus ERB measurements. As discussed in Kyle et al. (1993a), the first 9 years of the ERB products have proven very stable and also scientifically useful and important.

10. REFERENCES

Ardanuy, P. E., and H. Jacobowitz, 1984: A Calibration Adjustment Technique Combining ERB Parameters from Different Remote Sensing Platforms into a Long-Term Data Set, J. Geophys. Res., 89, No. D4, 5011-5019.

Ardanuy, P. E. and J. Rea, 1984: Degradation Asymmetries and Recovery of the Nimbus-7 ERB Shortwave Radiometer, J. Geophys. Res., 89, No. D4, 5039-5048.

Ardanuy, P. E. and H. L. Kyle, 1986: El Niño and outgoing longwave radiation: observations from Nimbus-7 ERB. Monthly Wea. Rev., 114, 415-433.

Ardanuy, P. E., H. L. Kyle, R. R. Hucek, and B. S. Groveman, 1987: Nimbus-7 climate data set improvement, Part II: Improvement of the Earth radiation budget products and consideration of the 1982-1983 El Niño event. J. Geophys. Res., 92, No. D4, 4125-4143.

Ardanuy, P. E., H. L. Kyle, and D. Hoyt, 1992: Global Relationships Between the Earth's Radiation Budget, Cloudiness, Volcanic Aerosols, and Surface Temperature, *J. Climate*, **10**, 1120-1139.

Barkstrom, B. R. and G. L. Smith, 1986: The Earth Radiation Budget Experiment: Science and Implementation, *Rev. Geophys. Space Phys.*, **24**, 379-390.

Barkstrom, B., E. Harrison, G. Smith, R. Green, J. Kibler, R. Cess, and the ERBE Science Team, 1989: Earth Radiation Budget Experiment (ERBE), Archival and April 1985 Results, *Bull. Am. Meteorol. Soc.*, **70**, 1254-1262.

Bess, T. Dale, R. N. Green, and G. L. Smith, 1981: Deconvolution of Wide-Field-of-View Radiometer Measurements of Earth-Emitted Radiation, Part II: Analysis of First Year of Nimbus-6 ERB Data, *J. Atmos. Sci.*, **38(3)**, 474-488.

Bess, T. Dale and G. Louis Smith, 1987: Atlas of Wide-Field-of-View Outgoing Longwave Radiation Derived From Nimbus-7 Earth Radiation Budget Data Set, November 1978-October 1985, NASA-RP-1186, August 1987, 176 pages.

Bess, T. D., G. L. Smith, T. P. Charlock, and F. G. Rose, 1992: Annual and Interannual Variations of Earth-Emitted Radiation Based on a 10-year Dataset, *J. Geophys. Res.*, **97**, 12,825-12,835.

Brooks, D. R., E. F. Harrison, P. Minnis, and J. T. Suttles, 1986: Development of Algorithms for Understanding the Temporal and Spatial Variability of the Earth's Radiation Balance, *Rev. Geophys.*, **24**, 422-438.

Campbell, G. G. and T. H. Vonder Haar, 1980: An Analysis of Two Years of Nimbus-6 Radiation Budget Measurements, *Atmos. Sci. Pap.*, **320**, Colorado State University, Ft. Collins, 83 pages.

Campbell, W. A., R. S. Marriott, J. J. Park, 1980: Outgassing Data for Spacecraft Materials, NASA Reference Publication 1061, National Aeronautics and Space Administration, Washington, DC 20546.

Cline, A. K., 1974: Scalar- and Planar-Valued Curve Fitting Using Splines Under Tension, *Comm. ACM 17*, **4**, 218-220.

Gillette, R. B., B. H. Kenyon, 1971: Proton-Induced Contaminant Film Effects on Ultraviolet Reflecting Mirrors, *Applied Optics*, **10(3)**, pp. 545-551.

Green, R. N., F. R. House, P. W. Stackhouse, X. Wu, S. A. Ackerman, W. L. Smith, and M. J. Johnson, 1990: Intercomparison of Scanner and Nonscanner Measurements for the Earth Radiation Budget Experiment, *J. Geophys. Res.*, **95**, 11,785-11,798.

Hall, D. F., 1980: Flight Experiment to Measure Contamination Enhancement by Spacecraft Charging, SPIE Proceedings, *Optics in Adverse Environments*, **216**,.

Hansen, J. and S. Lebedeff, 1987: Global Trends of Measured Surface Air Temperature, *J. Geophys. Res.*, **92**, 13,345-13,372.

Hansen, J. and S. Lebedeff, 1988: Global Surface Air Temperatures: Update Through 1987, *J. Geophys. Res. Lett.*, **15**, 323-326.

Hickey, J. R., and A. R. Karoli, Radiometric Calibrations for the Earth Radiation Budget Experiment, Appl. Opt., 13, 523-533, 1974.

Hickey, J. R., D. J. Brinker, and P. Jenkins, 1992: Studies of Effects on Optical Components and Sensors: LDEF Experiments AO-147 (ERB Components) and S-0014 (APEX), An Article in LDEF-69 Months in Space, Second Post-Retrieval Symposium, NASA Conference Publication 3194 (Part 4), 1375-1388.

House, F. B., 1989: An Intercomparison of Longwave Measurements by ERBE Radiometers on the NOAA-9 and ERBS Satellites, *Adv. Space Res.*, **9(7)**, (7)15-(7)18.

Hoyt, D. V., H. L. Kyle, J. R. Hickey, and R. H. Maschhoff, 1992: The Nimbus-7 Total Solar Irradiance: A New Algorithm for its Derivation, *J. Geophys. Res.*, **97(A1)**, 51-63.

Jacobowitz, H., W. L. Smith, H. B. Howell, F. W. Nagle, and J. R. Hickey, 1979: The First 19 Months of Planetary Radiation Budget Measurements from the Nimbus-6 ERB, J. Atmos. Sci., 36, No. 3, 501-507.

Jacobowitz, H., H. V. Soule, H. L. Kyle, F. B. House, et al., 1984a: The Earth Radiation Budget (ERB) Experiment: An Overview, J. of Geophys Res., 89, No. D4, 5021-5038.

Jacobowitz, H., R. J. Tighe, and the Nimbus-7 ERB Experiment Team, 1984b: The Earth Radiation Budget Derived From the Nimbus-7 ERB Experiment, *J. Geophys. Res.*, **89**, 4997-5010.

King, M. D., and R. J. Curran, 1980: The effect of nonuniform planetary albedo on the interpretation of earth radiation budget observation, J. Atmos. Sci., 37, 1262-1278.

Kruger, R. and H. Shapiro, 1980: Experiments on the Effect of Ultraviolet on Contamination in Vacuum Systems, NASA Technical Memorandum 81999, Goddard Space Flight Center, Greenbelt, MD 20771.

Kyle, H. L., F. B. House, P. E. Ardanuy, H. Jacobowitz, R. H. Maschhoff, and J. R. Hickey, 1984: New In-Flight Calibration Adjustment of the Nimbus-6 and -7 ERB Wide Field of View Radiometers, J. of Geophys. Res., 89, No. D4, 5057-5076.

Kyle, H. L., Ardanuy, P. E., and E. J. Hurley, 1985: The Status of the Nimbus-7 ERB Earth Radiation Budget Data Set. Bull. Amer. Meteor. Soc., 66, 1378-1388.

Kyle, H. L., K. L. Vasanth, and the Nimbus-7 ERB Experiment Team, 1986: Some Characteristics Differences in the Earth's Radiation Budget over Land and Ocean Derived from the Nimbus-7 ERB Experiment. J. Climate Appl. Meteor., 25, pp. 958-981.

Kyle, H. L., A. Mecherikunnel, P. Ardanuy, L. Penn, B. Groveman, G. Campbell, and T. H. Vonder Haar, 1990a: A Comparison of Two Major Earth Radiation Budget Data Sets, *J. Geophys. Res.*, **95**, 9951-9970.

Kyle, H. L., R. R. Hucek, B. Groveman, and R. Frey, 1990b: User's Guide: Nimbus-7 Earth Radiation Budget Narrow-Field-of-View Products, NASA RP-1246, 76 pages.

Kyle, H. L., J. R. Hickey, P. E. Ardanuy, H. Jacobowitz, A. Arking, G. G. Campbell, F. B. House, R. Maschhoff, G. L. Smith, L. L. Stowe, and T. Vonder Haar, 1993a: The Nimbus Earth Radiation Budget (ERB) Experiment: 1975-1992, *Bull. Amer. Meteor. Soc.*, **74**, 815-830.

Kyle, H. L., D. V. Hoyt, J. R. Hickey, R. H. Maschhoff, and B. J. Vallette, 1993b: Nimbus-7 Earth Radiation Budget Calibration History—Part I: The Solar Channels, NASA RP-1316, 80 pages.

Maschhoff, R., A. Jalink, J. Hickey, and J. Swedberg, 1984: Nimbus-ERB Sensor Characterization for Improved Data Reduction Fidelity, J. of Geophys. Res., 89, No. D4, 5049-5056.

Mearns, A. M., 1969: Thin Solid Films, **3**, pp. 201-208.

Minnis, P., E. F. Harrison, L. L. Stowe, G. G. Gibson, F. M. Denn, D. R. Doelling, and W. L. Smith, Jr., 1993: Radiative Climate Forcing by the Mount Pinatubo Eruption, *Science*, **259**, 1411-1415.

Predmore, R. E., H. Jacobowitz, and J. R. Hickey, 1982: Exospheric Cleaning of the Earth Radiation Budget Solar Radiometer During Solar Maximum, Paper Presented at Proceedings of Society of Photo-Optical Inst. Eng. (SPIE) (Tech. Symp. East, Arlington, VA, May 3-7, 1982), **338**, pp. 104-113.

Smith, G. L., R. N. Green, E. Raschke, K. M. Avis, J. T. Suttles, B. A. Wielicki, and R. Davies, 1986: Inversion Methods for Satellite Studies of the Earth's Radiation Budget: Development of Algorithms for the ERBE Mission, *Rev. Geophys.*, **24**, 407-421.

Smith, G. L., D. Rutan, T. P. Charlock, and T. D. Bess, 1990: Annual and Interannual Variations of Absorbed Solar Radiation Based on a 10-Year Data Set, *J. Geophys. Res.*, **95**, 16,639-16,652.

Smith W. L., J. Hickey, B. Howell, H. Jacobowitz, D. T. Hilleary, and A. J. Drummond, 1977: Nimbus-6 Earth Radiation Budget Experiment, Appl. Opt., 16, 306-318.

Soule, H. V., 1983: Nimbus-6 and -7 Earth Radiation Budget (ERB) Sensor Details and Component Tests, NASA Technical Memorandum TM-83906, 88 pages.

APPENDIX A
WFOV SENSITIVITY FROM OBSERVATIONS OF THE SUN

Recent analysis of the Nimbus-7 solar data indicates that the mean annual solar irradiance varied over a range of 0.15 percent between 1979 and 1987. In the period 1979 to 1984, day-to-day variations could amount to ± 0.15 percent with extreme values of ± 0.25 percent. The Sun was considerably quieter in the period 1985 to 1987 (Hoyt et al., 1992). Thus, to about ± 0.1 to ± 0.15 percent accuracy, the Sun is a constant source of shortwave radiation and the possibility of using an assumed constant Sun as a calibration reference source for the ERB WFOV radiometers depends, in part, on the magnitude of the sensitivity changes that occur in these channels. To address this question, we refer to the results of the WFOV time series analyses presented in Section 5 treating the MAT irradiance data. Assuming actual trends in ERB fluxes are small, these studies reveal cumulative sensitivity changes of about 1 to 2 percent in channel 12, 14 to 16 percent in channel 13, and 7 to 8.5 percent for channel 14 over the 9 years of processed data. Since these observed changes are large compared to fluctuations in the solar constant, the Sun indeed represents a suitable calibration source for the WFOV channels, especially on time scale of years or half-years.

During normal operation, the WFOV channels face the nadir direction and the unencumbered ring of space visible in every measurement spans an angular distance of only about 0.1°. In comparison, the solar disk subtends a nadir angle of 0.5°, roughly five times the width of the space ring. As a result, a variable and uncertain fraction, but never the total solar irradiance, strikes the detector during brief moments at satellite sunrise and sunset when the Sun actually enters the sensor FOV of space. To obtain a better and prolonged view of the Sun, the Nimbus-7 satellite is periodically tilted off nadir by some 2° to 3°, either toward (pitch-up) or away from (pitch-down) the direction of the satellite velocity vector. These scheduled events, which we refer to as "pitch" maneuvers, normally take place every twenty-four days and last for periods of about 10 minutes centered on a sunblip event. In the pitched satellite configuration, the full solar disk fits within the detector's unencumbered view of space and, once within, the Sun remains fully visible for about 42 seconds, or roughly ten 4-second WFOV observations. A large part of the detector FOV also views the Earth and the total channel response consists of radiation from both the Sun and the Earth.

Figure A1 shows a sequence of 4-second channel 12 observations associated with the passage of the Sun across the radiometer FOV of space during a satellite pitch-up event (12 July 1988). Time is measured relative to the first observation of the series. Pitch-ups are performed at sunrise, during satellite egression from the Earth's shadow, when the Sun is positioned ahead of the spacecraft. This occurs in the Southern Hemisphere and usually within 20° of the South Pole. Notice the relatively flat background signal (about 100 W/m^{-2}) at the start of the data sequence. Neglecting any thermal forcing of the detector signal, an assumption that is most suitable to the total channels 11 and 12, this segment of the curve represents the sensor response to terrestrial radiation alone. In particular, neither direct nor stray sunlight can strike the sensor at this time because both the receiver and baffle are hidden in darkness.

As the spacecraft approaches satellite sunrise, the faint signals of solar radiation refracted and scattered by the atmosphere out of the Earth's geometrical shadow are the first shortwave observations recorded. This twilight radiation quickly strengthens over a period of five or six measurements (about 20 seconds) until finally, at the shadow's edge, the solar disk becomes visible. Within two more observations it is fully exposed. An approximately linear decrease in detect response now follows that lasts for some 10 to 12 observations. This is the region of interest for calibration determination as the reference source, the full solar disk, now illuminates the detector. Although the total response appears to decrease linearly in this region, this is only because of the small range of angles that is considered. In fact, all of the

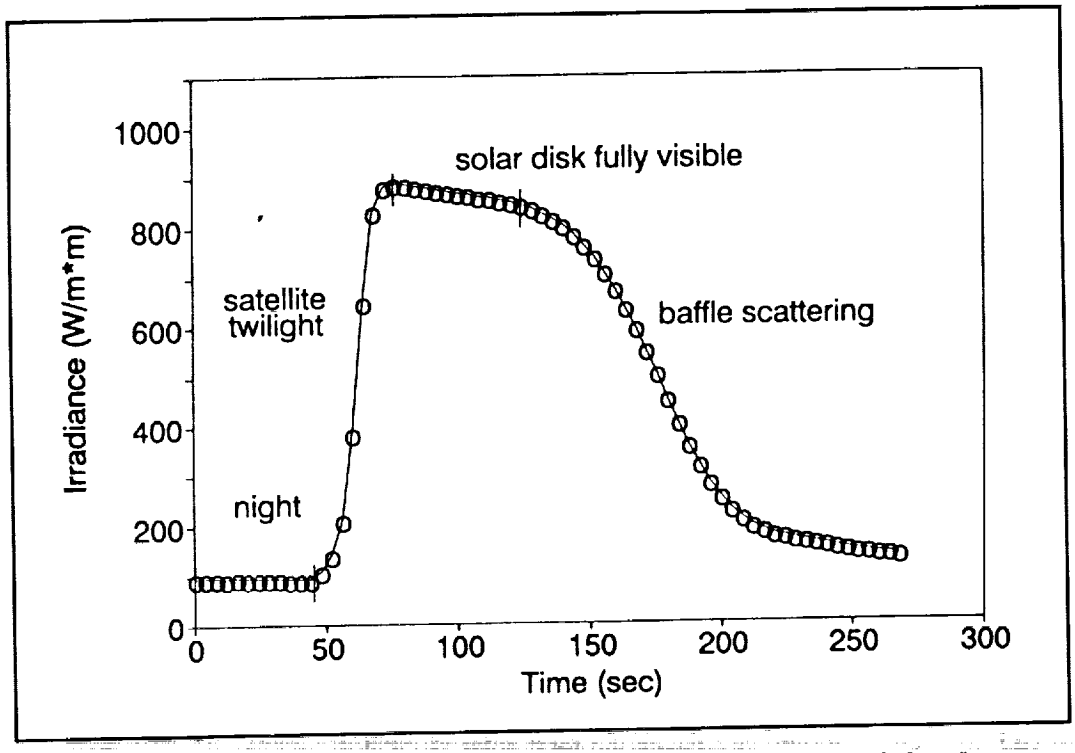

Figure A1. Channel 12 solar observations during a satellite calibration, "pitch-up" event at satellite sunrise on July 12, 1988. The time is calculated from the beginning of the event. At the top of the curve, the sensor views the unobstructed solar disk at about a 60° angle for approximately ten 4-second measurement periods.

WFOV channels have angular response functions that are similar to that of a flat-plate detector (cf. Figure 4) with departures from a cosine function being due to the out-of-field response added by the channel baffles. The total irradiance drops off quickly as the Sun exits the detectors unencumbered FOV beyond the calibration shoulder, as the linear region is termed. This decrease is not nearly as rapid as occurs during solar entry into the detector FOV because baffle scattered stray light during satellite day acts to sustain the high signal levels. The irradiance time curve of Figure A1 is traversed in the reverse direction during a pitch-down maneuver at sunset, but otherwise the same fundamental elements of the signal profile appear.

A.1 THE SENSITIVITY EQUATION FOR THE TOTAL CHANNELS 11 AND 12

It is assumed that a linear equation in the form

$$\Delta W = \frac{V - V_0}{S} \qquad \text{(A1)}$$

relates the net irradiance at the receiver (ΔW) to the measured voltage (V), and the channel offset voltage (V_0) and sensitivity (S). The net irradiance is the difference of the absorbed ($I_{absorbed}$) less the emitted ($I_{emitted}$) fluxes. The absorbed flux is the product of the receiver absorptivity (a_r) and incoming flux ($I_{incoming}$) while the emitted flux, due to thermal emission from the receiver, is characterized as that of a gray body with an emissivity ϵ_r. Equating the receiver absorptivity and emissivity, the energy balance equation is rewritten as

gray body with an emissivity ϵ_r. Equating the receiver absorptivity and emissivity, the energy balance equation is rewritten as

$$I_{incoming} - \sigma T_r^4 = \frac{V - V_0}{\epsilon_r S} \tag{A2}$$

where σ is the Stefan-Boltzmann constant and T_r is the temperature of the receiver surface. The incoming irradiance originates from several sources including Earth, Sun, and baffle. Baffle emission is combined with receiver thermal emission, as was done previously in Eq.(1) via the detector configuration factor F_D, to give a single term representing net emission from the receiver. Since the ERB instrument contains no temperature monitors that are positioned to directly record T_r, this temperature is determined, as before, in terms of the detector thermopile temperature T_D and the thermopile temperature correction factor k. Thus, the measurement equation is expressed as

$$I_{sun} + I_{earth} = \frac{V - V_0}{\epsilon_r S} + F_D\sigma(T_D + kV)^4 \tag{A3}$$

where I_{sun} and I_{earth} are the incoming solar and terrestrial irradiance components at the detector.

During normal data processing, values of the channel sensitivity and voltage counts are converted to estimates of the terrestrial irradiance via the calibration equation. Now we wish to invert this procedure—to derive the channel sensitivity given the measurement equation and estimates of the solar irradiance and voltage counts. The contribution of the Earth irradiance and possible thermal perturbations on the net detector response are also required. Estimates of these signals are obtained for a time of solar illumination by extrapolating the channel response (V) from a period of darkness. Consider a set of observations taken within the Earth's shadow prior to (pitch-up) or after (pitch-down) the peak of the sunblip spike. To ensure that no residual solar irradiance is present in these data and to keep the extrapolation interval as short as possible, voltage counts are collected during a 2-minute interval beginning (ending) 3 minutes prior to (after) the peak of the sunblip spike. The trend line in V is extrapolated to nearby times (i.e., to adjacent latitudes) and approximates the channel response due only to the flux of Earth radiation and thermal perturbations. In particular, the terrestrial and thermal perturbation irradiance component within the sunblip (V_{earth}) is given, using (A3), by

$$I_{earth} = \frac{V_{earth} - V_0}{\epsilon_r S} + F_D\sigma(T_D + kV_{earth})^4 \tag{A4}$$

Solar irradiance (I_{sun}) on the detector is variable, due both to rapid changes in incidence angle of the solar beam during any one pitch event, and slow to seasonal changes in the Earth-Sun distance (d). Thus, the magnitude of I_{sun} is obtained by modulating the solar constant with the inverse of d^2 and the angular response function of the channel, $g(\theta)$. Here θ is the angle from the sensor normal direction. The expression for I_{sun} is given by

$$I_{sun} = \frac{I_0}{d^2} g(\theta) \tag{A5}$$

with d in astronomical units. Values of $g(\theta)$ for channels 11 and 12 are given in Table A1 over the range of incidence angles encountered for the unencumbered Sun during a satellite pitch maneuver. For the black-painted baffle channel 11, $g(\theta)$ is essentially a cosine function whereas an approximately 12% increase (compared to a cosine function) is obtained for the shiny baffle channel 12.

Table A1. Angular response of the Nimbus-7 WFOV radiometers channel 11 (black baffle) and channel 12 (shiny baffle) for 11 observations at the limit of the unencumbered FOV

Angle of Incidence (°)	Cosine Response (Black Baffle)	Observed Response (Shiny Baffle)
57.96	0.5305	0.5900
58.19	0.5271	0.5875
58.41	0.5237	0.5845
58.64	0.5203	0.5816
58.87	0.5168	0.5786
59.11	0.5134	0.5758
59.34	0.5099	0.5733
59.57	0.5063	0.5706
59.80	0.5029	0.5681
60.03	0.4994	0.5650
60.27	0.4959	0.5590

Although the detector emissivity/absorptivity is high and believed to be between 0.92 and 0.96, exact values of this parameter are not known. Consequently, during sensitivity determination we determine not S alone, but the product of S and ϵ_r, termed the effective sensitivity (S′). Combining (A3), (A4), and (A5), a solution for S′ is given by

$$S' = \frac{V - V_{Earth}}{\frac{I_0}{d^2} g(\theta) - F_D \sigma \left[(T_D + kV)^4 - (T_D + kV_{earth})^4\right]} \tag{A6}$$

In deriving (A6), we made the first order approximation that the shortwave and longwave sensitivities for channel 12 or channel 11 were identical. However, in the solar calibration tests, the shortwave energy source (the Sun) is dominant. Thus, it is essentially the shortwave sensitivity that is derived. When the module temperature (T_m) dependence of S′ is removed, the effective sensitivity at T_m=25°C is computed via the expression

$$S'(25) = \frac{V - V_{Earth}}{\frac{I_0}{d^2} g(\theta) - F_D\sigma\left[(T_D + kV)^4 - (T_D + kV_{earth})^4\right]} - a(T_m - 25) \qquad \text{(A7)}$$

In (A7), a is the sensitivity temperature adjustment coefficient.

A.2 THE SENSITIVITY EQUATION FOR THE FILTERED CHANNELS 13 AND 14

The filtered channels are covered by infrared domes which act to block longwave but pass shortwave radiation components. To a first approximation, we drop I_{earth} from the energy balance equation of these channels since the longwave component is absorbed, and the shortwave signal is negligibly small at this point in the orbit (SZA $\simeq$ 120°). The further assumption of near thermal equilibrium within dome cavity allows us to also drop the receiver emission term on the RHS of (A3). This hypothesis implies that thermal baffle and dome radiation absorbed by the receiver nearly cancel thermal radiation emitted by the receiver. Instead of (A3), the measurement equation for the filter channels is

$$I_{sun} = \frac{V - V_0}{\epsilon_r S} \qquad \text{(A8)}$$

where only the constant prelaunch calibration estimates of the channel 13 and 14 offset voltages (V_0), -43 and -44 counts respectively, are available. We now know that these values are not suitable for all conditions met in the orbital environment, but they may still be used to detect relative sensitivity changes over a long time series of data (see, for example, Figures 4c and 4d).

The solar irradiance incident on the detectors is once again determined by modulating the solar constant by the inverse of the Earth-Sun distance squared and the angular response function of the channels. The value of the solar constant for channel 13 is 1372 W/m^2 and slightly less than half of this or 679.1 W/m^2 is used for the near-infrared channel 14. In view of the many approximations leading to (A8), $g(\theta)$ is represented simply as $\cos(\theta)$. Solving for the apparent sensitivity S′, we obtain

$$S' = \frac{V - V_0}{\frac{I_0}{d^2}\cos(\theta)} \qquad \text{(A9)}$$

In terms of the apparent sensitivity at 25°C, we have

$$S'(25) = \frac{V - V_0}{[1.0 + 0.01a(T_m - 25)]\frac{I_0}{d^2}\cos(\theta)} \qquad \text{(A10)}$$

where a is the sensitivity temperature adjustment coefficient.

A.3 Accuracy Estimates

Figures 5a-5d illustrate the time series of WFOV solar sensitivity estimates for channels 11 through 14, respectively. Random errors in the analysis procedure can be approximated directly from the figures by examining fluctuations about the long-term sensitivity drifts. These long-term changes are envisioned as simple trend lines in the total channels while quadratic or higher order polynomial fits are more appropriate for the filtered channels. Performing this analysis qualitatively for the pitch-up data, random sensitivity errors in the range of ± 0.03 c/Wm^{-2} are estimated for channels 11, 12, and 13. Variability in channel 14 appears to be somewhat greater reaching a range of ± 0.05 c/Wm^{-2} during the last 2.5 years of the time series. Possible sources of this error are fluctuations in the value of the solar constant, large thermal perturbation signals, and inaccuracies in the estimation of the terrestrial background signal, solar zenith angle, and satellite attitude.

Bias errors for channels 11 and 12 are expected to be small since only minor thermal perturbations occur in these channels and the global CAT best-estimates of the detector configuration factor, F_D (Table 5), are utilized in evaluating Eq.(A7). Moreover, linear extrapolation of the nighttime sensor voltage into the sunblip region serves to remove not only the influence of these small thermal perturbations from the sensor response, but also those of terrestrial radiation and any channel offsets that may be present in the detector readings. Solar stray light in channel 12 has also been considered via the channel angular response function. Thus, the random error estimates provide here for channels 11 and 12 are probably also representative of their absolute sensitivity errors. In contrast, thermal perturbations in the measurements of channels 13 and 14 are unaccounted for since no extrapolation of the nighttime signal (a partial measure of thermal perturbations) is performed. In Section 7 we have shown that these perturbations exert an important influence on the irradiances of the filtered channels and that this influence varies with season. Thus, while useful for relative sensitivity determinations, the solar calibrations of the filtered channels are probably subject to seasonal biases. This is clearly seen in Figures 5c and 5d where the seasonal cycle of sensitivity anomalies (i.e., departures from low-order polynomial curves fit to the data) are apparently correlated for all years.

APPENDIX B
THERMAL MODELS

B.1 INTRODUCTION

The ERB WFOV channels, in response to the various thermal gradients that develop, are biased from the desired measurements by an amount proportional to the heat flow. Should both knowledge of these heat gradients and the resultant biases they produce be available at certain periods or locations, then a calibration can be developed which characterizes this effect in a form which can be used to correct the measurements at all other times. The shortwave channels 13 and 14 should read zero during the satellite night, while numerous temperature monitors (TMs) throughout the ERB instrument report on many of the desired heat gradients. Using the temperature gradient information plus the observed nonzero, nighttime biases, thermal models have been developed. It is further demonstrated that these models are also applicable during the satellite day. These models are useful calibration tools, but they are more technically demanding than the adopted global CAT calibration models (cf. Section 7).

The four ERB WFOV channels are subjected to external thermal forcing along a number of paths. The general heat flow is illustrated in Figure B1. In it, 3 types of heat transfer are considered: shortwave radiation (including both that impinging directly on the spacecraft from the Sun and that first reflected by the Earth/atmosphere system), longwave radiation emitted by the sensors and by the Earth (long wavelength radiation emitted by the Sun can be neglected), and conduction. Sections B.2 through B.4 discuss, in turn, each of these variable heat sources: the Sun, the Earth, and power sources within the satellite. The temperature monitors are briefly discussed in Section B.5. Finally, the construction and verification of the channel 13 thermal model is described in Section B.6.

B.2 SHORTWAVE RADIATION

The angular deviation of the Earth-Sun radius vector from its projection in the Nimbus-7 orbital plane is small in all seasons (due to the near local-noon, Sun-synchronous orbit of the spacecraft) and, in fact, goes to zero twice per year with changes in the solar inclination. Because of the this and its 955 km altitude, the satellite is illuminated along a nearly 240° arc of every orbit, or 70 of every 104 minutes in an orbital period. The solar irradiance striking the satellite has a mean flux density of 1370 W/m^{-2}, but it varies by up 6 percent due to the seasonal cycle in the Earth-Sun distance. More importantly, however, are orbitally-varying intensity changes that occur along the surfaces of the Nimbus observatory because of changes in the angle of incidence of the solar radiation on any particular surface.

Consider a spherical coordinate system with origin at the satellite and having a polar, +Z axis along nadir, in the direction of the Earth (Figure B2). The X-Y plane is tangent to the orbital arc, with relative azimuth measured from the direction of the flight, the +X axis. Egressing from the Earth's shadow, direct solar radiation is first incident at spacecraft sunrise as the solar disks creeps from behind the Earth's shadow at a local colatitude (or nadir) angle of about 60 degrees. At this angle and orbital position, the bottom (including the 4 WFOV channels) and the front (including the 10 channel solar telescope array) of the spacecraft are illuminated. There is a brief in-field glimpse of the Sun by the WFOV channels and then an extended period of out-of-field response until the Sun crosses the local X-Y plane. At this time the Nimbus-7 satellite is, with nominal pitch, directly over the Southern Hemisphere terminator (this is also the position at which the once-per-orbit solar observations are taken by the solar sensors). The Sun is now directly illuminating only the front of the spacecraft. At the same time, solar radiation reflected specularly and diffusely off the Earth's surface is striking the bottom and front of the spacecraft and the ERB experiment. It is worth noting that, during the Southern Hemisphere summer, Antarctica is by far the largest source of shortwave radiation at the altitude of this satellite. As the

spacecraft continues along an orbital pass, the Sun sweeps through the maximum local colatitude angle (Sun near the -Z axis) with the ERB experiment fully shadowed by the satellite. Then, with nearly a 180° shift in azimuth, the colatitude of the Sun begins decreasing and the rear of the ERB experiment becomes increasingly illuminated. As the solar colatitude decreases to less than 90°, an out-of-field response occurs, followed by the in-field response, and finally spacecraft ingression into the Earth's shadow (cf. Figure 3).

B.3 LONGWAVE RADIATION

Longwave radiances emitted by the Earth are incident upon the spacecraft within 60° of local colatitude (nadir). The long wavelength fluxes at the top of the atmosphere (a convenient level where the radiative transfer from below and within the atmosphere can be neglected) vary, as with the shortwave radiation, with position. To a first approximation, the latitudinal variation consists of minima at both poles of the Earth and at the ITCZ, and maxima in the subtropics. However, longwave variability is on the order of a factor of 4 less than that of shortwave and, unlike shortwave radiation, there is very little difference between the radiation fields at night and during the day. Of course, the spacecraft is exposed to deep space over the remainder of the sphere, while the Earth-facing WFOV channels, but not the detectors, view space through a ring between 60 and 90 degrees colatitude. The detectors of the 2 total channels have baffles which restrict their view to the Earth plus a small space ring, while the shortwave and near-infrared channels do not directly view the Earth in the longwave region of the spectrum due to the presence of the Suprasil-W filter domes. The outer domes do, however, view deep space and the Earth; this leads to the interesting thermal interaction termed "longwave heating" (Section 8 and Kyle, et al., 1984) as the innermost filter domes, which are viewed by the detectors on the 2 channels warm and cool in a delayed response to the variations in the longwave Earth forcing.

B.4 CONDUCTION

In addition to these energy sources, each of the experiments on the Nimbus-7 satellite, when operating, consumes power generated by the solar panels and stored in the spacecraft's batteries. The locations of the other instrument assemblies relative to one another and to the spacecraft are shown in Figure B2. Notice that the SMMR instrument with its parabolic antenna sits directly above the ERB module. Approximate power consumptions are given in Table B1. It is evident that the heat produced by the operation of the various experiments and modulated by their duty cycles, as with that heat created by the absorption of short and long wavelength radiation, can act to bias the ERB WFOV radiometer measurements. As illustrated in Figure B1, the WFOV channels are not thermally isolated from the rest of the spacecraft. Additional information about the ERB instrument, itself, can be found in Section 1.2.

B.5 TEMPERATURE MONITORS

A detailed investigation of the time variability of the ERB sensor temperatures has been conducted (Figure 22 and Maschhoff et al., 1984). These thermistor TM's have an absolute accuracy of approximately 0.1°C, with a repeatability on the order of 0.1 millidegree. These monitors are sited throughout the experiment at numerous sensing locations. These include monitor sites with a large amount of external exposure (e.g., on the total channel 12 field of view limiter and on the 2 total channel shutters), internal temperature measurements (e.g., the power supply area), and other TM's scattered about the ERB experiment. Figure B3 shows the complete ERB instrument module with its 10 solar channels facing in the direction of the satellite velocity vector, the 4 WFOV channels on the bottom left and facing nadir, and the biaxial NFOV scanner with a complement of four telescopes.

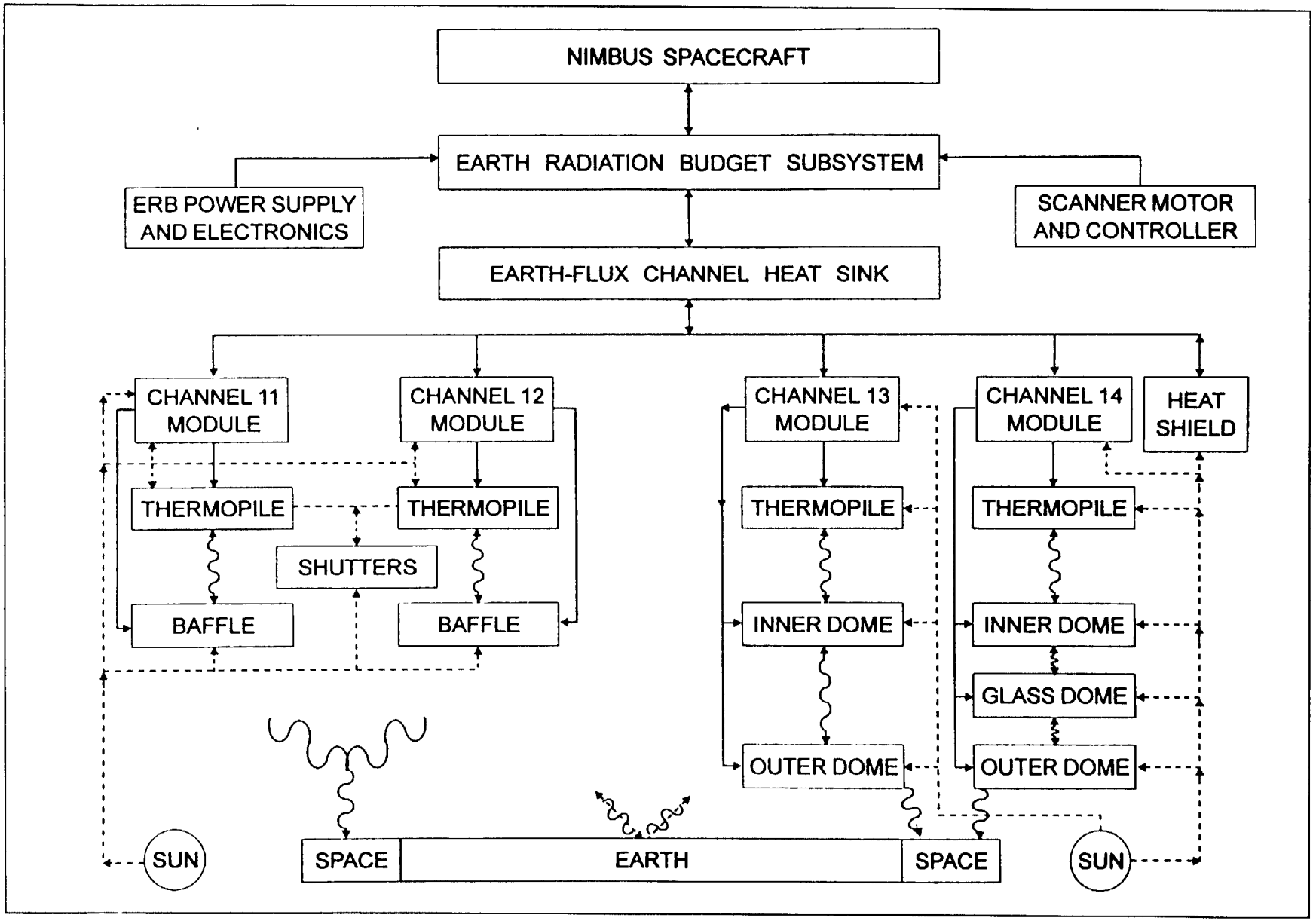

Figure B1. Diagram of heat flow paths around the four ERB WFOV sensors, channels 11-14. Heat flow both by conduction (solid lines) and by radiation are considered. Shortwave radiation is indicated by dashed lines and thermal radiation by wavy lines.

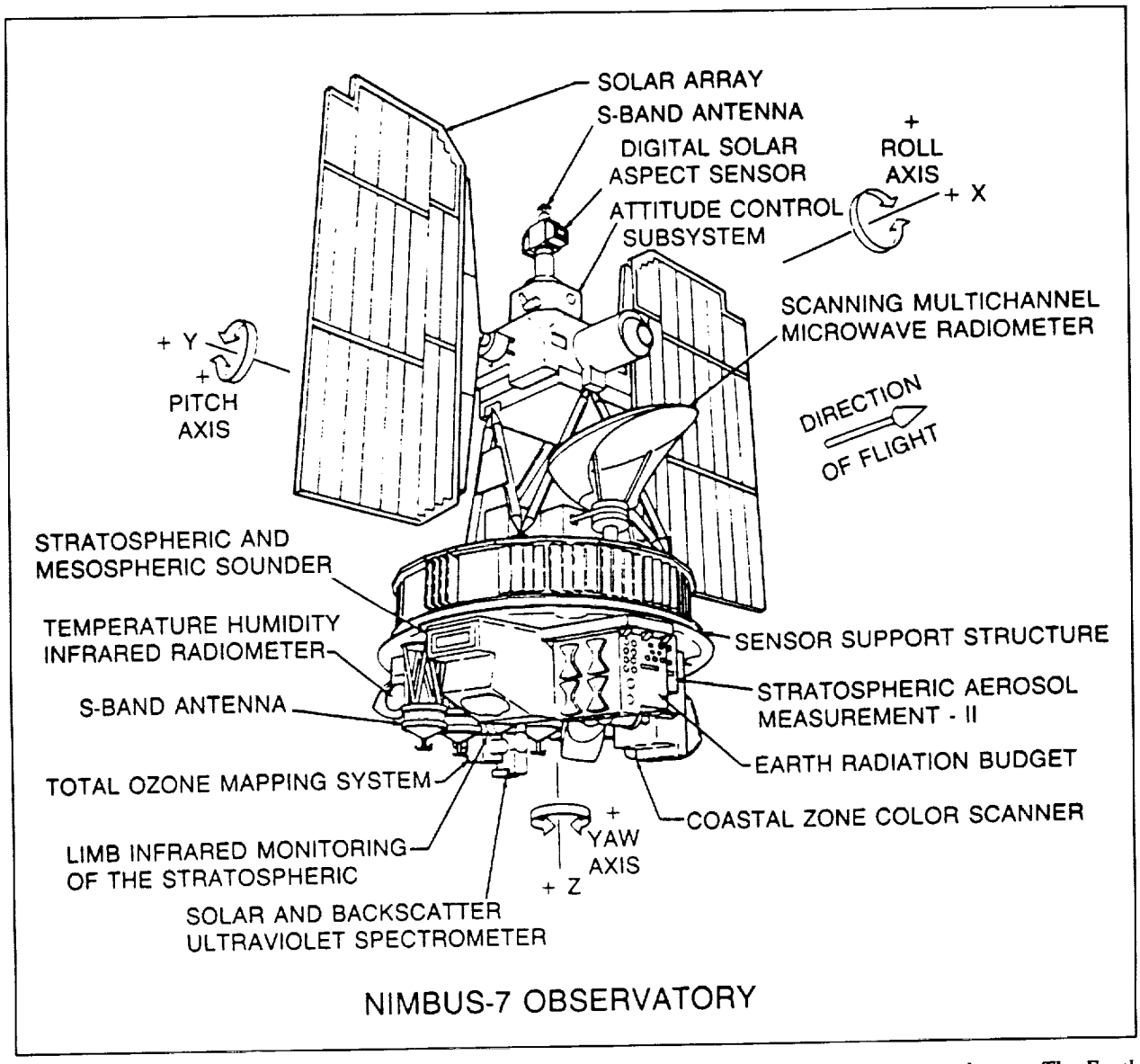

Figure B2.The in-flight configuration of the Nimbus-7 observatory and its various instrument packages. The Earth is towards the bottom of the page in the direction of the +Z-axis. The satellite moves in the direction of the +X-axis. The ERB instrument is at the bottom right with its solar sensors facing forward and the WFOV sensors on the bottom viewing the Earth.

Table B1. Power Consumption of the Active Experiments on Nimbus-7

Experiment	Original Power Requirement Planned[a] Full Time/Average (Watts)		Average Time On (%)	Effective Turn Off Date
CZCS	48.8	14.64	30	June 1986
ERB Scanner On	30.3	24.24	80	July 1980
ERB Scanner Off	23.5			
LIMS	30.63	24.50	80	June 1979
SAMS	18.4	14.72	80	July 1983
SAM II	12.3	0.98	8	
SBUV/TOMS	23.25	18.5	80	
SMMR Initial Channel 4 off Stop scan Channels 1 & 2 off Power off	59.4	29.7	50	 12 March 1985 25 August 1987 3 May 1988 6 July 1988
THIR	8.5	8.5	100	June 1985
Experiment Total	231.6	135.78		
Spacecraft		123.6		
Required Total Initial Power		259.39		

AVAILABLE SPACECRAFT POWER

Year	January (watts)	July (watts)
1979	287.0	264.8
1985	223.1	204.5
1987	215.1	198.6

Power supply degraded about 7.5% the first year and about 2.5% per year thereafter.

[a]The actual on time was variable particularly during the first year. Normally the SMMR schedule was 1-day-on/1-day-off, and the ERB was 3-days-on/1-day off. The ERB had long periods of full-time on after September 1983.

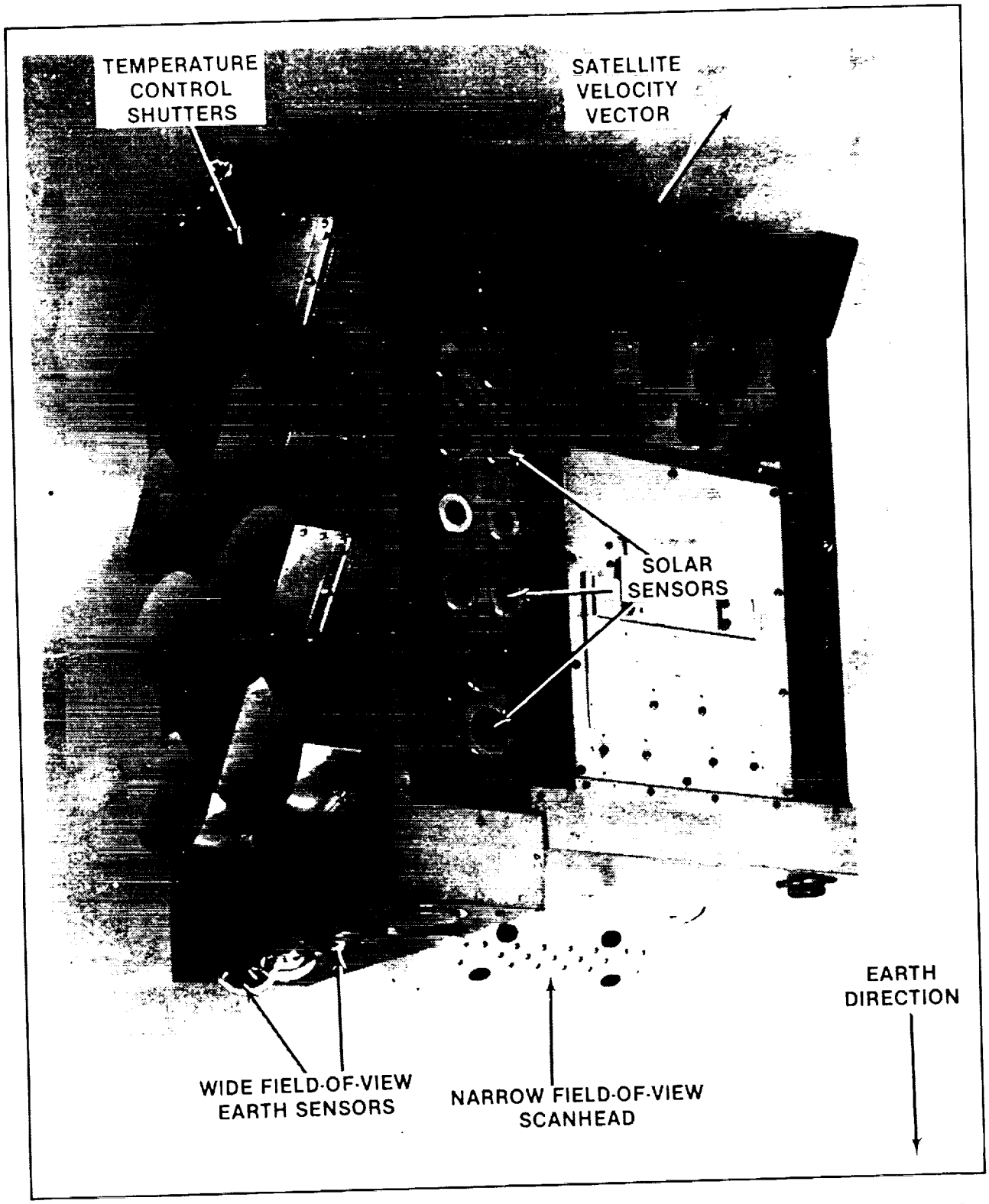

Figure B3. The ERB instrument package. The 10 solar sensors are on the front facing in the direction of the satellite velocity vector. The four WFOV channels and the NFOV scanner are on the bottom facing the Earth.

B.6 SELECTION OF TM SITES

Because, in the design of the ERB experiment, the locations of the TM's were not optimized to provide the maximum information content regarding thermally-induced biases, one would expect that temperatures taken at different locations will show a greater or lesser skill at contributing to the description of the error variance. The TM locations of significance for a study of channel 13 are given in Table B2, but only those monitors contributing additional independent information should ultimately be chosen to form any calibration model. To obtain a nearly complete set of independent temperatures, a stepwise linear regression procedure was applied to a dataset consisting of twelve 3-day duty cycles (one duty cycle per month) chosen from the fourth data year. Linear combinations of TM temperatures were sought that minimized the error variance of the predicted thermal perturbations on the data. Note that actual thermal perturbations in the nighttime data of the filtered channel data are easily specified since these are defined as the non-zero signal in the channel readings after removal of longwave heating. Although models of nine and more TM temperatures were tested, the error variance was found to be insensitive to the number of predictors after eight or more variables were included. Thus, a hierarchy of models containing from 1 to 8 variables (or terms) was obtained. The temperatures of the 8TM-predictor model plus three other temperatures (chosen on the basis of physical considerations) and their 55 possible differences were then taken as a basis set and used to produce additional models. Although it will be demonstrated that the amount of variance and root mean square (RMS) error explained by the important temperature-difference models is only slightly greater than that for the temperature models, the temperature differences do illustrate suggested heat flow paths of importance through the ERB instrument and are thus more representative of a physical model (see Figure B4a and B4b).

The predictors chosen, the percent variance explained, and the RMS error of the regression fit for the hierarchy of models obtained in this manner are given in Table B3. With this technique, over 90 percent of the variance of the non-zero nighttime "irradiance" signal is explained by all models with 4 or more terms. It is worth noting that, when the temperature differences are admitted explicitly as model variables, they are selected preferentially over the temperatures alone for the first 6 terms of the expansion. In addition, for up to the 6-variable models, the difference models (Model B) explain more variance than the corresponding temperature models (Model A) with the same number of terms. The temperature differences selected by the first 5 sets of Model B are those illustrated in Figure B4.

For the 1-variable model, the single parameter which explains the most error variance (as defined by a non-zero shortwave measurement bias during spacecraft night) is the temperature difference between the 2 total-channel shutters. This term alone accounts for some 72 percent of the signal variance, with a correlation of around 0.85. It should be noted at this time that, when a thermally-driven offset model is developed, some physical consideration must be given to the fact that the model will be applied and evaluated in an environment other than where it is developed. Specifically, although the thermal domain will be similar, as evidenced by reference to the TM time series during day and night, there will be additional forcing functions present during the day that do not act at the night: e.g., shortwave radiation. Thus, the choice of such a model may not be appropriate as possible excessive shortwave heating of the shutters may damage the utility of this model during the day. As additional terms are included, temperature differences from other areas of the experiment are selected. These each contribute additional variance to the regression equation. The models with 4-8 predictors are all within 1 percent of explained variance of each other, and within a RMS error range of less than 0.1 W/m^2.

Table B2. TM Sites Selected for Further Analysis	
TM Designation*	TM Location
T02	Channel 12 shutter
T20	Channel 10 thermopile base
T24	Channel 20 telescope post
T35	Solar channel assembly casting top
T36	Solar channel assembly casting bottom
T37	Solar channel assembly shield attach point
T39	Earth-flux assembly front
T48	Channel 10 module
T49	Channel 13 module
T57	Shortwave scanning channel detector
T58	Alpha sweep gear box and motor
T60	Post amplifier synch demod area
T61	Channel 11 shutter
T71	Power supply area
T74	Remote scan α-axis bearing
T75	Channel 12 field of view stop

The various temperature differences chosen have some significance as indicators of thermal gradients within the ERB experiment. There are 3 dominant forcing modes at work driving the observed offset errors. These are thermal transients and gradients modulated by the orbital cycle (with a period of 104 minutes), the operational duty cycle (with a period of from 2 to 4 days) and the annual cycle. The thermal gradients set up by these individual effects may or may not be oriented along different thermal paths (and thus sensed by a different pair of TM thermistors). Further, the effects induced by these different forcing modes are unlikely to be orthogonal. That is, the information contained in one of the relationships (e.g., the orbital cycle) may also contain some information content that at least partially describes another of the relationships (e.g., the duty cycle). As such, a "hybrid" form of calibration-adjustment equation is sought, which solves for the entire set of transient responses simultaneously. For this reason, the developmental dataset, from which the model is developed, contains information from 36 days of ERB nighttime data. This includes: the orbital cycle (the entire spacecraft night is used, though by necessity, not the day); the duty cycle (3-day sets, each composed of 1 full duty cycle are used); and the annual cycle (a single duty cycle from each month of the year is used).

In the solution for the 4 variable difference model, for example, there is a temperature difference suggestive of a thermal gradient across the solar channel assembly (the +X axis), along the NFOV scanning channel assembly (the +Z axis), from the ERB interior towards nadir coupled through the total channel 12 field of view stop, and an interior gradient near the power supply (possibly aiding in the description of the turn-on transient associated with the duty cycle).

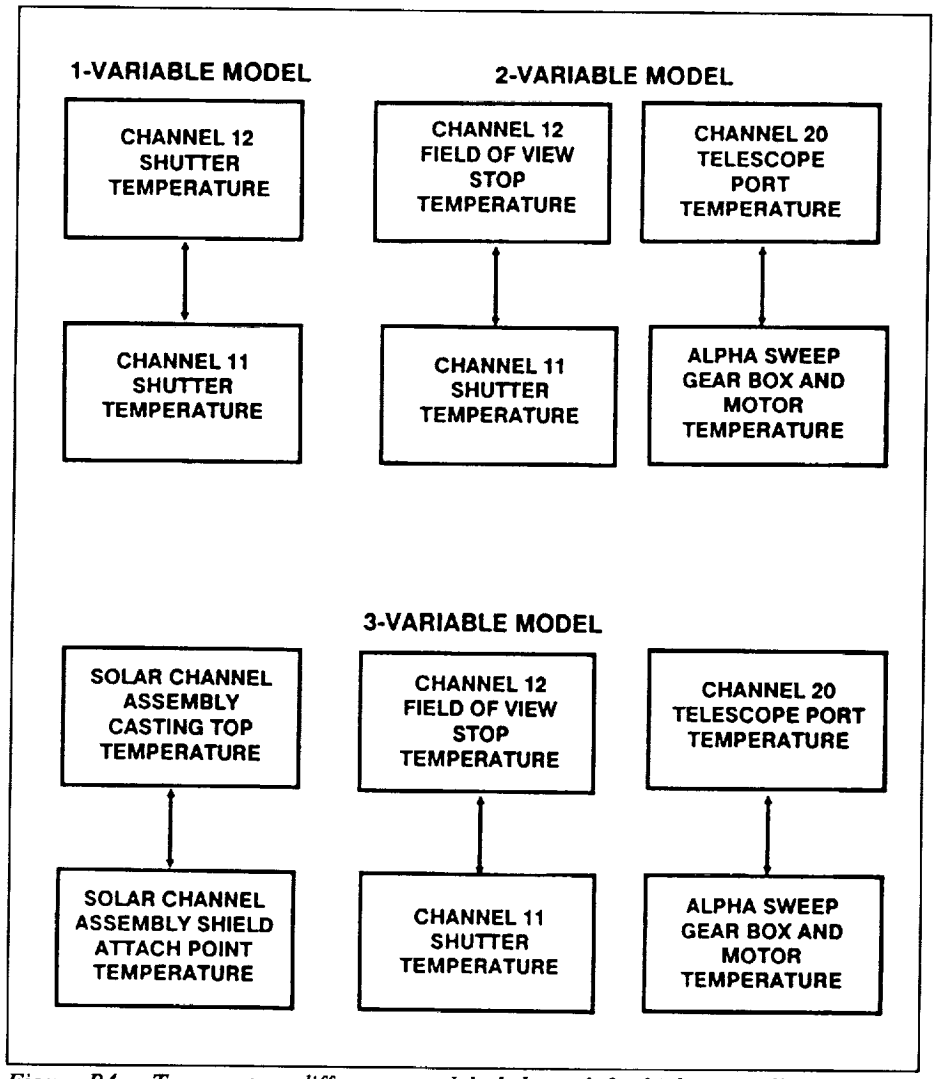

Figure B4a. Temperature difference models 1 through 3 which optimally predict the nighttime behavior of channel 13 (see the text).

As is common with any inversion procedure, there is a limit as to the total amount of information available in the dataset. What is desired is an accurate mathematical specification of the thermally induced offset bias of the WFOV filtered-channel measurements. What is specified is a set of TM measurements taken at various locations about the ERB experiment. As models of increasing complexity are derived, a point is eventually reached where the additional terms contribute very little independent information to the solution. One way this becomes manifested is through the individual coefficient amplitudes (Table B4). When only a few terms are included in a model, the amplitudes are relatively small (e.g., relate a temperature gradient change of 1°C to an offset change of 1 or 2 W/m^2). However, when the amplitudes for 7 or 8 terms are retrieved, the amplitudes reach the order of 10 W/m^2 per °C. Here, not only the precision of the individual TM's becomes a problem, but additionally the model itself has become very sensitive. Recall that, while the model is developed at night, it will actually be applied during the day. Even a small amount of unsuitability in the model as applied will, in the higher-order models, yield defective calibrations. The degree of instability present is further illustrated in Table B5, which presents the condition number of the matrix being inverted, as well as the set of eigenvalues resulting from the solution of the hierarchy of thermal calibration-adjustment models. Here again, while the eigenvalues are of the same order of magnitude for the first several models, indicating a stable and well-behaved solution,

the last several models have eigenvalues that range in value by 5 or 6 orders of magnitude. In addition, the large condition number indicates that the resultant matrix is ill-conditioned and any errors in the data or model are amplified by the solution vector. Therefore, it appears desirable to truncate the solution to an equation with less than 7 or 8 terms.

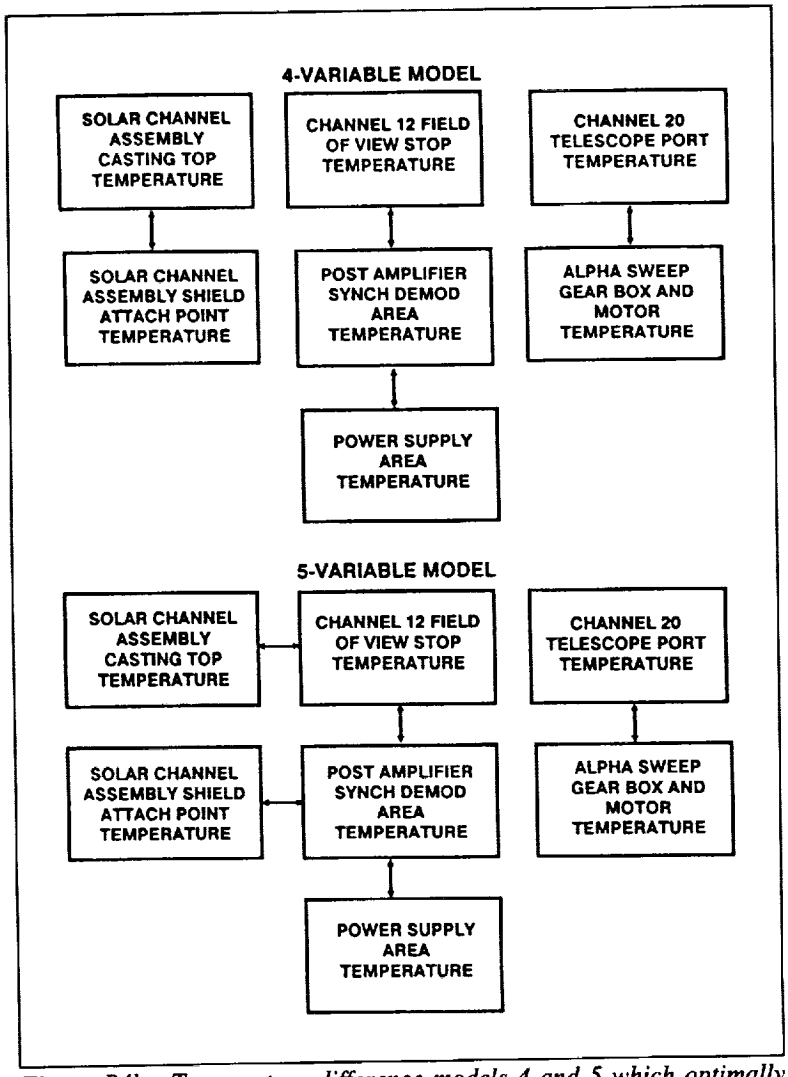

Figure B4b. Temperature difference models 4 and 5 which optimally predict the nighttime behavior of channel 13 (see the text).

The technique we have employed is to make use of a dataset that is independent from that used in constructing the model. Table B6 compares model errors when applied to data of year 4 (used to develop the model) and year 5. The table shows that an explained error variance plateau is reached when models of four or more terms are applied to independent data (year 5). For practical purposes, models with 4-8 temperature difference terms perform equally well. Thus, a 4-variable model was chosen as the optimal calibration-adjustment equation.

Table B3. Predictors chosen, percent variance explained, and RMS error of the fit for the hierarchy of models fit to the channel 13 irradiances at night. TD0275, for example, is the temperature difference between T02 and T75.

Model A (temperatures only)

Number of Predictors	1	2	3	4	5	6	7	8	Explained Variance (%)	RMS Error (W/m^2)
1	T02								48.7	3.33
2	T61	T71							84.4	1.84
3	T20	T24	T75						87.3	1.66
4	T35	T36	T57	T71					90.4	1.44
5	T24	T35	T39	T71	T74				90.7	1.42
6	T24	T35	T39	T48	T71	T74			90.8	1.41
7	T24	T35	T48	T58	T60	T71	T75		91.2	1.38
8	T24	T35	T37	T58	T60	T61	T71	T75	91.4	1.37

Model B (temperatures and temperature differences)

Number of Predictors	1	2	3	4	5	6	7	8	Explained Variance (%)	RMS Error (W/m^2)
1	TD0261								72.1	2.45
2	TD2458	TD6175							87.6	1.64
3	TD2458	TD3537	TD6175						89.5	1.50
4	TD2458	TD3537	TD6071	TD6075					90.5	1.43
5	TD2458	TD3537	TD3760	TD6071	TD6075				91.1	1.39
6	TD2458	TD3575	TD3760	TD3761	TD6075	TD6171			91.2	1.38
7	T58	TD2458	TD3575	TD3760	TD3761	TD6075	TD6171		91.3	1.37
8	T37	T58	TD2458	TD3575	TD3761	TD5860	TD6075	TD6171	91.4	1.37

The final and necessary step in the development of this model is its transfer to daytime conditions. The absolute accuracy of this model has been examined in Section 7.4. Here we develop confidence in the utility of this model by applying a consistency check. Specifically, it has been shown that, except perhaps for models with only one or two terms, the temperature difference models perform quite well and consistently in modelling the nighttime offset bias. It is now reasonable to ask the following question: will these models also yield consistent solutions when applied to the daytime data? This question is addressed by the results tabulated in Tables B7a and B7b. In Table B7a, the 8 calibration adjustment models are applied to mid-latitude nighttime data and, not surprisingly, give generally quite similar correction estimates. This is in contrast to the results shown in Table B7b, where the offset bias estimates during the day deviate substantially from model to model. Results for the relatively unstable models with 5-8 terms are self consistent, yet these deviate from the corrections suggested by the relatively more stable models with 3-4 terms.

This divergence in model solutions is evidently the result of the instability. This is demonstrated graphically in Figure B5a, where a constraint is applied to the model solution. The technique employed is termed "Ridge regression". With it, the least-squares equation takes the form

$$X = [A^T A + KH]^{-1} A^T B \qquad \text{(B1)}$$

where X is the solution vector of regression coefficients, B and A the input sensor bias vector and matrix obtained by the formation of the normal equations and H the identity matrix.

Table B4. Increase in the coefficient amplitudes as the temperature difference model complexity increases from 1 to 8 terms

	Number of Terms							
Term	1	2	3	4	5	6	7	8
1	1.51	2.06	1.88	2.54	3.13	3.02	0.54	-9.37
2		-1.58	1.32	2.83	5.13	4.87	3.53	10.58
3			1.58	3.49	-2.14	-9.64	4.85	3.83
4				-0.90	7.87	7.96	-9.14	5.05
5					-5.90	-5.97	7.79	8.08
6						7.24	-5.92	-12.45
7							6.92	-9.85
8								6.96
RMS coefficient amplitude ($W/m^{-2}{}^{o}/C^{-1}$								
	1.51	1.84	1.61	2.62	5.24	6.80	6.13	8.81

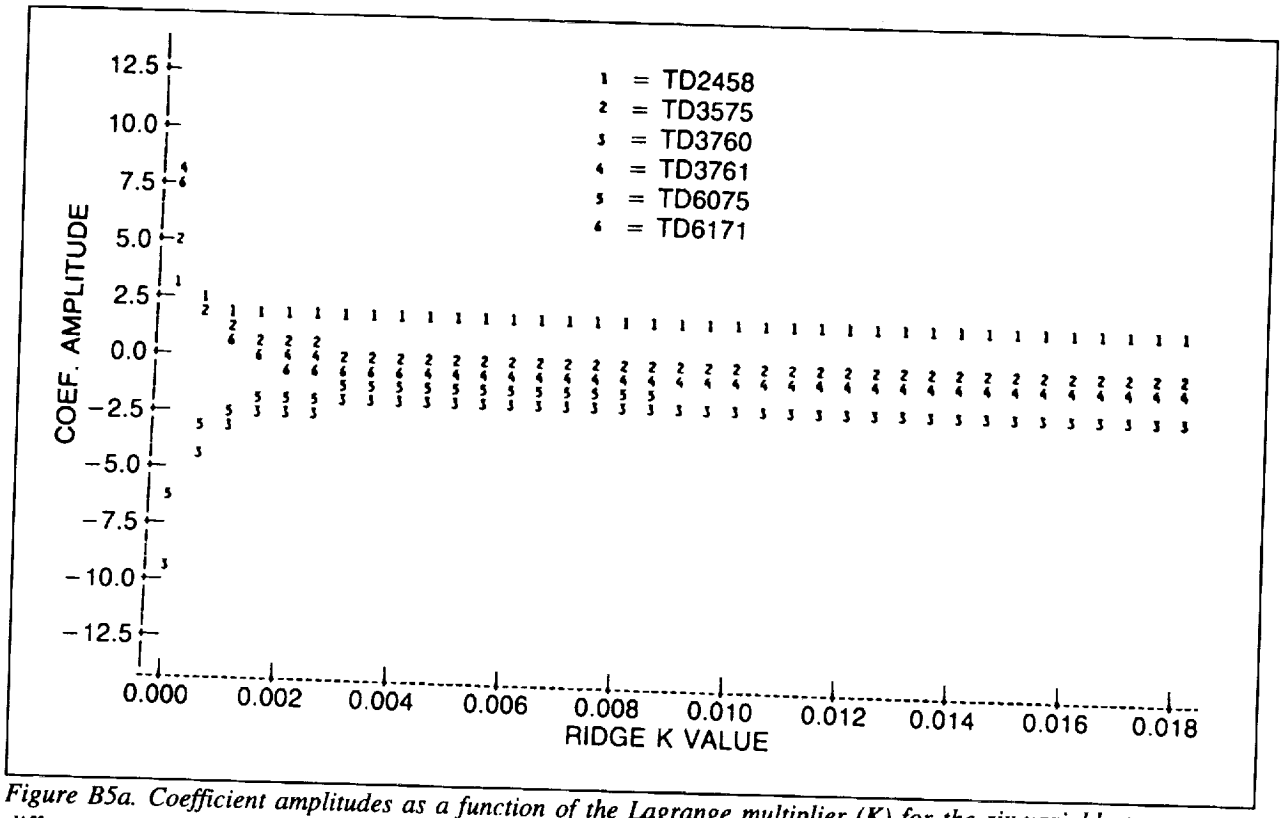

Figure B5a. Coefficient amplitudes as a function of the Lagrange multiplier (K) for the six-variable temperature difference model (see text). Notice the large values of the coefficients for K ~ 0.

Here, the variable K is a Lagrange multiplier. When it is set to zero the solution is that of unconstrained least squares. As K is increased, the parameter estimates (in this case slopes relating temperature differences to the offset bias) become smaller. As K goes to infinity, the estimates all approach zero. In Figure B5a, the 6 temperature difference slope coefficient estimates from the 6th order thermal calibration model (Model B and 6 predictors in Table B3) are plotted as a function of constraint magnitude. Using only a small amount of constraint (K<0.002), the parameter amplitudes rapidly decrease in magnitude, from on the order of 10 to about 2. This is accompanied by only a small increase in the RMS error of the fit. Similar behavior is found in the other higher-order solutions (with 5-8 slope terms). However, for the solutions in the 1-4 variable models (see Figure B5b), little perceptible alteration is found in the relatively stable coefficient estimates out to values of Lagrange multiplier an order of magnitude higher (0.02) than those needed for convergence (0.002) in the higher order models. The important result obtained from the ridge regression is that the consistency check is realized: when a small amount of constraint is applied to the model parameter estimates, the higher-order model solutions converge to the solution produced by the 4-variable model. This is illustrated in Table B8, which presents the predicted globally-averaged thermal offset estimates as a function of AN (mostly day) and DN (mostly night) for each calendar month. With the Lagrange multiplier set to zero, a large (on the order of 5 to 7 W/m^2 discrepancy is evident between the 4 and 6-variable offset predictions for the ascending node. Note that no such error exists for the descending node data as this is the domain over which the models were developed. As K is increased slightly, convergence is obtained not only globally as shown in the table, but also separately at each latitude (i.e., for 4.5° zones).

Table B5. Condition number and set of eigenvalues resulting from the solution of the hierarchy of the temperature difference thermal CAT offset models.

	Number of Terms/Condition Number							
Eigenvalue	1/2	2/2	3/3	4/77	5/239	6/451	7/505	8/1180
1	1.72×10^{0}	1.54×10^{0}	2.21×10^{0}	3.89×10^{0}	4.58×10^{0}	6.21×10^{0}	6.21×10^{0}	7.69×10^{0}
2	2.85×10^{-1}	9.82×10^{-1}	9.86×10^{-1}	7.04×10^{-1}	8.10×10^{-1}	1.03×10^{-1}	1.11×10^{0}	1.25×10^{0}
3		4.83×10^{-1}	5.51×10^{-1}	3.53×10^{-1}	6.09×10^{-1}	6.06×10^{-1}	6.71×10^{-1}	4.55×10^{-2}
4			2.51×10^{-1}	5.74×10^{-2}	3.62×10^{-3}	1.04×10^{-2}	1.05×10^{-2}	1.04×10^{-2}
5				6.60×10^{-4}	6.36×10^{-4}	1.02×10^{-3}	1.21×10^{-3}	1.34×10^{-3}
6					8.04×10^{-5}	7.57×10^{-4}	7.63×10^{-4}	1.02×10^{-3}
7						2.63×10^{-5}	8.87×10^{-5}	2.29×10^{-4}
8							2.43×10^{-5}	4.16×10^{-5}
9								5.53×10^{-6}

Table B6. Error analysis of predicted thermal offsets of temperature-temperature difference models when applied to year 4 (developmental) and year 5 (validation) datasets.

Number of Variables	Year 4			Year 5		
	Explained Variance (%)	RMS Error (W/m^2)	Mean Bias (W/m^2)	Explained Variance (%)	RMS Error (W/m^2)	Mean Bias (W/m^2)
1	72.1	2.45	0.00	70.9	2.67	-0.05
2	87.6	1.64	0.00	87.9	1.72	-0.04
3	89.5	1.50	0.00	89.4	1.62	-0.11
4	90.5	1.43	0.00	90.9	1.49	0.01
5	91.1	1.39	0.01	91.2	1.47	0.15
6	91.2	1.35	0.00	91.0	1.48	0.10
7	91.3	1.37	0.00	91.2	1.47	0.11
8	91.4	1.37	0.00	91.2	1.48	0.19

Representative channel 13 thermal CAT offsets for winter and summer solstices, and an equinox appear in Figure 23 panels a-c, respectively. Note that for all three locations in the seasonal cycle, the thermal CAT offsets exhibit greater amplitude changes near satellite sunset (13 W/m^2) than at satellite sunrise (10 W/m^2). This is primarily due to orbital differences in the shortwave heating response function of the sensor (Section 7.2) which varies by a factor of about 2 from sunrise to sunset. Seasonal changes in the latitudinal dependence of the thermal CAT offsets are largely accounted for by simple north-south shifts in latitudinal position; and by perturbations in the shape of the daytime curve. In particular, the start ($\approx$-2 W/m^2) and end ($\approx$+15 W/m^2) point values of the nighttime curves are nearly constant throughout the year, but they can be seen to drift in latitude, out-of-phase with changes in the solar declination. Relatively large winter-to-summer differences (up to 5 W/m^2) occur in the shape of the daytime bias curves. As might be expected, the curvature of the daytime equinox curve is intermediate to those of winter and summer. Additional discussion of the thermal CAT offsets is given in Section 7.4 where they are also compared to global CAT offsets for the same three situations.

Table B7a. Predicted channel-13 nighttime offsets (W/m^2) for two mid-latitude bands (zonal averages) by month for the eight models

Band #10 (-49.5° to -45.0° latitude)

Number of Terms

Month	1	2	3	4	5	6	7	8
JAN	12.8	7.5	8.8	10.0	9.4	8.8	10.7	9.7
FEB	17.2	16.3	16.6	16.5	16.5	16.6	18.4	16.6
MAR	15.9	14.8	15.0	14.9	14.8	14.8	16.7	14.7
APR	14.9	14.4	14.5	14.3	14.2	14.3	16.3	14.3
MAY	13.7	13.9	13.9	13.7	13.8	13.9	15.9	13.8
JUN	13.6	13.8	13.8	13.1	13.0	13.4	15.4	13.3
JUL	14.1	13.3	13.5	13.3	13.4	13.5	15.5	13.5
AUG	14.6	13.0	13.2	12.9	12.7	12.8	14.8	12.8
SEP	14.8	13.1	13.3	13.1	12.8	12.8	14.8	12.7
OCT	15.6	13.8	13.9	13.3	12.6	12.6	14.6	12.6
NOV	12.8	8.1	9.0	9.8	9.5	9.0	11.1	10.0
DEC	11.3	5.8	7.2	8.1	7.4	6.8	8.8	7.9

Band #30 (40.5° to 45.0° latitude)

Number of Terms

Month	1	2	3	4	5	6	7	8
JAN	8.6	10.3	10.4	10.7	10.6	10.5	12.7	10.5
FEB	8.1	9.5	9.5	9.7	9.9	9.9	11.9	9.9
MAR	5.7	5.4	5.5	5.5	5.3	5.3	7.2	5.1
APR	3.2	1.1	1.2	1.0	0.9	0.9	2.7	0.8
MAY	2.5	-0.5	-0.4	-0.6	-0.9	-0.9	0.9	-0.7
JUN	4.1	0.9	1.0	0.2	-0.3	0.0	1.6	0.0
JUL	3.5	-0.8	-0.6	-0.6	-0.8	-0.8	0.8	-0.7
AUG	3.1	-1.0	-0.7	-0.8	-1.1	-1.2	0.4	-1.4
SEP	3.9	0.9	1.1	1.1	0.7	0.6	2.3	0.1
OCT	5.7	6.2	6.2	6.0	5.5	5.5	7.6	5.4
NOV	6.4	8.0	8.1	8.2	8.1	8.0	10.3	8.1
DEC	7.9	10.1	10.1	10.2	10.0	10.0	12.2	10.1

Table B7b. Predicted channel-13 daytime offsets (W/m^2) for two mid-latitude bands (zonal averages) by month for the eight models								
Band #10 (-49.5° to -45.0° latitude)								
Number of Terms								
Month	1	2	3	4	5	6	7	8
JAN	9.5	5.5	9.3	12.3	5.5	4.3	4.9	2.8
FEB	10.9	7.0	10.6	14.1	7.1	5.8	6.3	4.3
MAR	11.8	7.4	11.1	14.4	7.1	5.9	6.3	4.3
APR	12.4	7.7	11.5	14.2	7.5	6.3	6.8	5.0
MAY	12.2	7.1	10.7	13.0	7.1	6.1	6.7	4.8
JUN	12.2	7.7	11.5	13.1	7.3	6.6	7.2	5.3
JUL	12.7	6.7	10.4	12.7	6.7	5.7	6.3	4.6
AUG	12.4	6.5	10.3	13.1	6.5	5.3	5.9	4.1
SEP	12.1	6.4	10.2	13.2	6.4	5.2	5.7	3.8
OCT	9.5	5.0	8.8	11.2	4.7	3.7	4.5	2.8
NOV	8.3	4.4	8.2	10.8	4.8	3.8	4.7	2.8
DEC	8.2	4.7	8.4	10.6	4.2	3.4	4.2	2.2
Band #30 (40.5° to 45.0° latitude)								
Number of Terms								
Month	1	2	3	4	5	6	7	8
JAN	9.6	8.8	9.0	9.8	8.0	7.9	9.6	7.2
FEB	10.5	9.2	9.4	10.4	8.5	8.4	9.9	7.7
MAR	11.1	8.4	8.8	9.9	7.2	7.0	8.4	6.2
APR	11.7	8.5	9.1	10.2	7.0	6.7	8.0	5.9
MAY	12.4	8.6	9.4	10.8	7.2	6.8	7.9	5.8
JUN	12.2	8.7	9.6	10.6	6.6	6.4	7.5	5.3
JUL	12.5	7.8	8.7	10.2	6.7	6.2	7.3	5.2
AUG	11.9	7.3	8.1	9.3	6.0	5.7	6.9	4.8
SEP	11.5	7.2	7.9	9.1	6.0	5.7	7.0	4.7
OCT	9.6	7.6	8.0	8.1	5.7	5.7	7.4	5.1
NOV	8.6	7.9	8.3	8.5	6.7	6.8	8.6	6.2
DEC	8.8	8.9	9.2	9.1	7.2	7.4	9.2	6.9

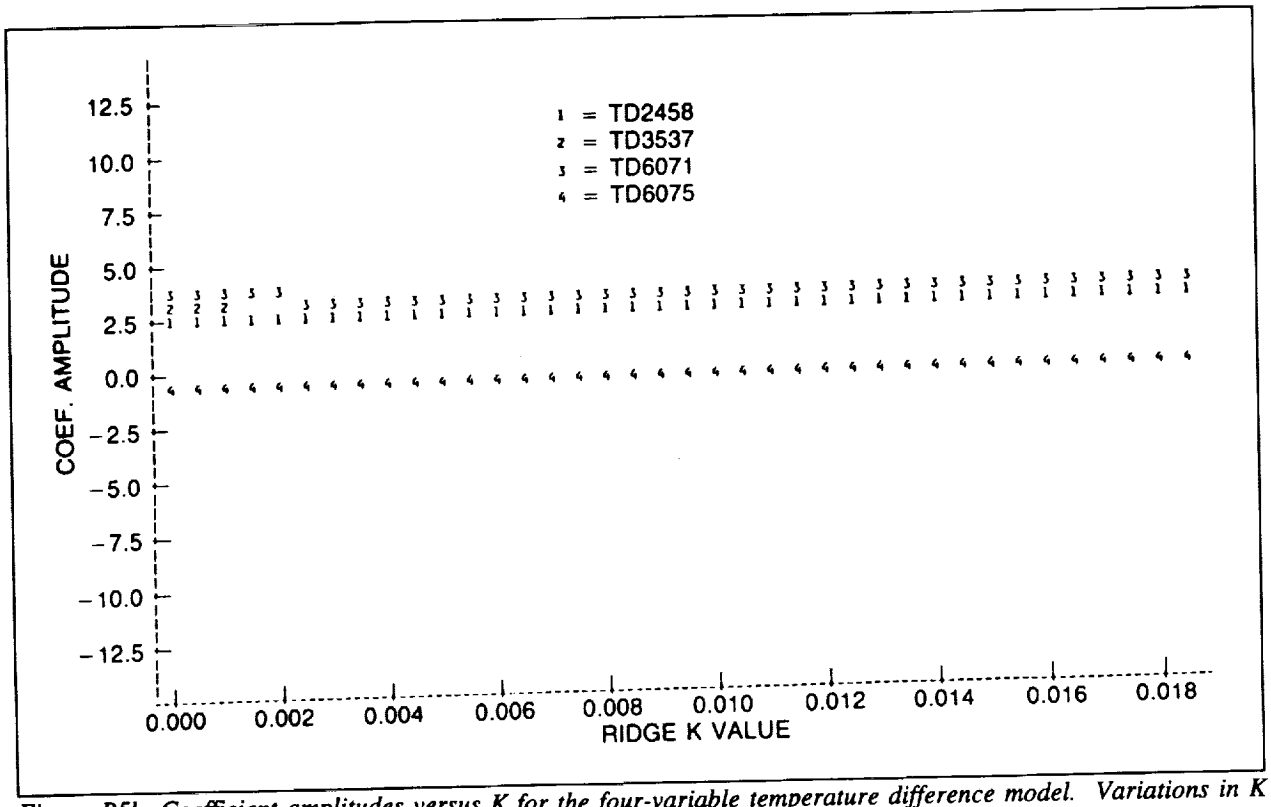

Figure B5b. Coefficient amplitudes versus K for the four-variable temperature difference model. Variations in K have little effect on the coefficients.

Table B8. Convergence of 6-variable model thermal offsets to 4-variable model offsets with the application of small amount of constraint						
	DAY			NIGHT		
N	4	6	6	4	6	6
K	0.000	0.000	0.002	0.000	0.000	0.002
JAN	10.5	5.9	11.9	11.9	11.3	11.8
FEB	12.0	7.2	13.2	12.2	12.2	12.0
MAR	12.3	6.7	13.7	10.5	10.3	10.5
APR	12.9	6.9	14.3	9.5	9.4	9.7
MAY	13.1	7.0	14.5	8.5	8.4	8.8
JUN	13.3	7.1	14.9	8.2	8.2	8.7
JUL	12.6	6.5	13.9	8.3	8.3	8.4
AUG	11.8	5.9	13.2	8.2	7.9	8.4
SEP	11.4	5.8	13.0	8.5	8.0	8.7
OCT	9.7	4.9	11.2	9.1	8.5	9.4
NOV	9.1	5.1	10.5	10.2	9.7	10.1
DEC	9.3	5.2	10.8	11.2	10.6	11.3

APPENDIX C
WFOV CALIBRATION ADJUSTMENT EQUATIONS

The decision was made in 1980 to maintain unchanged the initial post-launch calibration software. Thus, all the Nimbus-7 ERB MAT's have been produced by the same program which for the WFOV sensors utilizes Eq. (1) with unchanged coefficients. This was done for the sake of a continuous basic dataset. Corrections for the various problems described in this paper are applied before the final scientific products are produced. The basic set of scientific products are the corrected irradiances on the Solar and Earth Flux Data Tapes (SEFDT's) and the top of the atmosphere OLR, albedo and net radiation on the ERB MATRIX tapes. For a more complete description of the ERB products, see Kyle, et al. (1985).

C.1 ADJUSTMENT OF THE TOTAL CHANNEL 12

The total channel 12 calibration is assumed to require the application of sensitivity corrections for the shortwave (SW) and longwave (LW) components of the irradiance, an offset that is constant within the orbit, and a "baffle-enhancement" factor. The measurement equation for this channel is thus of the form

$$I_{12}^{u} = \frac{T_{LW}\,(I_{LW} - \text{offset}) + T_{SW}\,I_{SW}}{F_b} \qquad \text{(C1)}$$

T_{LW} = the longwave degradation factor
T_{SW} = the shortwave degradation factor
F_b = the baffle-enhancement factor
I = irradiance values at the satellite
I^u = MAT irradiance (H_T) from Eq.(1)

At night, $I_{SW} = 0$ and the calibration-adjustment equation becomes

$$I_{LW} = \frac{F_b I_{12}^{u}}{T_{LW}} + \text{offset} \qquad \text{(C2)}$$

Arranging (C1) in a manner analogous to (C2) gives

$$\frac{F_b I_{12}^{u}}{T_{LW}} + \text{offset} = I_{LW} + \frac{T_{SW}}{T_{LW}} I_{SW} \qquad \text{(C3)}$$

Adding the quantity I_{SW} to each side and rearranging gives

$$I_{LW} + I_{SW} = \frac{F_b I_{12}^u}{T_{LW}} + \left(1 - \frac{T_{SW}}{T_{LW}}\right) I_{SW} + \text{offset} \qquad \text{(C4)}$$

Recognizing that $I_{12} = I_{LW} + I_{SW}$ and that $I_{SW} = I_{13}$, the "correction" equation for this channel is simply

$$I_{12} = F_b A I_{12}^u + B I_{13} + \text{offset} \qquad \text{(C5)}$$

Here A is $1/T_{LW}$ and B is $1 - T_{SW}/T_{LW}$. The value of F_b is 0.963 and is the same as in Kyle, et al. (1984), but the offset has been recalculated and is now 12.6 W/m^2. It is determined so that the average channel 12 and scanner longwave fluxes will be the same at the top of the atmosphere. The calibration of the longwave scanner channels was recently revised (Kyle, et al., 1985, 1990b) and this has been taken into account in determining the new value. Notice that evaluation of Eq.(C5) requires knowledge of the satellite altitude shortwave irradiance (I_{13}) so recalibration of channel 13 must be completed prior to implementation of this equation. This is also indicated in panel e of Figure 10 which summarizes the sequence of global CAT processing procedures.

C.2 THE CHANNEL 13 CALIBRATION ADJUSTMENT SLOPE

It is assumed that both a sensitivity correction and an orbitally-varying offset are required to adjust the calibration of the shortwave channel 13. The measurement equation for this channel, with these assumptions, is

$$I_{13}^u = T_{13} I_{SW} - \text{offset} \qquad \text{(C6)}$$

where, as before, I_{SW} is the actual shortwave irradiance at satellite altitude, I_{13}^u is the prelaunch calibration MAT irradiance, and $1/T_{13}$ is the irradiance degradation correction factor. Shifting the offset of (C6) to the left hand side of the equation, an attenuated shortwave irradiance, $I_{SW,atten}$, is defined by

$$I_{SW,atten} = I_{13}^u + \text{offset} = T_{13} I_{SW} \qquad \text{(C7)}$$

that represents the decrease in satellite altitude irradiance due to the channel sensitivity loss alone. That is, the thermal perturbations and direct solar radiation that influence the values of the channel readings have been removed from the MAT irradiances via addition of the calibration offsets.

Derivation of T_{13} or $1/T_{13}$ is based on estimates of $I_{SW,atten}$, obtained by application of the climatological thermal CAT (see Section 5.3 and 7.4) to the channel 13 MAT irradiances, and approximate recalibration data for channel 12. Estimates of corrected channel 12 irradiances are derived by application of the baffle enhancement factor F_b and channel 12 offset as specified in (C5). The simplifying assumption that T_{LW} equals T_{SW} eliminates the dependence of the computed irradiance on I_{SW}, a quantity that is not available at this stage of the calibration. Channel 12 MAT irradiances recalibrated in this way are indicated by the variable $I_{12,approx1}$.

The AN - DN difference of approximate half-monthly, global-averaged, global CAT channel 12 irradiances may be partitioned into longwave and shortwave components in the form

$$(I_{12}^{an} - I_{12}^{dn})_{approx1} \approx I_{SW}^{an} - I_{SW}^{dn} + I_{LW}^{an} - I_{LW}^{dn} \tag{C8}$$

A similar difference for the thermal CAT-derived, attenuated channel 13 irradiances is

$$(I_{13}^{an} - I_{13}^{dn})_{atten} \approx T_{13} (I_{SW}^{an} - I_{SW}^{dn}) \tag{C9}$$

The ratio of (C8) and (C9) can be taken to give

$$\frac{(I_{12}^{an} - I_{12}^{dn})_{approx1}}{(I_{13}^{an} - I_{13}^{dn})_{atten}} \approx \frac{1}{T_{13}} \left(\frac{I_{SW}^{an} - I_{SW}^{dn}}{I_{SW}^{an} - I_{SW}^{dn}} + \frac{I_{LW}^{an} - I_{LW}^{dn}}{I_{SW}^{an} - I_{SW}^{dn}} \right) \tag{C10}$$

When C10 is rearranged, an expression for the degradation correction factor $1/T_{13}$ in terms of half-monthly globally-averaged irradiances is

$$\frac{1}{T_{13}} \approx \frac{(I_{12}^{an} - I_{12}^{dn})_{approx1}}{(I_{13}^{an} - I_{13}^{dn})_{atten}} /(1 + K) \tag{C11}$$

Here the constant K is the ratio

$$K = \frac{I_{LW}^{an} - I_{LW}^{dn}}{I_{SW}^{an} - I_{SW}^{dn}} \tag{C12}$$

and is assumed to be seasonally invariant with a value of 0.0193. The numerator, $I_{LW}^{an} - I_{LW}^{dn}$, was evaluated from the longwave scanner data while the denominator was estimated from channel 13 itself. The assumption that K is a constant is consistent with the observed small variation in K and the other approximations in the calibration algorithm. The global CAT degradation correction factors are obtained from the data of (C11) by fitting the time series of half-monthly correction factors with a low order polynomial curve. Although continuous changes in correction factors are then possible, only one value is used for each half-monthly period.

C.3 THE CHANNEL 13 CALIBRATION ADJUSTMENT OFFSET

Once the degradation for channel 13 has been obtained (essentially a sensitivity adjustment to account for transmissivity loss of the filter domes), only an offset is required to estimate the irradiance from (C6). From the standpoint of an operational algorithm, it is preferable to rewrite (C6) in the form

$$I_{SW} = A_{13} I_{13}^{u} + b_{13} \tag{C13}$$

where $A_{13} = 1/T_{13}$ is the slope and $b_{13} = \text{offset}/T_{13}$ is the offset that transform MAT irradiances to measurements of shortwave flux. The term "offset" consists of five components that together account for solar, terrestrial, and thermal perturbations in the MAT irradiances. They are the midnight offset (O_{mid}), shortwave heating (O_{SW}), longwave heating (O_{LW}), sunblip clipping (O_{cl}), and the daytime offset (O_{day}). The first four of these terms are derived directly from MAT data during DELMAT processing. As a computational expediency, therefore, we rewrite the calibration equation in terms of DELMAT data as

$$I_{SW} = A_{13} I_{13,DELMAT} + B_{13} \tag{C14}$$

where $I_{13,DELMAT}$ is given by

$$I_{13,DELMAT} = I_{13}^{u} + O_{mid} + O_{SW} + O_{LW} + O_{cl} \tag{C15}$$

and $B_{13} = O_{day}/T_{13}$ is the offset redefined for application to DELMAT data. A solution for B_{13} is obtained (in terms of half-monthly global averages) from (C14) by taking AN - DN differences (Δ), expressing I_{SW} as $I_{SW} = I_{total} - I_{LW}$, and recognizing the $B_{13} \approx 0$ on DN. We obtain

$$B_{13} = \left(\frac{\Delta I_{total}}{\Delta I_{13,DELMAT}} - \frac{\Delta I_{LW}}{\Delta I_{13,DELMAT}} - A_{13} \right) \Delta I_{13,DELMAT} \tag{C16}$$

The term ΔI_{total} is evaluated based on channel 12 data using (C5) but with DELMAT irradiances used to approximate the yet undetermined I_{13}. This estimate, $I_{13,approx}$, is computed as

$$I_{13,approx} = \frac{1}{T_{13}} \cdot I_{13,DELMAT} \approx I_{13} \tag{C17}$$

Notice from Figure 10c that DELMAT data contain all offset corrections except O_{day}. Using this estimate of I_{13} in (C5), we obtain approximate values for ΔI_{total} which we refer to as $I_{12,approx2}$. Notice too that the second term on the right-hand side of (C16) can be expressed as

$$\frac{\Delta I_{LW}}{\Delta I_{13,DELMAT}} \approx K \cdot \frac{\Delta I_{12,approx2}}{\Delta I_{13,DELMAT}} \tag{C18}$$

where K is given in (C12). Thus B_{13} is approximately given by

$$B_{13} \approx \left((\frac{\Delta I_{12,approx2}}{\Delta I_{13,DELMAT}})/(1+K) - A_{13} \right) \Delta I_{13,DELMAT} \tag{C19}$$

C.4 CHANNEL 14 CALIBRATION ADJUSTMENTS

The near infrared (NIR), 0.7 to 2.8 μm, values are derived from channel 14 in a manner analogous to the channel 13 adjustment algorithm, but with minor variations. The measurement equation is assumed to have the form

$$I_{14}^{u} = T_{14}\, I_{NIR} - \text{offset} \tag{C20}$$

where $1/T_{14}$ is the degradation correction factor for channel 14. As with channel 13, we rewrite (C20) in the form

$$I_{NIR} = A_{14} I_{14,DELMAT} + B_{14} \tag{C21}$$

where $B_{14} = 0_{day}/T_{14}$ is the offset for application to DELMAT data. Taking AN - DN differences of (C21) and noting that B_{14} is essentially zero on DN, we obtain

$$B_{14} = \left(\frac{\Delta I_{NIR}}{\Delta I_{14,DELMAT}} - A_{14} \right) \Delta I_{14,DELMAT} \tag{C22}$$

To evaluate (C22), we first express ΔI_{NIR} as

$$\Delta I_{NIR} = \frac{\Delta I_{SW}}{f} \tag{C23}$$

where f is a constant of value 2.2712 and (1/f) is the mean fraction of near infrared (0.7 to 2.8 μm) Earth-reflected solar irradiance in the shortwave spectral interval (0.2 to 3.8 μm). From the first year of measurements, solar constants of 1371.5 W/m^2 (0.2 to 3.8 μm) and 690 W/m^2 (0.7 to 2.8 μm) were determined in 1980. It was also found that the (0.7 to 2.8 μm) albedo was about 0.875 times the (0.2 to 3.8 μm) albedo. These numbers were used to calculated f. Substituting (C23) in (C22) and subsequently

following the development used for channel 13, B_{14} is approximately given in terms of DELMAT data and channel 12 irradiances as

$$B_{14} \approx \left(\frac{\Delta I_{12,approx2}/f}{\Delta I_{14,DELMAT}} \right) /(1+K) \; - \; A_{14} \Delta I_{14,DELMAT} \qquad \text{(C24)}$$

C.5 THE GLOBAL CALIBRATION ADJUSTMENT TABLE

Table C1 is a listing of the global CAT coefficients that complement the DELMAT corrections through 9 years of the experiment. Mean calibration slope(s) and offset for each of the channels are given by year and half-monthly calibration period. The slopes for channel 12 are the terms A ($1/T_{LW}$) and B ($1-T_{SW}/T_{LW}$) of (C5); the offset is indicated by the variable of the same name (i.e. "offset"). For channels 13 and 14, slopes are the terms A ($1/T_{13}$ and $1/T_{14}$, respectively) in (C15) and (C21) and offsets are the B variables. The results of asymmetric degradation in the channel 13 (the asymmetric slopes) are also given for six 30° solar zenith angle ranges from -90° to +90°.

Table C1. Half-Monthly Global Calibration Adjustment Table

Year-1													
	Channel 13 Asymmetric Slopes						Channel 12, 13, and 14 Mean Slope and Offsets						
	Solar Zenith Angle Range						Ch 13		Ch 12			Ch 14	
Half Month	-90 to -60	-60 to -30	-30 to 0	0 to 30	30 to 60	60 to 90	A Slope	B Offset	A Slope	B Slope	Offset	A Slope	B Offset
Nov 16-30 1978	1.0073	1.0046	1.0039	1.0039	1.0038	1.0007	1.0039	-1.2	1.0039	-0.0036	12.6	1.0000	-0.2
Dec 1-15 1978	1.0109	1.0068	1.0059	1.0059	1.0057	1.0011	1.0059	-1.8	1.0060	-0.0056	12.6	1.0006	-0.5
Dec 16-31 1978	1.0145	1.0090	1.0079	1.0079	1.0075	1.0014	1.0079	-1.0	1.0081	-0.0076	12.6	1.0012	-0.3
Jan 1-15 1979	1.0181	1.0112	1.0099	1.0099	1.0093	1.0017	1.0099	-0.8	1.0102	-0.0097	12.6	1.0018	0.0
Jan 16-31 1979	1.0217	1.0134	1.0119	1.0199	1.0111	1.0020	1.0119	0.2	1.0123	-0.0117	12.6	1.0024	0.8
Feb 1-15 1979	1.0253	1.0156	1.0139	1.0139	1.0129	1.0023	1.0139	0.4	1.0144	-0.0137	12.6	1.0029	1.0
Feb 16-28 1979	1.0289	1.0178	1.0159	1.0159	1.0147	1.0026	1.0159	-0.1	1.0165	-0.0156	12.6	1.0035	1.3
Mar 1-15 1979	1.0325	1.0200	1.0179	1.0179	1.0165	1.0029	1.0179	-1.4	1.0186	-0.0176	12.6	1.0041	0.8
Mar 16-31 1979	1.0334	1.0209	1.0188	1.0188	1.0174	1.0038	1.0188	-0.7	1.0187	-0.0176	12.6	1.0047	1.5
Apr 1-15 1979	1.0331	1.0206	1.0216	1.0206	1.0195	1.0035	1.0196	1.0	1.0188	-0.0176	12.6	1.0052	1.7
Apr 16-30 1979	1.0340	1.0215	1.0225	1.0215	1.0204	1.0044	1.0205	2.1	1.0189	-0.0177	12.6	1.0058	2.3
May 1-15 1979	1.0352	1.0212	1.0242	1.0231	1.0221	1.0056	1.0213	3.2	1.0190	-0.0177	12.6	1.0064	2.4
May 16-31 1979	1.0360	1.0220	1.0250	1.0239	1.0229	1.0064	1.0221	4.8	1.0192	-0.0178	12.6	1.0069	3.3
Jun 1-15 1979	1.0367	1.0230	1.0260	1.0248	1.0231	1.0081	1.0230	5.6	1.0193	-0.0178	12.6	1.0075	3.2
Jun 16-30 1979	1.0375	1.0238	1.0268	1.0256	1.0239	1.0089	1.0238	5.2	1.0194	-0.0178	12.6	1.0080	3.1
Jul 1-15 1979	1.0377	1.0247	1.0277	1.0258	1.0246	1.0099	1.0247	5.3	1.0195	-0.0177	12.6	1.0086	3.0
Jul 16-31 1979	1.0385	1.0255	1.0285	1.0266	1.0254	1.0107	1.0255	5.0	1.0196	-0.0177	12.6	1.0091	2.7
Aug 1-15 1979	1.0393	1.0264	1.0294	1.0274	1.0254	1.0125	1.0264	4.6	1.0197	-0.0177	12.6	1.0097	2.2
Aug 16-31 1979	1.0401	1.0272	1.0302	1.0282	1.0262	1.0133	1.0272	3.9	1.0198	-0.0177	12.6	1.0102	2.1
Sep 1-15 1979	1.0425	1.0271	1.0290	1.0290	1.0271	1.0141	1.0281	3.4	1.0199	-0.0177	12.6	1.0107	1.7
Sep 16-30 1979	1.0433	1.0279	1.0298	1.0298	1.0279	1.0149	1.0289	3.0	1.0201	-0.0178	12.6	1.0113	1.5
Oct 1-15 1979	1.0459	1.0288	1.0288	1.0298	1.0278	1.0169	1.0298	1.7	1.0202	-0.0178	12.6	1.0118	0.9
Oct 16-31 1979	1.0467	1.0296	1.0296	1.0306	1.0286	1.0177	1.0306	0.4	1.0203	-0.0178	12.6	1.0123	0.4

Year-2													
	Channel 13 Asymmetric Slopes						Channel 12, 13, and 14 Mean Slope and Offsets						
	Solar Zenith Angle Range						Ch 13		Ch 12			Ch 14	
Half Month	-90 to -60	-60 to -30	-30 to 0	0 to 30	30 to 60	60 to 90	Mean	Ch 13 Offset	LW	SW	Ch 12 Offset	Ch 14 Slope	Ch 14 Offset
Nov 1-15 1979	1.0485	1.0295	1.0285	1.0315	1.0295	1.0185	1.0315	-1.1	1.0204	-0.0178	12.6	1.0128	-0.2
Nov 16-30 1979	1.0493	1.0303	1.0293	1.0323	1.0303	1.0193	1.0323	-2.2	1.0205	-0.0178	12.6	1.0133	-0.4
Dec 1-15 1979	1.0490	1.0322	1.0311	1.0332	1.0311	1.0189	1.0332	-2.9	1.0206	-0.0177	12.6	1.0138	-0.7
Dec 16-31 1979	1.0499	1.0331	1.0320	1.0341	1.0320	1.0198	1.0341	-3.5	1.0207	-0.0177	12.6	1.0143	-0.7
Jan 1-15 1980	1.0506	1.0359	1.0328	1.0349	1.0328	1.0206	1.0349	-3.3	1.0208	-0.0177	12.6	1.0149	-0.8
Jan 16-31 1980	1.0515	1.0368	1.0337	1.0358	1.0337	1.0215	1.0358	-3.3	1.0209	-0.0177	12.6	1.0154	-0.5
Feb 1-15 1980	1.0514	1.0388	1.0357	1.0367	1.0346	1.0214	1.0367	-1.8	1.0210	-0.0177	12.6	1.0158	0.3
Feb 16-28 1980	1.0522	1.0396	1.0365	1.0375	1.0354	1.0221	1.0375	-0.8	1.0211	-0.0177	12.6	1.0163	1.0
Mar 1-15 1980	1.0532	1.0406	1.0384	1.0384	1.0369	1.0231	1.0384	0.4	1.0212	-0.0177	12.6	1.0168	1.4
Mar 16-31 1980	1.0541	1.0414	1.0392	1.0392	1.0377	1.0239	1.0392	1.4	1.0213	-0.0177	12.6	1.0173	2.0
Apr 1-15 1980	1.0538	1.0411	1.0422	1.0411	1.0400	1.0237	1.0401	2.7	1.0214	-0.0177	12.6	1.0178	2.6
Apr 16-30 1980	1.0546	1.0419	1.0430	1.0419	1.0408	1.0245	1.0409	2.7	1.0215	-0.0177	12.6	1.0183	2.0
May 1-15 1980	1.0559	1.0416	1.0446	1.0436	1.0425	1.0257	1.0417	3.9	1.0216	-0.0178	12.6	1.0188	2.5
May 16-31 1980	1.0567	1.0424	1.0454	1.0444	1.0433	1.0264	1.0425	4.0	1.0216	-0.0177	12.6	1.0192	2.4
Jun 1-15 1980	1.0574	1.0434	1.0464	1.0453	1.0435	1.0282	1.0434	4.6	1.0217	-0.0177	12.6	1.0197	2.5
Jun 16-30 1980	1.0582	1.0442	1.0472	1.0461	1.0443	1.0290	1.0442	4.4	1.0218	-0.0177	12.6	1.0202	2.3
Jul 1-15 1980	1.0583	1.0450	1.0480	1.0461	1.0449	1.0300	1.0450	5.5	1.0219	-0.0177	12.6	1.0206	2.6
Jul 16-31 1980	1.0591	1.0458	1.0488	1.0469	1.0457	1.0307	1.0458	5.2	1.0220	-0.0177	12.6	1.0211	2.6
Aug 1-15 1980	1.0598	1.0466	1.0496	1.0476	1.0456	1.0325	1.0466	5.0	1.0221	-0.0177	12.6	1.0215	2.6
Aug 16-31 1980	1.0606	1.0474	1.0504	1.0484	1.0464	1.0333	1.0474	3.6	1.0222	-0.0178	12.6	1.0220	1.7
Sep 1-15 1980	1.0629	1.0472	1.0491	1.0491	1.0472	1.0339	1.0482	2.8	1.0223	-0.0178	12.6	1.0224	1.3
Sep 16-30 1980	1.0637	1.0480	1.0499	1.0499	1.0480	1.0347	1.0490	1.6	1.0223	-0.0177	12.6	1.0229	0.9
Oct 1-15 1980	1.0662	1.0487	1.0487	1.0498	1.0478	1.0367	1.0498	0.4	1.0224	-0.0177	12.6	1.0233	0.4
Oct 16-31 1980	1.0670	1.0495	1.0495	1.0506	1.0486	1.0375	1.0506	-0.6	1.0225	-0.0177	12.6	1.0237	-0.1

Year-3													
	Channel 13 Asymmetric Slopes						Channel 12, 13, and 14 Mean Slope and Offsets						
	Solar Zenith Angle Range						Ch 13		Ch 12			Ch 14	
Half Month	-90 to -60	-60 to -30	-30 to 0	0 to 30	30 to 60	60 to 90	Mean	Ch 13 Offset	LW	SW	Ch 12 Offset	Ch 14 Slope	Ch 14 Offset
Nov 1-15 1980	1.0687	1.0494	1.0484	1.0514	1.0494	1.0382	1.0514	-1.4	1.0226	-0.0178	12.6	1.0242	-0.4
Nov 16-30 1980	1.0696	1.0502	1.0491	1.0522	1.0502	1.0389	1.0522	-1.5	1.0227	-0.0178	12.6	1.0246	-0.4
Dec 1-15 1980	1.0691	1.0519	1.0509	1.0530	1.0509	1.0385	1.0530	-1.9	1.0227	-0.0177	12.6	1.0250	-0.7
Dec 16-31 1980	1.0698	1.0526	1.0516	1.0537	1.0516	1.0392	1.0537	-2.7	1.0228	-0.0177	12.6	1.0254	-0.7
Jan 1-15 1981	1.0705	1.0556	1.0524	1.0545	1.0524	1.0399	1.0545	-2.9	1.0229	-0.0178	12.6	1.0259	-0.7
Jan 16-31 1981	1.0713	1.0564	1.0532	1.0553	1.0532	1.0407	1.0553	-3.3	1.0230	-0.0178	12.6	1.0263	-0.8
Feb 1-15 1981	1.0710	1.0581	1.0549	1.0560	1.0539	1.0404	1.0560	-2.8	1.0230	-0.0177	12.6	1.0267	-0.6
Feb 16-28 1981	1.0718	1.0589	1.0557	1.0568	1.0547	1.0412	1.0568	-1.6	1.0231	-0.0178	12.6	1.0271	0.1
Mar 1-15 1981	1.0726	1.0597	1.0575	1.0575	1.0560	1.0420	1.0575	-1.1	1.0232	-0.0178	12.6	1.0275	0.4
Mar 16-31 1981	1.0735	1.0606	1.0584	1.0584	1.0569	1.0428	1.0584	0.6	1.0232	-0.0178	12.6	1.0279	1.5
Apr 1-15 1981	1.0731	1.0602	1.0612	1.0602	1.0590	1.0424	1.0591	1.3	1.0233	-0.0178	12.6	1.0283	1.4
Apr 16-30 1981	1.0739	1.0610	1.0620	1.0610	1.0598	1.0432	1.0599	2.2	1.0234	-0.0178	12.6	1.0287	2.1
May 1-15 1981	1.0750	1.0605	1.0636	1.0625	1.0614	1.0443	1.0606	3.0	1.0234	-0.0177	12.6	1.0291	2.2
May 16-31 1981	1.0757	1.0612	1.0643	1.0632	1.0621	1.0450	1.0613	3.0	1.0235	-0.0178	12.6	1.0295	2.0
Jun 1-15 1981	1.0763	1.0621	1.0652	1.0640	1.0622	1.0466	1.0621	2.6	1.0236	-0.0178	12.6	1.0298	1.7
Jun 16-30 1981	1.0770	1.0628	1.0659	1.0647	1.0629	1.0473	1.0628	3.2	1.0236	-0.0177	12.6	1.0302	1.8
Jul 1-15 1981	1.0770	1.0635	1.0666	1.0647	1.0634	1.0482	1.0635	3.3	1.0237	-0.0178	12.6	1.0306	1.9
Jul 16-31 1981	1.0777	1.0642	1.0673	1.0654	1.0641	1.0489	1.0642	3.5	1.0238	-0.0178	12.6	1.0310	1.7
Aug 1-15 1981	1.0783	1.0649	1.0680	1.0660	1.0638	1.0505	1.0649	3.9	1.0238	-0.0178	12.6	1.0313	1.8
Aug 16-31 1981	1.0790	1.0656	1.0687	1.0667	1.0645	1.0512	1.0656	3.5	1.0239	-0.0178	12.6	1.0317	1.9
Sep 1-15 1981	1.0812	1.0652	1.0673	1.0673	1.0652	1.0518	1.0663	2.8	1.0239	-0.0178	12.6	1.0321	1.6
Sep 16-30 1981	1.0818	1.0658	1.0679	1.0679	1.0658	1.0524	1.0669	1.3	1.0240	-0.0178	12.6	1.0324	0.8
Oct 1-15 1981	1.0842	1.0664	1.0664	1.0675	1.0655	1.0542	1.0675	-0.5	1.0241	-0.0178	12.6	1.0328	0.2
Oct 16-31 1981	1.0848	1.0670	1.0670	1.0681	1.0661	1.0547	1.0681	-2.4	1.0241	-0.0178	12.6	1.0331	-0.8

Year-4													
	Channel 13 Asymmetric Slopes						Channel 12, 13, and 14 Mean Slope and Offsets						
	Solar Zenith Angle Range						Ch 13		Ch 12			Ch 14	
Half Month	-90 to -60	-60 to -30	-30 to 0	0 to 30	30 to 60	60 to 90	Mean	Ch 13 Offset	LW	SW	Ch 12 Offset	Ch 14 Slope	Ch 14 Offset
Nov 1-15 1981	1.0863	1.0667	1.0656	1.0687	1.0667	1.0552	1.0687	-3.5	1.0242	-0.0178	12.6	1.0333	-1.3
Nov 16-30 1981	1.0869	1.0673	1.0662	1.0693	1.0673	1.0558	1.0693	-3.9	1.0242	-0.0178	12.6	1.0335	-1.3
Dec 1-15 1981	1.0862	1.0687	1.0677	1.0698	1.0677	1.0550	1.0698	-4.0	1.0243	-0.0178	12.6	1.0337	-1.4
Dec 16-31 1981	1.0868	1.0693	1.0683	1.0704	1.0683	1.0556	1.0704	-3.7	1.0243	-0.0178	12.6	1.0339	-1.2
Jan 1-15 1982	1.0873	1.0721	1.0689	1.0710	1.0689	1.0562	1.0710	-3.6	1.0244	-0.0178	12.6	1.0341	-0.7
Jan 16-31 1982	1.0879	1.0727	1.0695	1.0716	1.0695	1.0568	1.0716	-3.3	1.0244	-0.0178	12.6	1.0343	-0.5
Feb 1-15 1982	1.0874	1.0743	1.0711	1.0722	1.0701	1.0563	1.0722	-3.0	1.0245	-0.0179	12.6	1.0345	-0.1
Feb 16-28 1982	1.0880	1.0749	1.0717	1.0728	1.0707	1.0569	1.0728	-2.8	1.0245	-0.0178	12.6	1.0348	0.0
Mar 1-15 1982	1.0886	1.0756	1.0733	1.0733	1.0718	1.0575	1.0733	-2.8	1.0245	-0.0178	12.6	1.0350	-0.2
Mar 16-31 1982	1.0893	1.0762	1.0739	1.0739	1.0724	1.0581	1.0739	-1.7	1.0246	-0.0178	12.6	1.0352	0.6
Apr 1-15 1982	1.0887	1.0756	1.0766	1.0756	1.0744	1.0575	1.0745	-0.2	1.0246	-0.0178	12.6	1.0354	1.1
Apr 16-30 1982	1.0893	1.0762	1.0772	1.0762	1.0750	1.0581	1.0751	1.6	1.0247	-0.0178	12.6	1.0356	1.8
May 1-15 1982	1.0903	1.0756	1.0787	1.0776	1.0766	1.0591	1.0757	2.9	1.0247	-0.0178	12.6	1.0358	2.3
May 16-31 1982	1.0909	1.0762	1.0793	1.0782	1.0772	1.0597	1.0763	3.7	1.0247	-0.0178	12.6	1.0360	2.3
Jun 1-15 1982	1.0912	1.0768	1.0799	1.0787	1.0769	1.0611	1.0768	3.8	1.0248	-0.0178	12.6	1.0362	2.2
Jun 16-30 1982	1.0918	1.0774	1.0805	1.0793	1.0775	1.0617	1.0774	3.5	1.0248	-0.0178	12.6	1.0365	1.9
Jul 1-15 1982	1.0917	1.0780	1.0811	1.0792	1.0779	1.0625	1.0780	3.6	1.0249	-0.0179	12.6	1.0367	1.9
Jul 16-31 1982	1.0923	1.0786	1.0817	1.0798	1.0785	1.0631	1.0786	3.1	1.0249	-0.0178	12.6	1.0369	1.7
Aug 1-15 1982	1.0928	1.0792	1.0823	1.0803	1.0781	1.0646	1.0792	2.4	1.0249	-0.0178	12.6	1.0371	1.1
Aug 16-31 1982	1.0934	1.0798	1.0829	1.0809	1.0787	1.0652	1.0798	2.4	1.0250	-0.0179	12.6	1.0373	1.2
Sep 1-15 1982	1.0954	1.0792	1.0813	1.0813	1.0792	1.0656	1.0803	2.2	1.0250	-0.0178	12.6	1.0375	1.3
Sep 16-30 1982	1.0960	1.0798	1.0819	1.0819	1.0798	1.0662	1.0809	1.1	1.0250	-0.0178	12.6	1.0377	1.2
Oct 1-15 1982	1.0984	1.0804	1.0804	1.0815	1.0794	1.0680	1.0815	0.0	1.0250	-0.0178	12.6	1.0379	0.7
Oct 16-31 1982	1.0990	1.0810	1.0810	1.0821	1.0800	1.0686	1.0821	-1.3	1.0251	-0.0179	12.6	1.0381	-0.1

Year-5														
	Channel 13 Asymmetric Slopes						Channel 12, 13, and 14 Mean Slope and Offsets							
	Solar Zenith Angle Range						Ch 13		Ch 12			Ch 14		
Half Month	-90 to -60	-60 to -30	-30 to 0	0 to 30	30 to 60	60 to 90	Mean	Ch 13 Offset	LW	SW	Ch 12 Offset	Ch 14 Slope	Ch 14 Offset	
Nov 1-15 1982	1.1006	1.0806	1.0796	1.0827	1.0806	1.0691	1.0827	-2.6	1.0251	-0.0178	12.6	1.0383	-0.8	
Nov 16-30 1982	1.1012	1.0812	1.0802	1.0833	1.0812	1.0696	1.0833	-3.9	1.0251	-0.0178	12.6	1.0385	-1.0	
Dec 1-15 1982	1.1004	1.0827	1.0816	1.0838	1.0816	1.0688	1.0838	-5.0	1.0252	-0.0179	12.6	1.0387	-1.6	
Dec 16-31 1982	1.1010	1.0833	1.0822	1.0844	1.0822	1.0694	1.0844	-5.2	1.0252	-0.0179	12.6	1.0389	-1.4	
Jan 1-15 1983	1.1015	1.0861	1.0828	1.0850	1.0828	1.0700	1.0850	-5.0	1.0252	-0.0178	12.6	1.0391	-1.4	
Jan 16-31 1983	1.1021	1.0867	1.0834	1.0856	1.0834	1.0706	1.0856	-3.4	1.0252	-0.0178	12.6	1.0393	-0.5	
Feb 1-15 1983	1.1016	1.0884	1.0851	1.0862	1.0840	1.0701	1.0862	-2.8	1.0252	-0.0178	12.6	1.0395	-0.1	
Feb 16-28 1983	1.1022	1.0890	1.0857	1.0868	1.0846	1.0707	1.0868	-1.3	1.0253	-0.0179	12.6	1.0398	0.2	
Mar 1-15 1983	1.1028	1.0896	1.0873	1.0873	1.0858	1.0713	1.0873	-0.6	1.0253	-0.0179	12.6	1.0400	0.9	
Mar 16-31 1983	1.1035	1.0902	1.0879	1.0879	1.0864	1.0719	1.0879	-0.5	1.0253	-0.0178	12.6	1.0402	1.2	
Apr 1-15 1983	1.1029	1.0896	1.0907	1.0896	1.0884	1.0713	1.0885	0.1	1.0253	-0.0178	12.6	1.0404	1.5	
Apr 16-30 1983	1.1035	1.0902	1.0913	1.0902	1.0890	1.0719	1.0891	1.4	1.0253	-0.0178	12.6	1.0406	1.7	
May 1-15 1983	1.1045	1.0896	1.0928	1.0917	1.0906	1.0729	1.0897	2.6	1.0253	-0.0178	12.6	1.0408	2.1	
May 16-31 1983	1.1050	1.0901	1.0933	1.0922	1.0911	1.0734	1.0902	3.2	1.0254	-0.0179	12.6	1.0410	2.1	
Jun 1-15 1983	1.1054	1.0908	1.0940	1.0928	1.0909	1.0749	1.0908	4.3	1.0254	-0.0179	12.6	1.0412	2.5	
Jun 16-30 1983	1.1060	1.0914	1.0946	1.0934	1.0915	1.0755	1.0914	3.5	1.0254	-0.0179	12.6	1.0415	2.1	
Jul 1-15 1983	1.1059	1.0920	1.0952	1.0932	1.0919	1.0763	1.0920	5.0	1.0254	-0.0179	12.6	1.0417	2.4	
Jul 16-31 1983	1.1065	1.0926	1.0958	1.0938	1.0925	1.0769	1.0926	4.3	1.0254	-0.0179	12.6	1.0419	2.1	
Aug 1-15 1983	1.1070	1.0932	1.0964	1.0943	1.0921	1.0784	1.0932	3.9	1.0254	-0.0178	12.6	1.0421	1.9	
Aug 16-31 1983	1.1076	1.0938	1.0970	1.0949	1.0927	1.0790	1.0938	3.5	1.0254	-0.0178	12.6	1.0423	1.8	
Sep 1-15 1983	1.1096	1.0932	1.0953	1.0953	1.0932	1.0794	1.0943	1.5	1.0254	-0.0178	12.6	1.0425	1.1	
Sep 16-30 1983	1.1102	1.0938	1.0959	1.0959	1.0938	1.0800	1.0949	0.1	1.0254	-0.0178	12.6	1.0427	0.4	
Oct 1-15 1983	1.1126	1.0944	1.0944	1.0955	1.0934	1.0818	1.0955	-0.7	1.0254	-0.0178	12.6	1.0429	0.4	
Oct 16-31 1983	1.1132	1.0950	1.0950	1.0961	1.0940	1.0824	1.0961	-1.6	1.0254	-0.0178	12.6	1.0431	-0.3	

Year-6													
	Channel 13 Asymmetric Slopes						Channel 12, 13, and 14 Mean Slope and Offsets						
	Solar Zenith Angle Range						Ch 13		Ch 12			Ch 14	
Half Month	-90 to -60	-60 to -30	-30 to 0	0 to 30	30 to 60	60 to 90	Mean	Ch 13 Offset	LW	SW	Ch 12 Offset	Ch 14 Slope	Ch 14 Offset
Nov 1-15 1983	1.1149	1.0947	1.0936	1.0968	1.0947	1.0830	1.0968	-1.7	1.0254	-0.0178	12.6	1.0433	-1.9
Nov 16-30 1983	1.1155	1.0953	1.0942	1.0974	1.0953	1.0836	1.0974	-2.6	1.0254	-0.0178	12.6	1.0435	-2.3
Dec 1-15 1983	1.1147	1.0968	1.0957	1.0979	1.0957	1.0827	1.0979	-3.2	1.0254	-0.0178	12.6	1.0437	-2.1
Dec 16-31 1983	1.1153	1.0974	1.0963	1.0985	1.0963	1.0833	1.0985	-4.5	1.0254	-0.0178	12.6	1.0439	-2.8
Jan 1-15 1984	1.1158	1.1002	1.0969	1.0991	1.0969	1.0839	1.0991	-4.9	1.0254	-0.0178	12.6	1.0441	-2.8
Jan 16-31 1984	1.1164	1.1008	1.0975	1.0997	1.0975	1.0845	1.0997	-4.5	1.0254	-0.0178	12.6	1.0443	-2.7
Feb 1-15 1984	1.1159	1.1025	1.0992	1.1003	1.0981	1.0840	1.1003	-3.5	1.0254	-0.0178	12.6	1.0446	-2.3
Feb 16-28 1984	1.1165	1.1031	1.0998	1.1009	1.0987	1.0846	1.1009	-2.1	1.0254	-0.0178	12.6	1.0448	-1.8
Mar 1-15 1984	1.1173	1.1038	1.1015	1.1015	1.1000	1.0853	1.1015	-0.8	1.0254	-0.0178	12.6	1.0450	-1.0
Mar 16-31 1984	1.1178	1.1043	1.1020	1.1020	1.1005	1.0858	1.1020	0.6	1.0254	-0.0178	12.6	1.0452	-0.1
Apr 1-15 1984	1.1172	1.1037	1.1048	1.1037	1.1025	1.0852	1.1026	1.8	1.0254	-0.0178	12.6	1.0454	0.2
Apr 16-30 1984	1.1178	1.1043	1.1054	1.1043	1.1031	1.0858	1.1032	2.5	1.0254	-0.0178	12.6	1.0456	0.2
May 1-15 1984	1.1188	1.1037	1.1069	1.1058	1.1047	1.0868	1.1038	3.5	1.0254	-0.0178	12.6	1.0458	0.7
May 16-31 1984	1.1194	1.1043	1.1075	1.1064	1.1053	1.0874	1.1044	3.6	1.0254	-0.0178	12.6	1.0461	0.3
Jun 1-15 1984	1.1197	1.1049	1.1081	1.1069	1.1050	1.0888	1.1049	3.9	1.0254	-0.0178	12.6	1.0463	0.3
Jun 16-30 1984	1.1203	1.1055	1.1087	1.1075	1.1056	1.0894	1.1055	4.4	1.0254	-0.0178	12.6	1.0465	0.4
Jul 1-15 1984	1.1201	1.1061	1.1093	1.1073	1.1060	1.0902	1.1061	4.4	1.0254	-0.0178	12.6	1.0467	0.5
Jul 16-31 1984	1.1208	1.1067	1.1099	1.1079	1.1066	1.0908	1.1067	4.8	1.0254	-0.0178	12.6	1.0469	0.7
Aug 1-15 1984	1.1213	1.1073	1.1105	1.1084	1.1062	1.0924	1.1073	5.2	1.0254	-0.0178	12.6	1.0471	0.8
Aug 16-31 1984	1.1219	1.1079	1.1111	1.1090	1.1068	1.0929	1.1079	4.4	1.0254	-0.0178	12.6	1.0473	0.5
Sep 1-15 1984	1.1239	1.1073	1.1094	1.1094	1.1073	1.0933	1.1084	3.1	1.0254	-0.0178	12.6	1.0475	1.7
Sep 16-30 1984	1.1245	1.1079	1.1100	1.1100	1.1079	1.0939	1.1090	1.6	1.0254	-0.0178	12.6	1.0477	0.9
Oct 1-15 1984	1.1269	1.1085	1.1085	1.1096	1.1075	1.0957	1.1096	-0.6	1.0254	-0.0178	12.6	1.0479	0.0
Oct 16-31 1984	1.1275	1.1091	1.1091	1.1102	1.1081	1.0963	1.1102	-1.9	1.0254	-0.0178	12.6	1.0481	-0.6

Year-7													
	Channel 13 Asymmetric Slopes						Channel 12, 13, and 14 Mean Slope and Offsets						
	Solar Zenith Angle Range						Ch 13		Ch 12			Ch 14	
Half Month	-90 to -60	-60 to -30	-30 to 0	0 to 30	30 to 60	60 to 90	Mean	Ch 13 Offset	LW	SW	Ch 12 Offset	Ch 14 Slope	Ch 14 Offset
Nov 1-15 1984	1.1291	1.1087	1.1076	1.1108	1.1087	1.0968	1.1108	-2.8	1.0254	-0.0178	12.6	1.0483	-0.7
Nov 16-30 1984	1.1297	1.1093	1.1082	1.1114	1.1093	1.0974	1.1114	-3.2	1.0254	-0.0177	12.6	1.0485	-1.0
Dec 1-15 1984	1.1289	1.1108	1.1097	1.1119	1.1097	1.0966	1.1119	-3.9	1.0254	-0.0176	12.6	1.0487	-1.3
Dec 16-31 1984	1.1295	1.1114	1.1103	1.1125	1.1103	1.0971	1.1125	-3.6	1.0254	-0.0175	12.6	1.0489	-0.9
Jan 1-15 1985	1.1300	1.1142	1.1109	1.1131	1.1109	1.0977	1.1131	-2.7	1.0254	-0.0173	12.6	1.0491	-0.1
Jan 16-31 1985	1.1306	1.1148	1.1115	1.1137	1.1115	1.0983	1.1137	-3.0	1.0254	-0.0172	12.6	1.0493	-0.2
Feb 1-15 1985	1.1300	1.1164	1.1131	1.1142	1.1131	1.0977	1.1142	-2.9	1.0254	-0.0171	12.6	1.0495	-0.5
Feb 16-28 1985	1.1306	1.1170	1.1137	1.1148	1.1126	1.0983	1.1148	-2.5	1.0254	-0.0170	12.6	1.0497	-0.3
Mar 1-15 1985	1.1314	1.1177	1.1154	1.1154	1.1138	1.0990	1.1154	-1.5	1.0254	-0.0168	12.6	1.0500	0.3
Mar 16-31 1985	1.1320	1.1183	1.1160	1.1160	1.1144	1.0996	1.1160	-0.4	1.0254	-0.0167	12.6	1.0502	1.1
Apr 1-15 1985	1.1313	1.1177	1.1188	1.1177	1.1165	1.0990	1.1166	1.3	1.0254	-0.0166	12.6	1.0504	1.6
Apr 16-30 1985	1.1319	1.1183	1.1194	1.1183	1.1171	1.0995	1.1172	3.2	1.0254	-0.0165	12.6	1.0506	2.2
May 1-15 1985	1.1330	1.1177	1.1209	1.1198	1.1187	1.1006	1.1178	4.5	1.0254	-0.0163	12.6	1.0508	2.9
May 16-31 1985	1.1335	1.1182	1.1214	1.1203	1.1192	1.1011	1.1183	5.1	1.0254	-0.0162	12.6	1.0510	2.7
Jun 1-15 1985	1.1339	1.1189	1.1221	1.1209	1.1190	1.1026	1.1189	5.3	1.0254	-0.0161	12.6	1.0512	2.7
Jun 16-30 1985	1.1345	1.1195	1.1227	1.1215	1.1196	1.1032	1.1195	4.4	1.0254	-0.0160	12.6	1.0514	2.1
Jul 1-15 1985	1.1343	1.1201	1.1233	1.1213	1.1200	1.1040	1.1201	4.8	1.0254	-0.0158	12.6	1.0516	2.2
Jul 16-31 1985	1.1349	1.1207	1.1240	1.1219	1.1206	1.1046	1.1207	4.3	1.0254	-0.0156	12.6	1.0518	1.9
Aug 1-15 1985	1.1354	1.1213	1.1246	1.1224	1.1202	1.1062	1.1213	4.2	1.0254	-0.0155	12.6	1.0520	2.0
Aug 16-31 1985	1.1360	1.1219	1.1252	1.1230	1.1208	1.1068	1.1219	4.0	1.0254	-0.0154	12.6	1.0522	1.8
Sep 1-15 1985	1.1382	1.1214	1.1235	1.1235	1.1214	1.1072	1.1225	3.5	1.0254	-0.0152	12.6	1.0525	1.9
Sep 16-30 1985	1.1388	1.1220	1.1241	1.1241	1.1220	1.1078	1.1231	2.1	1.0254	-0.0151	12.6	1.0527	1.3
Oct 1-15 1985	1.1411	1.1225	1.1225	1.1236	1.1215	1.1096	1.1236	0.5	1.0254	-0.0150	12.6	1.0529	0.7
Oct 16-31 1985	1.1417	1.1231	1.1231	1.1242	1.1221	1.1101	1.1242	-0.8	1.0254	-0.0149	12.6	1.0531	0.3

Year-8													
	Channel 13 Asymmetric Slopes						Channel 12, 13, and 14 Mean Slope and Offsets						
	Solar Zenith Angle Range						Ch 13		Ch 12			Ch 14	
Half Month	-90 to -60	-60 to -30	-30 to 0	0 to 30	30 to 60	60 to 90	Mean	Ch 13 Offset	LW	SW	Ch 12 Offset	Ch 14 Slope	Ch 14 Offset
Nov 1-15 1985	1.1434	1.1227	1.1215	1.1248	1.1227	1.1106	1.1248	-2.6	1.0254	-0.0148	12.6	1.0533	-0.7
Nov16-30 1985	1.1440	1.1233	1.1221	1.1254	1.1233	1.1112	1.1254	-3.5	1.0254	-0.0146	12.6	1.0535	-1.0
Dec 1-15 1985	1.1432	1.1249	1.1237	1.1260	1.1237	1.1105	1.1260	-4.1	1.0254	-0.0145	12.6	1.0537	-1.1
Dec16-31 1985	1.1438	1.1255	1.1243	1.1266	1.1243	1.1111	1.1266	-3.8	1.0254	-0.0144	12.6	1.0539	-0.8
Jan 1-15 1986	1.1443	1.1283	1.1249	1.1272	1.1249	1.1116	1.1272	-3.0	1.0254	-0.0142	12.6	1.0542	-0.5
Jan16-31 1986	1.1448	1.1288	1.1254	1.1277	1.1254	1.1121	1.1277	-2.7	1.0254	-0.0141	12.6	1.0544	-0.3
Feb 1-15 1986	1.1443	1.1306	1.1272	1.1283	1.1260	1.1116	1.1283	-1.1	1.0254	-0.0140	12.6	1.0546	0.7
Feb16-28 1986	1.1449	1.1312	1.1278	1.1289	1.1266	1.1122	1.1289	-0.4	1.0254	-0.0139	12.6	1.0548	0.9
Mar 1-15 1986	1.1457	1.1319	1.1295	1.1295	1.1279	1.1129	1.1295	0.0	1.0254	-0.0137	12.6	1.0550	1.2
Mar16-31 1986	1.1463	1.1325	1.1301	1.1301	1.1285	1.1135	1.1301	0.6	1.0254	-0.0136	12.6	1.0552	1.2
Apr 1-15 1986	1.1456	1.1318	1.1330	1.1318	1.1306	1.1128	1.1307	0.8	1.0254	-0.0135	12.6	1.0554	1.5
Apr16-30 1986	1.1461	1.1323	1.1335	1.1323	1.1311	1.1133	1.1312	M	1.0254	-0.0134	12.6	1.0556	M
May 1-15 1986	1.1472	1.1317	1.1350	1.1338	1.1327	1.1144	1.1318	M	1.0254	-0.0132	12.6	1.0558	M
May16-31 1986	1.1478	1.1323	1.1356	1.1344	1.1333	1.1150	1.1324	M	1.0254	-0.0131	12.6	1.0560	M
Jun 1-15 1986	1.1482	1.1330	1.1363	1.1350	1.1331	1.1165	1.1330	5.5*	1.0254	-0.0130	12.6	1.0562	2.6*
Jun16-30 1986	1.1488	1.1336	1.1369	1.1356	1.1337	1.1170	1.1336	5.5	1.0254	-0.0129	12.6	1.0564	2.6
Jul 1-15 1986	1.1486	1.1342	1.1375	1.1354	1.1341	1.1179	1.1342	5.4	1.0254	-0.0127	12.6	1.0566	2.5
Jul16-31 1986	1.1491	1.1347	1.1380	1.1359	1.1346	1.1184	1.1347	5.1	1.0254	-0.0126	12.6	1.0568	2.3
Aug 1-15 1986	1.1496	1.1353	1.1386	1.1364	1.1342	1.1200	1.1353	4.8	1.0254	-0.0125	12.6	1.0570	2.2
Aug16-31 1986	1.1502	1.1359	1.1392	1.1370	1.1348	1.1206	1.1359	3.7	1.0254	-0.0124	12.6	1.0573	1.7
Sep 1-15 1986	1.1524	1.1354	1.1375	1.1375	1.1354	1.1210	1.1365	2.4	1.0254	-0.0122	12.6	1.0575	1.4
Sep16-30 1986	1.1530	1.1360	1.1381	1.1381	1.1360	1.1216	1.1371	1.6	1.0254	-0.0121	12.6	1.0577	1.3
Oct 1-15 1986	1.1554	1.1366	1.1366	1.1377	1.1355	1.1235	1.1377	0.4	1.0254	-0.0120	12.6	1.0579	0.9
Oct16-31 1986	1.1560	1.1371	1.1371	1.1382	1.1360	1.1240	1.1382	-0.2	1.0254	-0.0119	12.6	1.0581	0.6

* Assume that offset for Jun 16-30, 1986 is the same as Jun 1-15, 1986 since no observations are available for the period.
M Offset is missing due to lack of WFOV observations during the period.

	Year-9												
	Channel 13 Asymmetric Slopes						Channel 12, 13, and 14 Mean Slope and Offsets						
	Solar Zenith Angle Range						Ch 13		Ch 12			Ch 14	
Half Month	-90 to -60	-60 to -30	-30 to 0	0 to 30	30 to 60	60 to 90	Mean	Ch 13 Offset	LW	SW	Ch 12 Offset	Ch 14 Slope	Ch 14 Offset
Nov 1-15 1986	1.1576	1.1366	1.1355	1.1388	1.1366	1.1245	1.1388	-1.6	1.0254	-0.0118	12.6	1.0583	-0.4
Nov16-30 1986	1.1582	1.1372	1.1361	1.1394	1.1372	1.1250	1.1394	-2.1	1.0254	-0.0117	12.6	1.0585	-0.3
Dec 1-15 1986	1.1574	1.1389	1.1377	1.1400	1.1377	1.1243	1.1400	-3.1	1.0254	-0.0116	12.6	1.0587	-0.7
Dec16-31 1986	1.1581	1.1395	1.1383	1.1406	1.1383	1.1249	1.1406	-3.7	1.0254	-0.0115	12.6	1.0589	-0.8
Jan 1-15 1987	1.1585	1.1423	1.1389	1.1412	1.1389	1.1255	1.1412	-4.2	1.0254	-0.0114	12.6	1.0591	-1.1
Jan16-31 1987	1.1592	1.1429	1.1395	1.1418	1.1395	1.1260	1.1418	-3.4	1.0254	-0.0113	12.6	1.0593	-0.4
Feb 1-15 1987	1.1586	1.1447	1.1413	1.1424	1.1401	1.1255	1.1424	-2.1	1.0254	-0.0112	12.6	1.0595	0.3
Feb16-28 1987	1.1592	1.1453	1.1419	1.1430	1.1407	1.1261	1.1430	-1.1	1.0254	-0.0111	12.6	1.0597	0.7
Mar 1-15 1987	1.1600	1.1460	1.1436	1.1436	1.1420	1.1268	1.1436	0.5	1.0254	-0.0110	12.6	1.0599	1.6
Mar16-31 1987	1.1606	1.1466	1.1442	1.1442	1.1426	1.1274	1.1442	1.5	1.0254	-0.0109	12.6	1.0601	2.0
Apr 1-15 1987	1.1599	1.1459	1.1471	1.1459	1.1447	1.1267	1.1448	2.6	1.0254	-0.0108	12.6	1.0603	2.1
Apr16-30 1987	1.1605	1.1465	1.1477	1.1465	1.1453	1.1273	1.1454	4.0	1.0254	-0.0107	12.6	1.0605	2.5
May 1-15 1987	1.1616	1.1459	1.1492	1.1481	1.1469	1.1284	1.1460	4.3	1.0254	-0.0106	12.6	1.0607	2.2
May16-31 1987	1.1622	1.1465	1.1498	1.1487	1.1475	1.1289	1.1466	5.2	1.0254	-0.0105	12.6	1.0609	2.7
Jun 1-15 1987	1.1625	1.1471	1.1504	1.1492	1.1472	1.1304	1.1471	5.6	1.0254	-0.0105	12.6	1.0612	2.8
Jun16-30 1987	1.1631	1.1477	1.1510	1.1498	1.1478	1.1309	1.1477	6.2	1.0254	-0.0104	12.6	1.0614	2.9
Jul 1-15 1987	1.1629	1.1483	1.1516	1.1496	1.1482	1.1318	1.1483	6.8	1.0254	-0.0104	12.6	1.0616	3.1
Jul16-31 1987	1.1635	1.1489	1.1522	1.1502	1.1488	1.1324	1.1489	6.7	1.0254	-0.0103	12.6	1.0618	3.1
Aug 1-15 1987	1.1640	1.1495	1.1528	1.1506	1.1483	1.1340	1.1495	5.7	1.0254	-0.0102	12.6	1.0620	2.4
Aug16-31 1987	1.1646	1.1501	1.1534	1.1512	1.1489	1.1346	1.1501	5.6	1.0254	-0.0102	12.6	1.0622	2.5
Sep 1-15 1987	1.1668	1.1495	1.1517	1.1517	1.1495	1.1350	1.1507	3.9	1.0254	-0.0101	12.6	1.0624	1.9
Sep16-30 1987	1.1674	1.1501	1.1523	1.1523	1.1501	1.1356	1.1513	1.9	1.0254	-0.0100	12.6	1.0626	1.3
Oct 1-15 1987	1.1699	1.1507	1.1507	1.1519	1.1497	1.1375	1.1519	-0.3	1.0254	-0.0099	12.6	1.0628	0.5
Oct16-31 1987	1.1705	1.1513	1.1513	1.1525	1.1503	1.1381	1.1525	-1.4	1.0254	-0.0098	12.6	1.0630	-0.1
Nov 1-15 1987	1.1721	1.1509	1.1498	1.1531	1.1509	1.1386	1.1531	-2.5	1.0254	-0.0097	12.6	1.0632	-0.8

REPORT DOCUMENTATION PAGE

Form Approved
OMB No. 0704-0188

1. AGENCY USE ONLY (Leave blank)	2. REPORT DATE	3. REPORT TYPE AND DATES COVERED
	March 1994	Reference Publication

4. TITLE AND SUBTITLE
Nimbus-7 Earth Radiation Budget Calibration History--Part II: The Earth Flux Channels

5. FUNDING NUMBERS
665-10-70
NAS5-31331

6. AUTHOR(S)
H. Lee Kyle, Douglas Richard R. Hucek, Philip E. Ardanuy, John R. Hickey, Robert H. Maschhoff, Lanning M. Penn, Brian S. Groveman, and Brenda J. Vallette

7. PERFORMING ORGANIZATION NAME(S) AND ADDRESS (ES)
Goddard Space Flight Center
Greenbelt, Maryland 20771

8. PEFORMING ORGANIZATION REPORT NUMBER
94B00047

9. SPONSORING / MONITORING ADGENCY NAME(S) AND ADDRESS (ES)
National Aeronautics and Space Administration
Washington, DC 20546-0001

10. SPONSORING / MONITORING ADGENCY REPORT NUMBER
NASA RP-1335

11. SUPPLEMENTARY NOTES
Kyle: Goddard Space Flight Center, Greenbelt, MD; Hucek, Ardanuy, Penn and Vallette: Research and Data Systems Corp., Greenbelt, MD; Hickey, The Eppley Laboratory, Inc., Newport, RI; Maschhoff, Gulton Industries, Albuquerque, NM; and Groveman, Computer Sciences Corp., Lanham, MD.

12a. DISTRIBUTION / AVAILABILITY STATMENT
Unclassified - Unlimited
Subject Category 35

12b. DISTRIBUTION CODE

13. ABSTRACT *(Maximum 200 words)*

Nine years (November 1978 to October 1987) of Nimbus-7 Earth radiation budget (ERB) products have shown that the global annual mean emitted longwave, absorbed shortwave, and net radiation were constant to within about ± 0.5 W/m^{-2}. Further, most of the small annual variations in the emitted longwave have been shown to be real. To obtain this measurement accuracy, the wide-field-of-view (WFOV) Earth-viewing channels 12 (0.2 to over 50 μm), 13 (0.2 to 3.8 μm), and 14 (0.7 to 2.8 μm) have been characterized in their satellite environment to account for signal variations not considered in the prelaunch calibration equations. Calibration adjustments have been derived for (1) extraterrestrial radiation incident on the detectors, (2) long-term degradation of the sensors, and (3) thermal perturbations within the ERB instrument. The first item is important in all the channels; the second, mainly in channels 13 and 14; and the third, only in channels 13 and 14. The Sun is used as a stable calibration source to monitor the long-term degradation of the various channels. Channel 12, which is reasonably stable to both thermal perturbations and sensor degradation, is used as a reference and calibration transfer agent for the drifting sensitivities of the filtered channels 13 and 14. Redundant calibration procedures were utilized. Laboratory studies complemented analyses of the satellite data. Two nearly independent models were derived to account for the thermal perturbations in channels 13 and 14. The global annual mean terrestrial shortwave and longwave signals proved stable enough to act as secondary calibration sources. Instantaneous measurements may still, at times, be in error by as much as a few Wm^{-2}, but the long-term averages are stable to within a fraction of a Wm^{-2}.

14. SUBJECT TERMS
Earth radiation budget measurements; sensor characterization; calibration procedures on a satellite

15. NUMBER OF PAGES
120

16. PRICE CODE

17. SECURITY CLASSIFICATION OF REPORT	18. SECURITY CLASSIFICATION OF THIS PAGE	19. SECURITY CLASSIFICATION OF ABSTRACT	20. LIMITATION OF ABSTRACT
Unclassified	Unclassified	Unclassified	UL